

**LISA optical bench development**  
**Experimental investigation of tilt-to-length**  
**coupling for a spaceborne gravitational**  
**wave detector**

Von der QUEST-Leibniz-Forschungsschule der  
Gottfried Wilhelm Leibniz Universität Hannover  
zur Erlangung des Grades

DOKTOR DER NATURWISSENSCHAFTEN  
– Dr. rer. nat. –

genehmigte Dissertation  
von

Dipl.-Phys. Maike Danielle Lieser  
geboren am 28.08.1985 in Seeheim-Jugenheim

2017

<b>Referent</b>	Prof. Dr. Karsten Danzmann (AEI Hannover)
<b>Korreferent</b>	Apl. Prof. Dr. Michèle Heurs (AEI Hannover)
<b>Korreferent</b>	Dr. Henry Ward (University of Glasgow)
<b>Tag der Disputation</b>	25. Januar 2017

# Abstract

The Laser Interferometer Space Antenna (LISA) is a future gravitational wave detector in space to measure low-frequency gravitational waves. One of the largest entries in the LISA noise budget is tilt-to-length coupling and it had not previously been investigated experimentally in a representative setup.

To measure tilt-to-length coupling, a setup is needed that simulates inter-spacecraft interferometry. A testbed was built with two Zerodur baseplates. One represents the optical bench for a LISA spacecraft and the other one, the telescope simulator, generates a beam simulating the beam received from a remote spacecraft and provides a reference interferometer.

Within this thesis, most of the telescope simulator was built using hydroxide catalysis bonding, a technique that is proven to be ultra-stable in spaceborne interferometers. The laser preparation and test equipment was installed and the combined setup of optical bench and telescope simulator was commissioned.

A frequency stability of  $300 \text{ Hz}/\sqrt{\text{Hz}}$  and a temperature stability of better than  $10^{-4} \text{ K}/\sqrt{\text{Hz}}$  was demonstrated for the testbed, which is required for future high precision measurements in vacuum with  $\text{pm}/\sqrt{\text{Hz}}$  accuracy.

In LISA, imaging systems in the interferometers are planned to reduce tilt-to-length coupling. Two different designs of imaging systems were investigated in the testbed, one using two lenses and one using four lenses. Using a flat-top beam, similar to what will be received from a distant spacecraft, both imaging systems suppressed tilt-to-length coupling below  $\pm 25 \text{ }\mu\text{m}/\text{rad}$  for a tilt range of  $\pm 300 \text{ }\mu\text{rad}$ , meeting the design requirements.

The performance was also investigated with two Gaussian beams, representative of the local interferometer for the test mass readout. The two-lens imaging system showed a dependency on the beam parameters. With modified beam parameters the requirement was met.

Additionally, the performance of both imaging systems was tested as a function of the misalignment of individual components. The measurements agree well with optical simulations which allows the specifications of imaging systems to be determined by simulations.

**Keywords:** LISA, gravitational wave detector in space, tilt-to-length coupling, imaging systems



# Kurzzusammenfassung

LISA (Laser Interferometer Space Antenna) ist ein zukünftiger Gravitationswellendetektor im Weltraum um Gravitationswellen bei niedrigen Frequenzen zu messen. Eine der größten Beiträge im Rauschbudget für LISA ist die Kopplung von Strahlverkipfung in das Weglängensignal und das wurde bisher noch nicht in einem repräsentativen Aufbau untersucht.

Um diese Kopplung zu messen wird ein Aufbau benötigt, der interferometrische Messungen zwischen Satelliten simuliert. Dafür wurde ein Testaufbau mit zwei Grundplatten aus Zerodur gebaut. Eine repräsentiert die optische Bank eines LISA Satelliten und die andere, der Teleskopsimulator, simuliert den Strahl eines entfernten Satelliten und stellt ein Referenzinterferometer bereit.

Im Rahmen dieser Arbeit wurde der Großteil des Teleskopsimulators mittels ‘hydroxide catalysis bonding’ gebaut, einer Technik, die sich zum Bau von ultrastabilen Interferometern zur Weltraumanwendung bewährt hat. Die Laservorbereitung und die Testinfrastruktur wurden aufgebaut und optische Bank und Teleskopsimulator wurden in Betrieb genommen.

Eine Frequenzstabilität von  $300 \text{ Hz}/\sqrt{\text{Hz}}$  und eine Temperaturstabilität von weniger als  $10^{-4} \text{ K}/\sqrt{\text{Hz}}$  wurden demonstriert, wie sie für zukünftige Präzisionsmessungen im Bereich von  $\text{pm}/\sqrt{\text{Hz}}$  im Vakuum benötigt wird.

Für LISA sind Abbildungssysteme in den Interferometern geplant um die Kopplung von Strahlverkipfung in das Weglängensignal zu reduzieren. Zwei verschiedene Designs von Abbildungssystemen wurden mit dem Aufbau untersucht, eins mit zwei Linsen und eins mit vier Linsen. Bei Verwendung eines ‘flat-top’-Strahls, der den Strahl eines entfernten Satelliten simuliert, reduzierten beide Abbildungssysteme die Kopplung unter  $\pm 25 \mu\text{m}/\text{rad}$  im Winkelbereich von  $\pm 300 \mu\text{rad}$ .

Das Verhalten wurde auch mit zwei Gausstrahlen untersucht, repräsentativ für das lokale Interferometer zur Testmassenauslesung. Das Zwei-Linsen-Abbildungssystem zeigte eine Abhängigkeit von den Strahlparametern. Mit modifizierten Parametern konnte die Anforderung erfüllt werden.

Zusätzlich wurde das Verhalten beider Abbildungssysteme abhängig von der Verschiebung einzelner Komponenten untersucht. Die Messungen stimmen gut mit optischen Simulationen überein, so dass die Simulationen zur Spezifikation von Abbildungssystemen verwendet werden können.

**Stichworte:** LISA, Gravitationswellendetektor im Weltraum, Kopplung von Strahlverkipfung in Weglängensignal, Abbildungssysteme

# Contents

<b>Abstract</b>	<b>3</b>
<b>Kurzzusammenfassung</b>	<b>5</b>
<b>Contents</b>	<b>7</b>
<b>List of Figures</b>	<b>15</b>
<b>List of Tables</b>	<b>19</b>
<b>1 Introduction</b>	<b>21</b>
<b>I Design and Construction of an interferometric testbed for LISA</b>	<b>25</b>
<b>2 LISA interferometry</b>	<b>27</b>
2.1 Introduction of the LISA interferometric concept . . . . .	27
2.2 Interferometer signals . . . . .	31
2.3 Photoreceiver noise . . . . .	34
2.4 Tilt-to-length coupling . . . . .	38
2.5 Suppression by imaging optics . . . . .	41
<b>3 Design of the LISA optical bench testbed</b>	<b>43</b>
3.1 Concept of the test bed . . . . .	43
3.2 Detailed design of the optical bench . . . . .	44
3.3 Detailed design of the telescope simulator . . . . .	50
<b>4 Construction of the telescope simulator</b>	<b>57</b>
4.1 Hydroxide catalysis bonding . . . . .	57
4.2 Optical components . . . . .	59
4.3 Alignment plan for the Telescope Simulator . . . . .	60
4.4 Template bonding of non-critical components . . . . .	62
4.5 Critical alignment steps . . . . .	69
4.6 Integration of metal parts and mounts . . . . .	70

<b>5</b>	<b>Electronics, laser preparation and vacuum tank</b>	<b>75</b>
5.1	Modulation bench . . . . .	75
5.2	Signal readout . . . . .	77
5.3	Control software . . . . .	78
5.4	Vacuum tank . . . . .	80
5.5	Representivity of the operation parameters . . . . .	80
 <b>II Experimental investigation of tilt-to-pathlength coupling in LISA</b>		<b>83</b>
<b>6</b>	<b>Alignment and calibration</b>	<b>85</b>
6.1	Photodiode signal calibration . . . . .	86
6.2	Telescope simulator alignment on optical bench . . . . .	88
6.3	Tilt actuation of the RX beam . . . . .	89
6.4	Pinhole alignment . . . . .	90
6.5	Reference pinhole on the Telescope Simulator . . . . .	91
6.6	Alignment test using the flipping procedure . . . . .	94
6.7	Investigation of the pinhole-pinhole measurement with the flat-top beam . . . . .	97
6.8	Temperature dependencies tip-tilt mount . . . . .	104
6.9	Telescope simulator height variation removal . . . . .	108
6.10	TTL coupling without imaging systems . . . . .	108
6.11	Summary and conclusion of the commissioning . . . . .	109
<b>7</b>	<b>Investigation of the two-lens imaging system design</b>	<b>111</b>
7.1	Design and alignment . . . . .	112
7.2	Nominal performance . . . . .	112
7.3	Sensitivity to misalignments . . . . .	114
7.4	Compensation by photodiode alignment . . . . .	119
7.5	Investigations with the Gaussian RX beam . . . . .	121
<b>8</b>	<b>Investigation of the four-lens imaging system design</b>	<b>127</b>
8.1	Design and alignment . . . . .	127
8.2	Nominal performance . . . . .	131
8.3	Sensitivity to misalignments . . . . .	132
8.4	Compensation by photodiode alignment . . . . .	136
8.5	The effect of the field-stop . . . . .	136
8.6	Influence of the RX aperture . . . . .	138
<b>9</b>	<b>Summary and discussion</b>	<b>141</b>



<b>III Preparations for performance measurements in vacuum with this setup</b>	<b>143</b>
<b>10 Towards picometer interferometry</b>	<b>145</b>
10.1 Temperature stability . . . . .	146
10.2 Laser frequency stability . . . . .	148
10.3 Outlook . . . . .	151
<b>11 Summary</b>	<b>153</b>
<b>A Read out noise floor</b>	<b>155</b>
A.1 science interferometer . . . . .	159
A.2 reference interferometer . . . . .	160
<b>B As-built component list</b>	<b>163</b>
<b>Bibliography</b>	<b>169</b>



# Acronyms

**A phase** phase of the heterodyne signal between the RX and TX beam.

**AEI** Albert Einstein Institute (Hannover).

**AM** amplitude modulation.

**AOM** acousto-optical modulator.

**ASD** Airbus Defense and Space.

**aux SEPD** auxiliary single element photo diode on the TS with a big active area (8 mm).

**B phase** phase of the heterodyne signal between the LO and TX beam.

**BS** beam splitter.

**C phase** phase of the heterodyne signal between the RX and LO beam.

**CQP** calibrated quadrant photo diode pair.

**DPS** differential power sensing.

**DWS** differential wavefront sensing.

**EBB** elegant breadboard.

**eLISA** evolved laser interferometer space antenna.

**ESA** European Space Agency.

**FEE** front end electronics.

**FIOS** fiber injector optical subassembly.

**GRS** gravitational reference sensor.

**HWP** half wave plate.

**IfoCAD** optical simulation software developed at AEI.

**LISA Pathfinder** technology demonstrator mission.

**LO** local oscillator beam, stable reference beam.

**LPF** LISA Pathfinder.

**MACOR** machinable glass ceramic (by Corning Inc.).

**MOSA** movable optical sub-assembly.

**NGO** New Gravitational wave Observatory, mission concept with two arms.

**NPRO** non-planar ring oscillator.

**OB** optical bench.

**OBI** optical bench interferometer (LISA Pathfinder).

**OPD** optical pathlength difference stabilization.

**PBS** polarization beam splitter.

**POM** polyoxymethylene (by DuPont).

**QPD** quadrant photo diode.

**reference pinhole SEPD** reference single element photo diode on the TS with a 150  $\mu\text{m}$  pinhole aperture.

**ref QPD** reference quadrant photo diode on the TS.

**ref SEPD** reference single element photo diode on the TS with a 150  $\mu\text{m}$  pinhole aperture.

**RX** Beam received from the distant spacecraft and injected into the OB from the telescope. On the telescope simulator a 1 mm Gaussian RX beam (RX Gauss) or a RX beam with a flat intensity and phase profile (RX flat-top) can be used.

**RX clip** aperture in the interface of OB and TS.

**SCI** science interferometer.

**sciQPD1** science interferometer QPD 1 (see fig. 3.2).

**sciQPD2** science interferometer QPD 2 (see fig. 3.2).

**SEPD** single element photo diode.

**temporary pinhole SEPD** temporary single element photo diode in the RX aperture with a 150  $\mu\text{m}$  pinhole aperture.

**TS** telescope simulator.

**TTL** tilt-to-length coupling.

**TX** transmitted beam; beam from the local laser on the OB launched to the telescope and transmitted to the distant spacecraft.

**UGL** University of Glasgow.

**WinCAM** beam profiler camera from DataRay Inc., WinCamD series.



# List of Figures

1.1	The orbit around the Sun for the eLISA mission . . . . .	22
1.2	The LISA Pathfinder spacecraft and payload . . . . .	23
1.3	One of the three LISA spacecraft. Image credit: Milde Marketing .	23
2.1	Schematic of one laser link between two LISA spacecraft . . . . .	28
2.2	The design of the telescope, optical bench and test mass structure (MOSA) for NGO . . . . .	29
2.3	Optical layout of the elegant breadboard (EBB) of the optical bench for the original LISA mission design . . . . .	30
2.4	Schematic and photograph of the active area of a quadrant photodiode . . . . .	32
2.5	Circuit layout of a transimpedance amplifier (TIA). . . . .	35
2.6	Measured voltage noise and estimated input current noise . . . . .	37
2.7	Sketch to illustrate the geometric tilt-to-length coupling . . . . .	39
2.8	Sketch for illustrating TTL coupling due to mismatched beam parameters . . . . .	40
2.9	Tilted wave fronts on a photodiode with gap . . . . .	41
2.10	Removing beam walk on the photodiode with an imaging system .	42
3.1	Schematic of the testbed with optical bench and telescope simulator	45
3.2	Layout of the OB with the key components labeled . . . . .	47
3.3	Photographs of the two different imaging system mechanics . . . . .	49
3.4	Mount of the RX clip . . . . .	50
3.5	Layout of the telescope simulator with the key components labeled	51
3.6	One of the adjustable feet for the tip-tilt mount to align the telescope simulator baseplate . . . . .	53
3.7	Photograph of the apodized aperture for the flat-top generator . .	54
3.8	Photograph of the flat-top generator . . . . .	55
4.1	Template bonding and CMM assisted alignment . . . . .	59
4.2	Construction steps for the telescope simulator . . . . .	61
4.3	TS baseplate in the aluminum frame for easier handling . . . . .	63
4.4	The beam orientation of the RX Gauss beam after bonding the FIOS measured with the CMM . . . . .	64

4.5	Measured position accuracy of the TS baseplate on the CMM table	65
4.6	Curing of the bond of the RX Gauss FIOS over several days . . . . .	66
4.7	CAD models of the two templates for bonding the non-critical components of the telescope simulator . . . . .	67
4.8	Photographs of template bonding . . . . .	68
4.9	Assembly and gluing of the $\lambda/2$ -waveplate . . . . .	69
4.10	Actuator assembly . . . . .	72
4.11	Photograph of completed telescope simulator . . . . .	72
4.12	Photograph of completed optical bench and telescope simulator . . . . .	73
5.1	Schematic of the laser preparation and electronic setup. . . . .	76
5.2	Modulation bench overview. . . . .	76
5.3	Schematic overview of the electronics for the modulation bench. . . . .	78
5.4	Screen shot of the user interface of the measurement program. . . . .	79
5.5	Picture of OB and TS in the vacuum tank with open lid. . . . .	80
6.1	Calibration of raw DWS signals for Gaussian RX beam . . . . .	86
6.2	DPS and DWS calibration for the RX flat-top beam with an additional QPD . . . . .	87
6.3	Beam angle vs. DWS signal for the RX flat-top beam . . . . .	88
6.4	Picture of a four-hole and a pinhole aperture . . . . .	90
6.5	Pathlength signal of the temporary pinhole, not aligned, with RX Gauss . . . . .	92
6.6	Pathlength signal of the temporary pinhole, aligned, with RX Gauss . . . . .	93
6.7	Pathlength signal of the temporary pinhole, not aligned, with RX flat-top . . . . .	93
6.8	Pathlength signal of the temporary pinhole, aligned, with RX flat-top . . . . .	94
6.9	Pathlength signal of the temporary pinhole, after flip, with RX Gauss . . . . .	95
6.10	Pathlength signal of the temporary pinhole, after flip, with RX Gaussian, realigned. . . . .	96
6.11	Pathlength signal of the temporary pinhole before and after flipping. . . . .	96
6.12	Setup on the optical bench to measure and suppress the light back reflected from the pinhole aperture surface . . . . .	98
6.13	Pinhole-pinhole measurement to investigate stray light from the aperture . . . . .	98
6.14	Amplitude of the heterodyne signal of the C phase behind the open port of BS23 . . . . .	99
6.15	Illustration of a ghost beam from the back side of a beam splitter. . . . .	100
6.16	Pinhole-pinhole measurement to investigate ghost beams . . . . .	101
6.17	Longterm measurement with adjustment screws attached to the mounting feet . . . . .	105
6.18	Longterm measurement with adjustment screws retracted from the mounting feet. . . . .	105



6.19	Clamping spring of the mounting feet in the position with the maximal possible clamping force. . . . .	106
6.20	Pathlength vs. temperature, with adjustment screws. . . . .	107
6.21	Pathlength vs. temperature, without adjustment screws. . . . .	107
6.22	A phase and A+B phase comparison. . . . .	108
6.23	TTL coupling measurement with the RX Gauss beam and no imaging systems in the science interferometer . . . . .	109
7.1	Optical design and a photograph of the two-lens imaging system .	113
7.2	Two-lens imaging systems: nominal performance with the RX flat-top beam . . . . .	114
7.3	Two-lens imaging system: sensitivity to lateral QPD displacement	115
7.4	Two-lens imaging system: sensitivity to lateral displacement of the entire imaging system in x direction. . . . .	116
7.5	Two-lens imaging system: sensitivity to longitudinal displacement of the QPD . . . . .	117
7.6	Two-lens imaging system: sensitivity to lateral displacement of lens 1	118
7.7	Two-lens imaging system: sensitivity to lateral displacement of lens 2	119
7.8	Linear TTL coupling because of a lateral misalignment of Lens2 and compensation by photo diode alignment . . . . .	120
7.9	Result after optimizing the photo diode position . . . . .	120
7.10	Two-lens imaging system: nominal performance with Gaussian RX beam . . . . .	121
7.11	Simulation of additional TTL coupling of unfavorable beam parameter combinations. . . . .	122
7.12	Two-lens imaging system: nominal performance with Gaussian RX beam and 500 mm focal length lens. . . . .	124
7.13	Two-lens imaging system: nominal performance with Gaussian RX beam and 1 m focal length lens. . . . .	124
8.1	Optical design and a photograph of the four-lens imaging system .	129
8.2	The setup for aligning the four-lens imaging system at Airbus DS .	130
8.3	The wavefront measured with the SHS after aligning all four lenses	130
8.4	Four-lens imaging systems: nominal performance with RX flat-top beam . . . . .	132
8.5	Four-lens imaging system: sensitivity to lateral QPD displacement	133
8.6	Four-lens imaging system: sensitivity to a lateral displacement of lens 1 . . . . .	134
8.7	Four-lens imaging system: sensitivity to lateral displacement of lens 2 . . . . .	134
8.8	Four-lens imaging system: sensitivity to lateral displacement of lens 3 . . . . .	135
8.9	Four-lens imaging system: sensitivity to lateral displacement of lens 4 . . . . .	136

8.10	Linear TTL coupling with a lateral misalignment of lens 1 and after realigning the photo diode . . . . .	137
8.11	Comparison of a scenario with field stop and a scenario without. . .	138
8.12	Comparison of a scenario with RX clip and a scenario without RX clip . . . . .	139
9.1	Sensitivity of the different misalignment parameters for both imaging systems, compared to simulated data. . . . .	142
10.1	Schematic of the thermal insulation installed inside the vacuum chamber . . . . .	146
10.2	Multi-layer insulation (MLI) foil and stand-off . . . . .	147
10.3	Spectra of the temperature readout . . . . .	148
10.4	Setup to measure the frequency stability of the iodine stabilized laser system . . . . .	149
10.5	Measured spectrum of the two laser systems compared to initial performance . . . . .	150
10.6	Measured frequency spectrum of the two laser systems after realigning the iodine stabilization of the system 1723A . . . . .	151
B.1	Layout of the telescope simulator with all components labeled . . .	165
B.2	Layout of the optical bench with all components labeled . . . . .	166

# List of Tables

5.1	AOM and heterodyne frequencies . . . . .	77
A.1	Parameters used for the calculations . . . . .	156
A.2	Transmission through a round aperture . . . . .	157
A.3	Power budget . . . . .	158
A.4	parameters for one science interferometer QPD . . . . .	159
A.5	pathlength noise for the signal TX+RX on one segments of one science interferometer QPD . . . . .	159
A.6	parameters for one reference interferometer QPD . . . . .	160
A.7	pathlength noise for the signal TX+RX on one segment of the reference interferometer QPD . . . . .	160
A.8	parameters for the reference pinhole photodiode . . . . .	161
A.9	pathlength noise for the signal TX+RX on the reference pinhole photodiode . . . . .	161
B.1	Component list with nominal and measured positions. . . . .	164
B.2	List of component names and specifications for the telescope simulator. . . . .	167
B.3	List of component names and specifications for the optical bench. . . . .	168



# Introduction

On September 14th 2015, a gravitational wave was detected for the first time [1]. This first detection opened a new window to our universe and started the era of gravitational wave astronomy.

Gravitational waves are ripples in the fabric of space-time, caused by accelerated masses in the universe. They were predicted by Albert Einstein's general theory of relativity [2], but Einstein – at this time – could not imagine an instrument sensitive enough to ever detect this phenomenon. Because of the great stiffness of space-time, even incredibly massive objects as black holes cause only very tiny variations in the space-time. The instruments capable of measuring such small variations in distance are large laser interferometers. GW150914 was detected in the two LIGO (Laser Interferometer Gravitational Wave Observatory) instruments in Hanford and Livingston in the US. Besides LIGO, a network of ground-based detectors is currently under construction to measure more gravitational waves.

**LISA and LISA Pathfinder** The ground-based detectors are sensitive in the range from Hz to kHz, but below about 1 Hz gravitational wave signals are not accessible on Earth, because of the seismic ground motion. To extend the observed frequency regime to lower frequencies, a laser interferometer in space is planned. The European Space Agency (ESA) is planning to launch a spaceborne gravitational wave observatory within their Cosmic Vision program in the 2030s. 'The Gravitational Universe' [3] was selected as the science theme and the call for missions was released in October 2016. The only existing mature mission concept is LISA, the Laser Interferometer Space Antenna, and it is expected to be chosen as the mission concept [4].

Key technologies for LISA were already successfully tested on the LISA Pathfinder mission [5], that was launched in December 2015 and is still operating. In Pathfinder, the drag-free test mass control and the local interferometry

was tested inside one spacecraft with two test masses separated by 38 cm. The requirements and expectations for the performance were exceeded in early operations. Further experiments and studies are underway to provide complete understanding of the measurement noise models.

LISA is a laser interferometer with millions of kilometers armlength to be sensitive to gravitational waves in the millihertz regime. It is a triangular constellation with three satellites trailing the Earth on its orbit around the Sun (see fig. 1.1). The satellites host free-falling test masses and the distances between these test masses are tracked by interferometric measurements between spacecraft. Information about the astrophysical sources and the science case for LISA can be found for example in a study for eLISA [6], the White Paper [3] and a recent study on multi-band gravitational-wave astronomy [7].

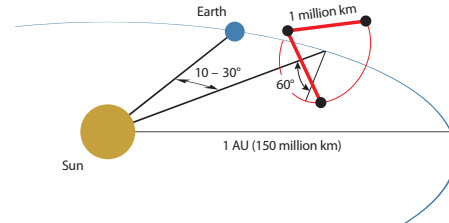


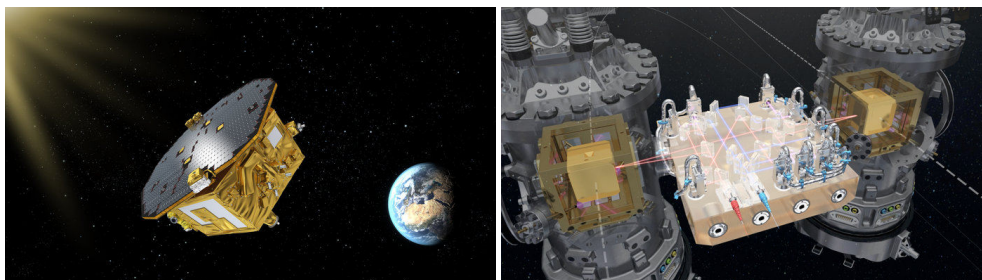
**Figure 1.1:** The orbit around the Sun for the eLISA mission design with two arms. Credit: The Gravitational Universe [3]

**Optical bench development** In 2009, ESA started a technology development project to build and characterize a functional prototype, an elegant breadboard (EBB), of a LISA optical bench. The project team included Astrium, the University of Glasgow, TNO and the AEI Hannover. The testing was planned in Hannover and required extensive preparation. Two important conditions to reach the required accuracy of  $\text{pm}/\sqrt{\text{Hz}}$  in the interferometric readout are a temperature-stable environment and a good frequency stability of the laser source. The required temperature stability is better than  $10^{-4} \text{ K}/\sqrt{\text{Hz}}$ .

Laser frequency noise couples into the interferometer readout when the armlengths are not matched. On the EBB, armlengths differences in the order of 1 m, required a frequency stability of  $300 / \text{Hz}\sqrt{\text{Hz}}$  for the laser. The first goal of this thesis was to prepare and commission the test equipment to provide this required environment.

During the course of this thesis NASA had to withdraw their contribution to LISA and ESA asked for a reformulation of the mission concept as an European only mission. This meant that the layout of the optical bench would change significantly and it was decided to rescope the running EBB project.

The components intended for the elegant breadboard were used to build the setup presented in this thesis: A minimal optical bench and a telescope simulator to test imaging systems for tilt-to-length coupling suppression. Tilt-to-length coupling is a significant noise source in LISA, that was not investigated experimentally before in a representative way. For the NGO design,



(a) LISA Pathfinder spacecraft

(b) Payload of LISA Pathfinder.

**Figure 1.2:** The LISA Pathfinder spacecraft is on an orbit around the Lagrange point L1, 1.5 million kilometers away from earth. On board are two free falling test masses with an optical bench in between to read out their distance. Image credit: ESA

tilt-to-length coupling was identified as the second largest noise source after shot noise, which illustrates the importance of a good understanding of the coupling and the performance of imaging systems.

The setup was built in a joint effort by most of the previous team: the University of Glasgow, Airbus DS and the AEI in Hannover. Within this thesis, the majority of the telescope simulator was built. The construction of the minimal optical bench and some critical alignment steps were conducted by the University of Glasgow. The goal was to build a setup suitable to measure tilt-to-length coupling and versatile to enable future investigations of different components and measurements with  $\text{pm}/\sqrt{\text{Hz}}$  accuracy. The setup uses Zerodur<sup>®</sup> interferometer baseplates for a low thermal expansion coefficient and all optical components are assembled using hydroxide catalysis bonding, a technique established to build high precision interferometers for space applications.

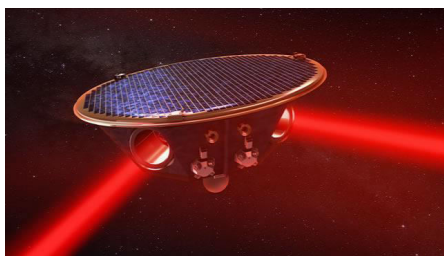


**Figure 1.3:** One of the three LISA spacecraft. Image credit: Milde Marketing

coupling. The performance is tested against the LISA requirement in the range of  $\pm 300 \mu\text{rad}$ , using a beam with a flat phase and intensity profile, representative for a beam received from a distant spacecraft. A systematic alignment sensitivity analysis, performed by misaligning individual components, inves-

The commissioning of the setup included the laser preparation and electronics, the alignment of the telescope simulator with a few  $\mu\text{m}$  precision, which is mounted on the optical bench by gravity, and the calibration of the measured beam angles.

Within this thesis two different designs of imaging systems are investigated that suppress tilt-to-length

investigates how misalignments couple into the performance and validate results from optical simulations.

**Outline of the thesis** This thesis is divided into three parts: The design and construction of an interferometric testbed for LISA with the focus on the construction of the telescope simulator, the experimental investigation of tilt-to-length coupling in LISA with two different imaging systems, and preparations necessary for high precision measurements in vacuum with the existing setup. The main body of the work is described in parts one and two.

After this introduction, in chapter 2, the interferometric scheme of LISA is introduced. Interferometer signals important for this thesis are described and the mechanisms of how tilt couples into the length measurement are discussed as a basis for the imaging system investigations.

In chapter 3 the concept and overall design of the testbed is described and in chapter 4 the construction of the telescope simulator is reported in more detail. To operate the setup, a laser preparation, test equipment and a readout scheme are needed, that are presented in chapter 5.

In chapter 6 the alignment, calibration and commissioning of the combined optical bench and telescope simulator setup is reported. After showing the successful commissioning, the nominal performance and alignment sensitivity analysis for the two different imaging system designs, using a flat-top beam, are shown in chapter 7 and 8. The performance with two Gaussian beams and the influence of beam parameters is investigated in chapter 9.

The results of the imaging system tests are summarized in chapter 10. The two different designs are compared and the implications of the results are discussed.

In chapter 11 an outlook is given into future investigations with this setup, testing the stability of the all-Zerodur design in vacuum.



## Part I

# Design and Construction of an interferometric testbed for LISA



# LISA interferometry

In this chapter an overview of the interferometric concept of a LISA-like mission is given to motivate the design of the setup for the experimental investigations in this thesis. The detailed design of the mission which should fly for the L3 science theme ‘The Gravitational Universe’ is not yet fixed, but it will be a laser interferometer with millions of kilometers armlength [4]. A brief overview of the mission history is given at the beginning of the first section.

After the general mission design, typical interferometer and alignment signals are introduced which are important for this thesis. The concept of heterodyne interferometry is introduced and the differential power sensing (DPS) and differential wavefront sensing (DWS) signals are described as well as the phase definitions for a quadrant photodiode. Different phase definitions are possible and within this thesis the average phase signal was used. The read-out noise as a function of laser power and photo receiver electronic noise is calculated.

In the third part of this chapter the tilt-to-length coupling is discussed. It is one of the largest noise sources for a gravitational wave detector in space and the optical bench development project was dedicated to investigate this effect experimentally. At the end of the chapter, the mechanisms of tilt-to-length coupling are introduced and the concept of interferometric imaging to suppress this coupling.

## 2.1 Introduction of the LISA interferometric concept

In a LISA-like, space-borne gravitational wave observatory, the distance changes between free falling test masses are measured to detect gravitational waves. The triangular constellation will have two or three arms with test masses at

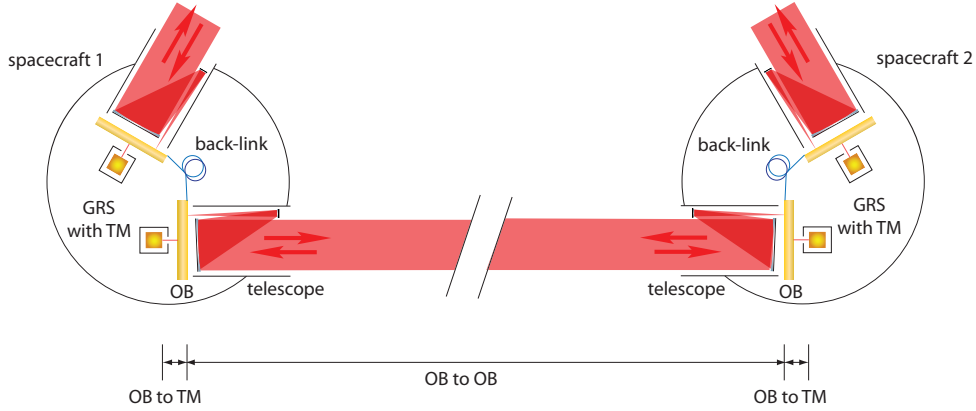


**Figure 2.1:** Schematic of one laser link between spacecraft. The distance measurement between the two test masses (TM) is divided into three parts: One TM to the local OB, distance between the two OBs in distant spacecraft and OB to TM in the other spacecraft. The back-link is providing a phase reference between the different arms.

each end and laser-links in between. The mission architecture is constantly evolving since the first proposal for a gravitational wave observatory in space in 1985 [4]. LISA stands for a class of missions and here a brief overview of the recent mission history is given to clarify the nomenclature of different mission designs and to put the LISA optical bench development project into the context.

In the last decade, first a joint mission of the European Space Agency (ESA) and the National Aeronautics and Space Administration (NASA) was planned, until 2011 [8]. This design had three arms with 5 million kilometers length and is often referred to as the ‘original LISA’ design. In 2011, the mission was reformulated in a study by ESA as an only European mission under the name of New Gravitational Observatory (NGO) [9], later called evolved LISA (eLISA). This design has only two arms and a shorter armlength. With the selection of ‘The Gravitational Universe’ as the science theme for a large mission to be launched in 2034, the mission design will be evolving again. The call for missions was released recently (in October 2016). The mission proposal for this call is expected to have three arms with probably approximately 2.5 million kilometer armlength and will be called ‘LISA’ again.

All mission designs follow the same principle, which is introduced in the following. The laser links in between the test masses are divided in several individual interferometric measurements, which are combined to a Michelson-like interferometer in post processing. One laser link between two test masses in distant spacecraft is divided in three parts: the distance between each test mass and the local optical bench and the distance between the two optical benches in the distant spacecraft (see fig. 2.1). The interferometer measuring the distance between spacecraft is called science interferometer, the interfer-

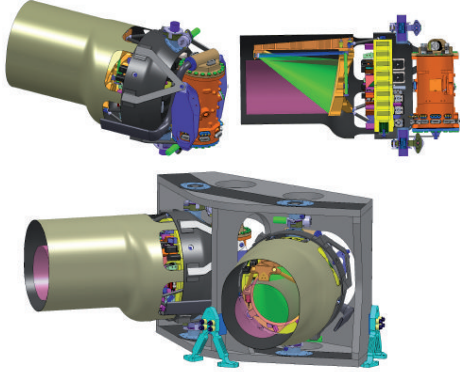


**Figure 2.2:** The design of the telescope, optical bench and test mass structure for NGO. This design is from the NGO Yellow Book ([9]). The assembly of one telescope with the optical bench behind it and the gravitational reference sensor (GRS) – containing the test mass – is called movable optical sub-assembly (MOSA). Two MOSAs in one spacecraft can be moved independent of each other to point the telescopes in the correct direction.

ometer measuring the distance from the optical bench to the test mass is called test mass interferometer. Between two arms of the constellation, a phase reference is needed. To get the gravitational wave signal from these multiple measurements the time delay interferometry (TDI) algorithm is used ([10], [11], [12], [13]). This algorithm can also be used to cancel out laser frequency noise, which has to be suppressed in LISA because of the unequal arms in the interferometer.

In fig. 2.2 the movable optical sub-assembly (MOSA) for the NGO mission design is shown [9]. It will be similar for LISA. The optical bench is placed vertically between the telescope and the test mass inside the gravitational reference sensor (GRS). In this design there is one optical bench and one GRS for each telescope. The two MOSAs can be rotated individually to compensate for breathing of the constellation. For this approach, a flexible back-link solution is needed because the optical benches are moving with the telescopes. An optical fiber was proposed for this purpose and tested experimentally ([14], [15], [16]). The optical path through the fiber only has to be reciprocal – and not absolutely stable – to the picometer level, because it is used in both directions. The requirement for the absolute pathlength stability is more relaxed. An optical fiber is in principle suitable for such a back-link but requires some additional complexity in the optical design because of stray light effects [15]. To test alternatives, like a free-beam back-link, a dedicated experiment was proposed [16] and is under construction [17].

Another solution would be to use only one optical bench, then a back-link is not necessary. This is only possible if there is another mechanism for steering the beam to compensate the breezing of the constellation. A mechanism, called in-field pointing, with an actuated mirror on the optical bench could do that. The feasibility is currently tested in an experiment at Airbus DS [18]. The technical details for this solution are challenging because the actuator has to be in the sensitive measurement path and continuously moving.

In fig. 2.3, the optical layout of the optical bench for the original LISA design [8] is shown. This design was developed for the LISA optical bench

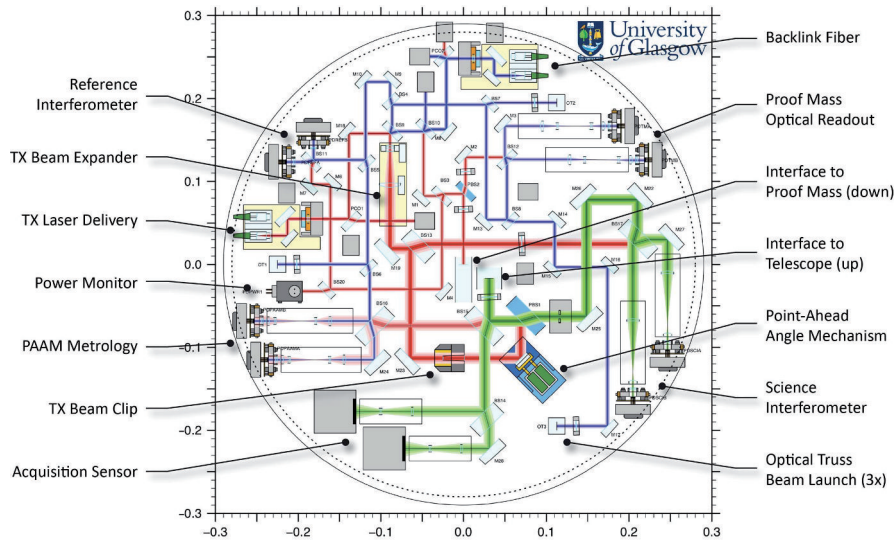


**Figure 2.3:** Optical layout of the elegant breadboard (EBB) of the optical bench for the original LISA mission design. OptoCAD model by UGL, figure reproduced from [22]. Some key features are labeled.

development project [19], the OptoCAD model shown here was produced by UGL. The parts procured for building this elegant breadboard (EBB) within this project were used instead to build the setup presented in this thesis. In the EBB design more interferometers and components were planned to build an optical bench representative for a full LISA optical bench. In addition to the science interferometer for reading out the long arm, it has a test mass interferometer, a reference interferometer and a point ahead angle mechanism (PAAM) interferometer ([20], [21]). The PAAM is a steering mirror that points ahead the outgoing (RX) beam to compensate for the distance the distant spacecraft moves in the light travel time between spacecraft. Shorter armlength would simplify this mechanism [4] and it is not implemented in the NGO design. The optical truss interferometers are additional readouts for deformations of the telescope structure. These interferometers are also not included in the NGO design, because the telescopes are smaller, to allow a smaller optical bench diameter [22]. In the current LISA design no truss interferometers but a PAAM is planned.

Many parameters of the optical design of the mission are not fixed yet, like the armlength, the telescope size and design, the laser power, the size of the optical bench and many others. The 'Gravitational Wave Observatory Designer' is a tool to predict the sensitivity depending on various mission parameters [23].

## 2.2 Interferometer signals

In this section, the principle of heterodyne interferometry, as used for inter-satellite interferometry, is introduced as well as some typical interferometer signals, that are important for this thesis. Throughout the section, references are given for more detailed theoretical descriptions and optical simulations for the interested reader.

### Heterodyne interferometry

In a heterodyne interferometer the reference beam and the measurement beam do not have the same frequency. This results in a beat on the photodiode with a frequency equal to the difference frequency of the two beams. This frequency is called heterodyne frequency  $f_{het}$  and is typically in the order of kHz or MHz. For LISA Pathfinder the heterodyne frequency is approximately 1.6 kHz. For LISA MHz heterodyne frequencies will occur because of the large Doppler shifts due to relative spacecraft velocities. With a heterodyne interferometer it is easily possible to track the phase with high resolution over many fringes. This is why it is used for inter-satellite interferometry where the arm lengths cannot be held constant.

The two laser beams with different frequencies can for example come from two phase locked lasers or from one laser where the frequency is shifted slightly by AOMs. Usually the power of the two interfered beams on the photodiode is written as [24]:

$$P = P_{mean}(1 + c \cos(\omega_{het}t + \phi)) \quad (2.1)$$

Where  $c$  is the contrast,  $\omega_{het}$  the heterodyne frequency and  $\phi$  the phase difference that usually encodes the pathlength change of interest. The contrast is a measure for the AC part of the signal and given by:

$$c = \frac{P_{max} - P_{min}}{P_{max} + P_{min}} \quad (2.2)$$

where  $P_{min}$  and  $P_{max}$  is the minimum and maximum power, respectively.

### Alignment signals

Alignment signals for an interferometer can be calculated using quadrant photodiodes (QPDs). In a QPD the active area of the photodiode is divided in four equally sized parts, called segments, and their signals are processed individually. For technical reasons the segments are separated by a gap that is not sensitive to the light. In fig. 2.4 a schematic is showing how the active area is divided and an example of how the segments are named. There are different conventions how to label the segments. Throughout this thesis the labeling shown here is used.

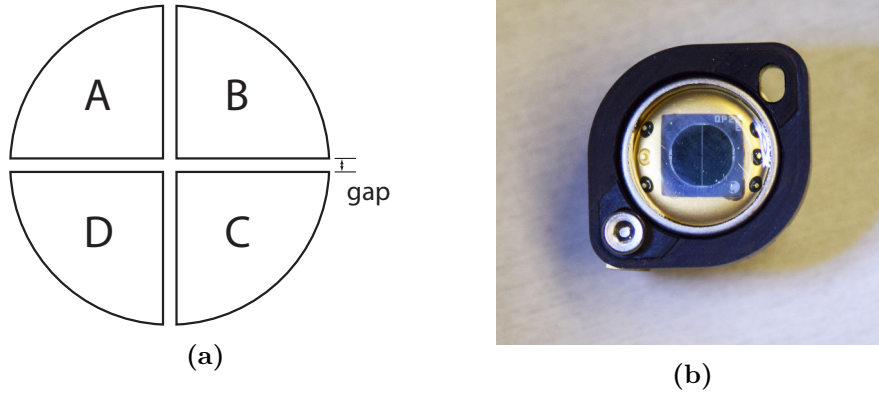


**Figure 2.4:** Schematic of the active area of a quadrant photodiode (a) and a photograph of a diode with housing (b). The labeling of the segments is the convention used in this thesis.

With a QPD four signals are generated which can be combined to get alignment information. The beams incident on the active area are inducing a photo current which is proportional to the beam power on the photodiode surface. How to calculate the interferometer signal is given in [25].

By combining the DC signals from the different segments the position of the beam on the QPD surface can be determined. This signal is usually called differential power sensing signal (DPS) and is given by:

$$\text{DPS}_{vertical} = \frac{P_{top} - P_{bottom}}{P_{sum}} = \frac{(P_A + P_B) - (P_C + P_D)}{P_A + P_B + P_C + P_D} \quad (2.3)$$

$$\text{DPS}_{horizontal} = \frac{P_{left} - P_{right}}{P_{sum}} = \frac{(P_A + P_C) - (P_B + P_D)}{P_A + P_B + P_C + P_D} \quad (2.4)$$

$P_i$  is here the mean power value of the four segments A,B,C and D.  $P_{top}$  and  $P_{bottom}$  are the combined power signals of the top and bottom half of the QPD,  $P_{left}$  and  $P_{right}$  the sum of the left the right side.  $P_{sum}$  is the power signal of all four segments combined. With these two signals the beam position of one beam with regard to the photodiode position can be sensed in the vertical and the horizontal axis. An interference or phase readout is not required. With two beams incident on the photodiode, the (weighted) average of both beam positions is measured.

Another very useful signal is the differential wavefront sensing signal (DWS) where the phase signals of the different segments are compared instead of the power levels.



$$\text{DWS}_{vertical} = \phi_{top} - \phi_{bottom} \quad (2.5)$$

$$\text{DWS}_{horizontal} = \phi_{left} - \phi_{right} \quad (2.6)$$

These signals are a measure for the horizontal and vertical angle between two wave fronts incident on the QPD.  $\phi_{left}$  and  $\phi_{right}$  are the phase signals of the two segments on the left and the two segments on the right of the QPD. For the vertical tilt the phase on the upper and the lower part of the photodiode is compared. The DWS signal is much more sensitive than the DPS signal and, to first order, independent of the photodiode position.

For a fundamental Gaussian beam the DPS and the DWS signal can be calculated analytically. The DPS signal for one beam on a QPD with infinite diameter and no slits is given by an error function:

$$\text{DPS}_{analytical} = -\text{erf}\left(\frac{x_0\sqrt{2}|\cos\alpha|}{w}\right) \quad (2.7)$$

Here  $x_0$  is the shift of the beam on the photodiode,  $\alpha$  is the incident angle of the beam and  $w$  is the radius of the beam on the photodiode. This analytical solution can be found in [25] and [24]. In these references also more general solutions for QPDs with slits and with a finite radius where beam clipping occurs are given.

### Phase definition for a QPD

For a QPD the measured phase on the four segments can be combined in different ways to get the phase for the whole beam. The definition chosen for LISA Pathfinder (LPF) is via the complex amplitude of the photo current [26]. The phase is the argument of the complex amplitude  $C$  which is defined as the integral of the two electric fields over the detector surface. The phase of an QPD is then the argument of the sum of the complex amplitudes of all four segments:

$$\phi_{LPF} = \arg(C_A + C_B + C_C + C_D) \quad (2.8)$$

This definition is the one closest to the phase measured with a SEPD.

Another possible definition is the arithmetic mean of the phases measured on the different segments. This averaged phase (AP) definition is used for the measurements in this thesis:

$$\phi_{AP} = \frac{\phi_A + \phi_B + \phi_C + \phi_D}{4} \quad (2.9)$$

The averaged phase definition has the disadvantage that it weighs the phase on all four segments equally even if the beam is significantly off center. This can be taken into account by weighing the phases according to the signal

amplitudes on the segments. The LPF phase does include the correct weighing because adding the complex amplitudes is basically a vector addition.

A more detailed definition and comparison of the different phase definitions are given in [26].

## 2.3 Photoreceiver noise

The photo current generated by the photodiode is converted to a voltage by a transimpedance amplifier (TIA) shown in fig. 2.5. The voltage is converted to a digital phase signal in the phase meter ([27], [28]). Shot noise, electronic noise and digitization noise contribute to the readout noise.

The shot noise is given by:

$$\tilde{I}_{shot} = \sqrt{2q_e I_{ph}} \quad (2.10)$$

$I_{ph}$  is the photo current dependent on the efficiency  $\eta$  of the photodiode:  $I_{ph} = \eta(P_{meas} + P_{ref})$ .  $P_{meas}$  and  $P_{ref}$  are the light powers of the measurement and the reference beam, respectively.  $q_e$  is the elementary charge. According to [23], [29] and calculations by Gerhard Heinzel, the linear spectral density (of a time domain signal  $s(t)$ ) of the resulting phase noise  $\tilde{\phi}$  can be calculated using the carrier-to-noise density  $C/N_0$  and is given by:

$$\tilde{\phi} = \frac{1}{C/N_0} = \frac{\tilde{s}}{s_{signal,rms}} \quad (2.11)$$

$\tilde{s}$  is the linear spectral density of  $s$  and  $s_{signal,rms}$  is the RMS amplitude of the sinusoidal signal ( $1/\sqrt{2}$  of the peak amplitude). For the shot noise this is:

$$\tilde{\phi} = \frac{\tilde{I}_{shot}}{I_{signal,rms}} = \frac{\sqrt{2q_e I_{ph}}}{A_{het}} \quad (2.12)$$

with the RMS heterodyne signal amplitude:

$$A_{het} = \frac{1}{\sqrt{2}} \eta 2 \sqrt{\gamma P_{meas} P_{ref}} = \eta \sqrt{2\gamma P_{meas} P_{ref}} \quad (2.13)$$

$\gamma$  the heterodyne efficiency which is given by the mode overlap of the two beams and  $\eta$  is the efficiency of the photodiode. This is the amplitude on one segment of a quadrant photodiode or of one single element photodiode. The light powers  $P_{meas}$  and  $P_{ref}$  are here the power levels per segment or single element photodiode.

The frequency dependent output voltage noise of the TIA is the sum of uncorrelated noise contributions. As they are uncorrelated, they sum up quadratically [30]:

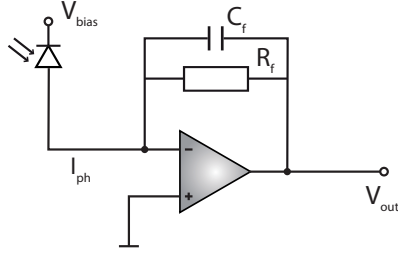


**Figure 2.5:** Circuit layout of a transimpedance amplifier (TIA).

$$\tilde{U}_{out} = \sqrt{R_f \tilde{I}_{shot}^2 + \tilde{U}_{johnson}^2 + \tilde{U}_{amp}^2 + R_f \tilde{I}_i^2} \quad (2.14)$$

$$(2.15)$$

$\tilde{I}_{shot}$  is the shot noise of the photo current,  $\tilde{U}_{johnson}$  is the Johnson noise (thermal noise),  $\tilde{U}_{amp}$  the input voltage noise of the op-amp,  $\tilde{I}_i$  the input current noise of the op-amp and  $R_f$  the resistance of the feedback resistor of the TIA.

The input current noise of the amplifier electronics can be estimated by measuring the noise spectral density of the output voltage with a shot noise limited light source and with no light incident on the photodiode [30].

The following derivation is taken from [31] and [32]. The output voltage noise with a shot noise limited light source incident on the photodiode is given by:

$$\tilde{U}_{out}(f) = T(f) \sqrt{\tilde{I}_{shot}^2 + \tilde{I}_{el}^2} \quad (2.16)$$

Here,  $\tilde{I}_{shot}$  is the shot noise of the light,  $\tilde{I}_{el}$  the equivalent input current noise of the circuit and  $T(f)$  the transfer function of the photodiode. The output voltage dark noise with no light incident on the photodiode is:

$$\tilde{U}_{dark}(f) = T(f) \tilde{I}_{el} \quad (2.17)$$

By dividing the equations for  $\tilde{U}_{out}$  and  $\tilde{U}_{dark}$ , the transfer function cancels out:

$$\frac{\tilde{U}_{out}}{\tilde{U}_{dark}} = \frac{T(f) \sqrt{\tilde{I}_{shot}^2 + \tilde{I}_{el}^2}}{T(f) \tilde{I}_{el}} \quad (2.18)$$

And solving for  $\tilde{I}_{el}$  gives:

$$\tilde{I}_{el}(f) = \frac{\tilde{I}_{shot}}{\sqrt{\left(\frac{\tilde{U}_{out}}{\tilde{U}_{dark}}\right)^2 - 1}} \quad (2.19)$$

Measurements of the input current noise using this relation are shown in the next section.

Another noise source is digitization noise. This depends on the voltage corresponding to one least significant bit  $U_{LSB}$  and the sampling frequency  $f_s$  [33]:

$$\tilde{U}_{dig} = \frac{U_{LSB}}{\sqrt{6}f_s} \quad (2.20)$$

### Pathlength noise

The linear spectral density of pathlength noise  $\tilde{x}$ , given in  $\text{m}/\sqrt{\text{Hz}}$ , measured in the interferometer depends on the phase noise  $\tilde{\phi}$ , given in  $\text{rad}/\sqrt{\text{Hz}}$ , and the laser wavelength  $\lambda$ :

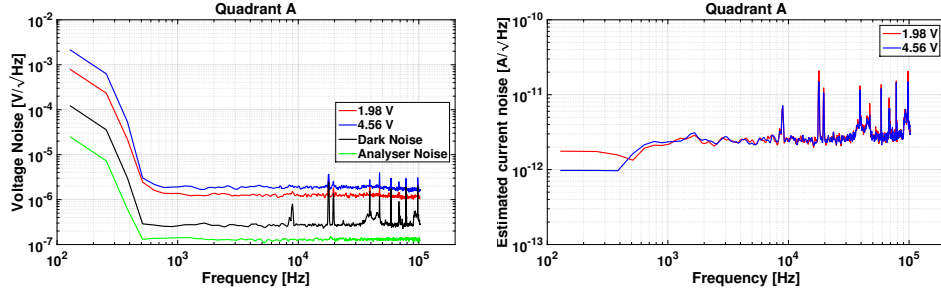
$$\tilde{x} = \frac{\lambda}{2\pi} \times \tilde{\phi} \quad (2.21)$$

The same relation is true for converting a length change  $\Delta l$  into a phase shift  $\Delta\phi$ .

For the LISA optical bench testbed the photoreceiver noise was calculated during the design to ensure this is not the limiting noise source. The testbed was designed to provide a picometer stability even if that was not necessary for the TTL coupling investigations. The power budget for the photodiodes is given in [34], they are given by the available laser power at the fiber couplers inside the vacuum tank and the passed beam splitters. The defined requirement on the output power at the fiber couplers was based on the available laser power and the properties of the modulation bench like the efficiency of the AOMs and the losses at the fiber couplers.

The signal amplitude is then given by the heterodyne efficiency and the photodiode efficiency. For the heterodyne efficiency – given by the mode overlap of the two interfering beams – a typical value of 0.8 was assumed which is easily possible with a reasonably well aligned interferometer. The photodiode efficiency is dependent on the type of photodiode. For an InGaAs photodiode like the GAP1000Q from GFD Optoelectronics it is 0.7 A/W. This is a quadrant photodiode and it is used here in the science interferometer. For silicon photodiodes the efficiency at 1064 nm is lower, only 0.3 A/W for the PC50-7 from First Sensor. The single element photodiodes used here are all silicon diodes. The larger quadrant photodiode QP22-Q from First Sensor used in the reference interferometer is also a silicon diode but with an optimized efficiency for the near infrared. At 1064 nm it has an efficiency of 0.55 A/W. A complete list of photodiodes built into the experiment can be found in the design document [34].

For the electronic noise an input current noise of  $3.5 \text{ pA}/\sqrt{\text{Hz}}$  was assumed. This assumption was verified with one photodiode, the QP22-Q. For this photodiode and the TIA built into a LISA Pathfinder style phasemeter [27], the input current noise was measured using equation (2.19). The output voltage of the TIA was measured with a spectrum analyzer. The dark noise without



(a) Voltage noise measured for two different light levels with different output voltages, the voltage dark noise and the analyzer noise.

(b) The input current noise estimated with the measured voltage noise according to equation (2.19). Except for the high frequency peaks the noise is at the expected  $3.5 \text{ pA}/\sqrt{\text{Hz}}$ .

Figure 2.6

any light incident on the photodiode and the noise spectrum with a shot noise limited light source – a simple white light bulb. According to equation (2.19) the input current noise was then calculated using these measurements, the resistor in the TIA was  $5 \text{ k}\Omega$ . In fig. 2.6 the results for one segment are plotted showing the expected noise of  $3.5 \text{ pA}/\sqrt{\text{Hz}}$ . The voltage noise was measured for two different light levels, the dark noise of the photoreceiver was measured and the noise of the spectrum analyzer. The input current noise was then calculated for the two different light levels that is nearly identical as expected. The peaks at high frequencies are already present in the dark noise.

For calculating the digitization noise according to equation (2.20) the sampling frequency of the analog-to-digital converter (ADC) and the voltage corresponding to the least significant bit  $U_{LSB}$  is needed:

$$U_{LSB} = \frac{U_{max} - U_{min}}{2^n} \quad (2.22)$$

Where  $n$  is the number of bits. The phasemeter used here is using the ADC card FMC116 by 4DPS. This provides 14 bits and a differential voltage reference of  $\pm 3.3 \text{ V}$ . It is operated with a  $80 \text{ MHz}$  sampling frequency ([35], [28]).

These noise contributions are uncorrelated and add up quadratically:

$$\tilde{x} = \frac{\lambda}{2\pi} \frac{\sqrt{\tilde{I}_{dig}^2 + \tilde{I}_{el}^2 + \tilde{I}_{shot}^2}}{A_{het}} \quad (2.23)$$

For this experiment the total pathlength noise contribution from shot noise, electronic noise and digitization noise is less than  $1 \text{ pm}/\sqrt{\text{Hz}}$  for all photodiodes. Another noise source not calculated here is due to the relative

intensity noise (RIN) of the laser. The effect of RIN is calculated in [23]. However, it is expected that the coupling is a little different from what was assumed there [36]. A table with some calculated numbers can be found in appendix A.

## 2.4 Tilt-to-length coupling

Tilt-to-length (TTL) coupling is one of the largest noise sources in the expected noise budget for a spaceborne gravitational wave detector like LISA. There is a contribution from the science interferometer where the beam received from the distant spacecraft tilts relative to the local beam because the local spacecraft rotates. And there is a contribution from the test mass interferometer resulting from residual test mass jitter.

TTL coupling is nearly always present in interferometers, except for a few special cases like [37]:

- The point of rotation is exactly in the center of the wavefront curvature.
- The beam parameters of the interfering beams are identical and both beams are detected completely (large single element photodiode).

In most cases TTL coupling is present in an interferometer. There are different mechanisms which cause the coupling and depending on the geometry and the beam parameters, different mechanisms can be dominant. The following mechanisms can cause TTL coupling (the mechanisms relevant for this thesis are discussed in more detail below):

- Geometric coupling: when the point of rotation is not on the photodiode surface.
- Beam parameter mismatch, leading to different wavefront curvatures of the beams.
- Non-complete detection of the beams: clipping at the photodiode or any other component.
- Wavefront errors
- Variations in the intensity or the photodiode efficiency

The most obvious TTL coupling mechanism is the geometric effect. When the beam rotates around a pivot that is not on the photodiode surface, the measured path length is getting longer with increasing angle. This is depicted in fig. 2.7. In the case of the science interferometer, the beam will tilt around a pivot in the pupil plane of the telescope that will be in the RX aperture. In the case of the test mass, the beam will tilt around the same point as

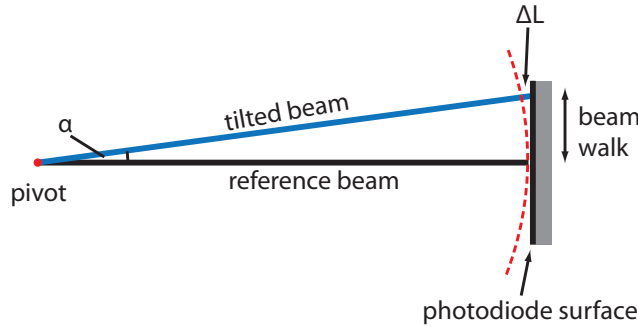


**Figure 2.7:** Sketch to illustrate the geometric tilt-to-length coupling.  $\alpha$  is the angle of the tilted beam,  $\Delta L$  the additional path length measured and the beam walk is the lateral offset on the photodiode surface.

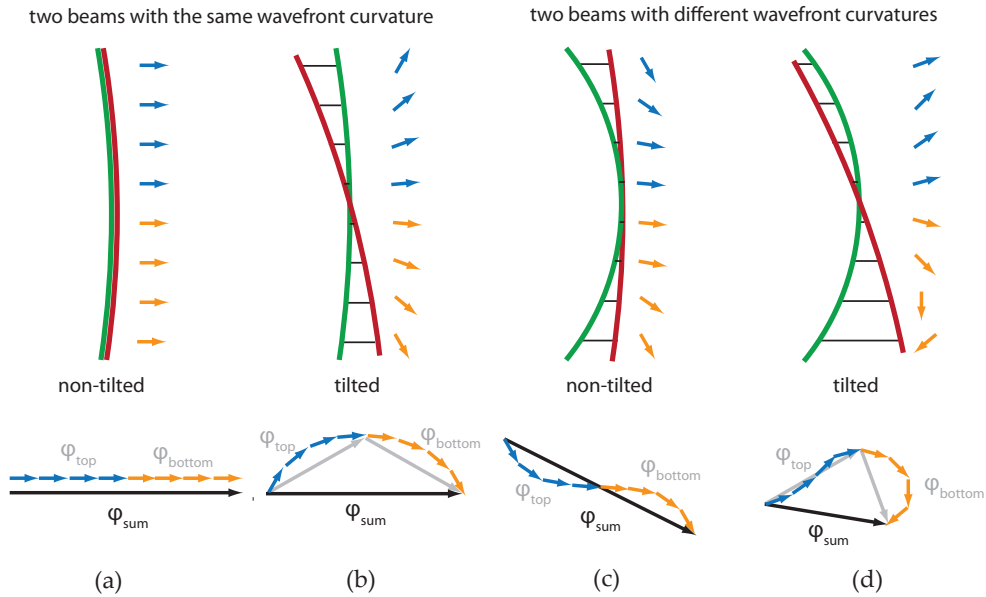
the test mass causing the tilt. One special case in which this TTL coupling is vanishing is when the waist of the beam is exactly at the pivot. Then the wavefront curvature radius is the same as the distance of the photodiode surface to the pivot. One can say the phase center is at the pivot. This is why the geometric TTL coupling is also sometimes described as an 'phase center offset' (for example in [38]).

Another phenomenon causing TTL coupling is due to beam parameter mismatch [39]. In fig. 2.8 different scenarios are sketched to explain this effect qualitatively. Different beam parameters means different wave front curvatures for the interfering beams on the photodiodes. A fixed wavefront (green) is interfered with a tilting wavefront (red). The blue and yellow arrows are symbolizing the local phase difference as phasors between the two beams. The length of the arrows is the amplitude (assumed to be constant over the whole beam for simplicity) and the angle is the phase of the signal. Underneath, the sum of the phasors is depicted. The black arrows show the total phase  $\varphi_{sum}$  on the photodiode, the grey arrows show the sum on the top and the bottom half.

Fig. 2.8(a) shows the case of two identical wavefront curvatures and no tilt. The measured phase is the same at every point of the photodiode (blue and yellow arrows).  $\varphi_{sum}$  (black arrow) is the total phase measured, depicted here as the sum of the phasors over the photodiode surface.

Fig. 2.8(b) one beam is tilted and there is an angle between the two interfering wave fronts. The phase difference between the wave fronts is not the same at every point of the photodiode anymore. The measured phase is again the sum of the phasors  $\varphi_{sum}$ . The phase change due to the tilt is symmetrical for both halves of the photodiode (depicted by the grey arrows). Therefore the total measured phase  $\varphi_{sum}$  is the same for the tilted (a) and the non-tilted case (b). What changes is the length of the phasor  $\varphi_{sum}$  that means the heterodyne amplitude is changing with the tilt angle.

Fig. 2.8(c) shows two wave fronts with different curvatures and no tilt. The phase is not the same at every point on the photodiode, the total phase is again the sum of the phasors  $\varphi_{sum}$ .



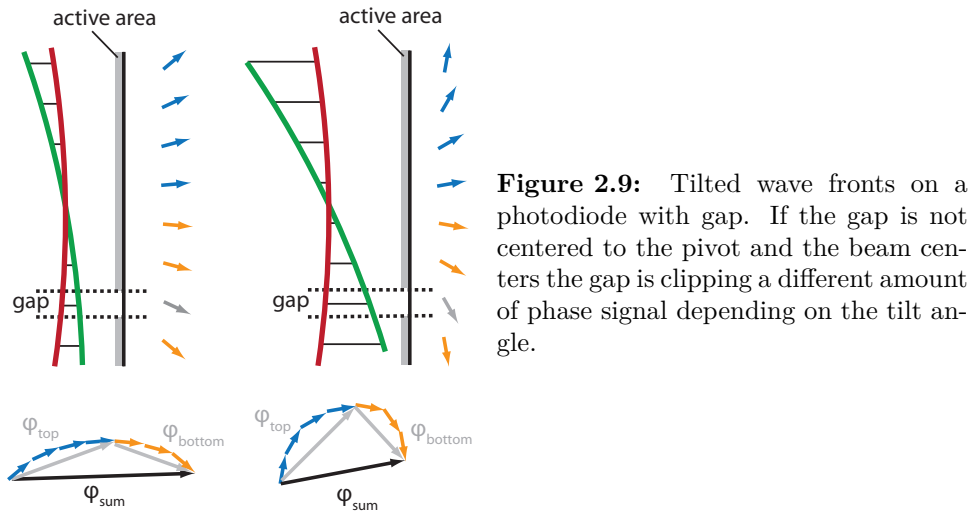
**Figure 2.8:** Sketch for qualitatively illustrating TTL coupling due to mismatched beam parameters. The blue and yellow arrows are symbolizing the local phasors at this position of the interfering beams. In a simplified picture, these phasors are added to get the signal  $\varphi_{sum}$  over the whole photodiode. The resulting phase signal is different for tilted and non-tilted beams with different wavefront curvatures, but not for beams with equal curvature. Here only the length but not the angle of the phasor changes. Sketch adapted from [39]

Fig. 2.8(d) shows two wave fronts with different curvatures where one beam is tilted. The phase change is not symmetric on the two halves of the photodiode and the total measured phase is different to the measured phase in the non-tilted case (c). That is symbolized here by the angle of the total phasor  $\varphi_{sum}$ . The angle is changing with a tilt of the wave fronts and thus the total measured phase is dependent on the tilt angle.

In this picture this can be explained by the different weighing of the signal on the two halves of the photodiode, depending on the phase difference being large or small. The arrows in grey are showing the sum over one half of the photodiode. In the case of two tilted beams with different curvatures (d) these signals are not symmetric like in the case with two tilted beams with equal curvature (b). The local heterodyne amplitude is not changing, but in the sum the larger phase difference on one half of the photodiode (here the bottom half) is reducing the total amplitude and changing the phase.

Clipping can also cause TTL coupling. The case of the clipping by the slits of a quadrant photo diode is discussed here and illustrated in fig. 2.9. The clipped part (grey phasor) is not contributing to the total phase  $\varphi_{sum}$ . If this phasor is changing with the tilt angle it changes the total phase. This effect can be avoided if the slit is aligned to the pivot (to the intersection point of





the two wave fronts) and no beam walk is present on the photodiode. Similar TTL coupling mechanisms can be caused by other clipping effects.

The TTL coupling can be calculated quantitatively for example with the optical simulation software IfoCAD ([25], [40]). With IfoCAD the photodiode signals can be calculated for different beam parameters, pivot positions and photodiode parameters. The effect of the slits of a QPD, clipping at the photodiode edges and clipping at simple apertures can also be simulated. More complex clipping effects and the propagation of clipped beams through components is more difficult and not always possible with IfoCAD.

## 2.5 Suppression by imaging optics

A way to reduce TTL coupling are imaging optics. By imaging the point of rotation on the photodiode surface the beam walk is removed and thus the TTL coupling decreased (see fig. 2.10). With an ideally designed and aligned imaging system only TTL coupling due to different wavefront curvatures remains. This can be achieved with a classic pupil plane imaging system but in the case of the LISA optical bench that needs to have at least four lenses to get a more compact design that fits on the bench. To save even more space a non-classical approach can be used with only two lenses and a non-collimated beam behind the imaging system. Both solutions have been tested to work for LISA. In part II of this thesis the designs and experimental investigations are shown and discussed.

In previous work a two-lens solution for the test mass interferometer was studied using optical simulations [24] and a table-top experiment [39]. In the experiment it was shown in a homodyne interferometer with equal beams that this type of imaging system in principle works for reducing TTL coupling.



**Figure 2.10:** Removing beam walk on the photodiode with an imaging system. The pivot is imaged on the center of the photodiode surface.

The experiment also showed some experimental difficulties to measure TTL coupling in an interferometer. One challenge is the tilt actuator. Some scheme is needed to prevent additional path length changes due to longitudinal motion of the actuator. The experiment also showed that higher order modes in the Gaussian beam induce TTL coupling.

# Design of the LISA optical bench testbed

In this section the concept and the design of the LISA optical bench testbed is described. The testbed consists of a minimal optical bench and the telescope simulator. The minimal optical bench has an interferometer representing the science interferometer for LISA and the telescope simulator is a second baseplate providing a representative RX beam for the science interferometer and a reference interferometer. The primary goal of this experiment was to investigate tilt-to-length coupling and test imaging systems for the science interferometer.

This testbed was built within a project for ESA, in a collaboration of the AEI, the University of Glasgow (UGL) and Airbus Defense and Space in Friedrichshafen. The optical bench was constructed at UGL and the telescope simulator was constructed mainly in Hannover. Some critical bonding steps were done in Glasgow, too. The completed benches were then transported to Hannover and operated with the test equipment prepared in Hannover.

## 3.1 Concept of the test bed

The primary goal of the investigation supported by ESA was to test the suppression of tilt-to-length coupling by imaging systems in the science interferometer. This project evolved from the original optical bench project where it was planned to build an elegant breadboard (EBB) of the full LISA optical bench [38]. Most of the hardware and optical components for the EBB were already available at the time of the redirection of the project and used for the actual test bed. So the goal was to design a test bed for investigating tilt-to-length coupling in a way representative for a LISA-like mission using mostly the already available components. In addition it was designed to be

flexible for upgrades and further investigations to build a test bed useful for future work towards a LISA mission.

For this test bed not the full EBB was built but a minimal optical bench. The main part of the minimal optical bench (called optical bench or OB in the following) is the science interferometer that measures the distance between the local optical bench and the optical bench in the remote spacecraft. Therefore the local laser is interfered here with the received beam (RX beam) coming from the distant spacecraft. To operate the science interferometer in the lab a simulated RX beam beam is needed that is provided by the telescope simulator. In fig. 3.1 a schematic of the setup is shown.

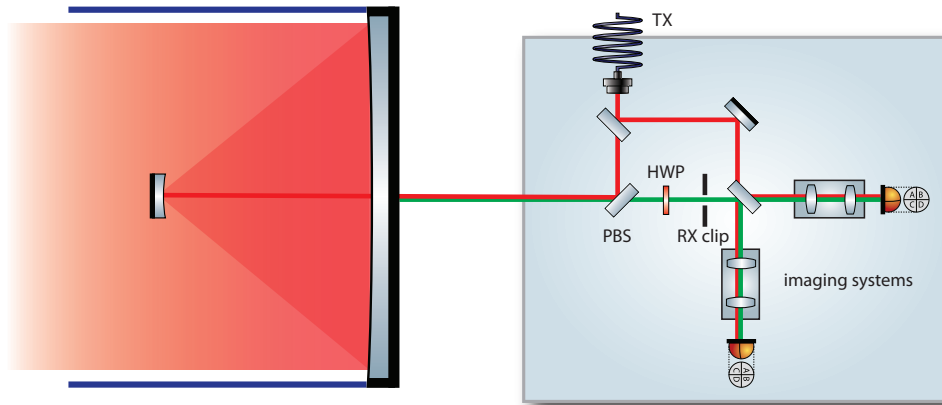
The optical bench has the science interferometer where three beams are interfered. The local beam that is transmitted (TX beam) through the telescope to the distant spacecraft is shown in red, the RX beam in green and the local oscillator (LO beam) in blue. The LO is used as an alignment and phase reference beam. In front of the science interferometer photodiodes the imaging systems are placed. The PBS and the waveplate are to send a part of the TX beam to the telescope and to receive the RX beam on the same optical axis. The polarization of the TX beam is rotated from s-pol to p-pol to allow the separation of the beam path again. Using polarizing optics in precision interferometers was shown to be compatible with picometer noise in [41]. The RX aperture is placed in the pupil plane of the telescope. This is defined as the interface between the optical bench and the telescope.

Instead of the telescope there is a second baseplate, the so-called telescope simulator. It provides the RX beam that can be tilted via two piezo driven actuators and has a flat-top beam profile to be as representative as possible for the actual received beam on a LISA spacecraft. Its polarization is changed before it is going to the OB and one part is going to the reference interferometer that is on the telescope simulator baseplate. The output ports of the reference interferometer are used for reference photodiodes and a phase camera for beam diagnostics. In addition the telescope simulator has a second beam, the local oscillator (LO beam), that is combined with the RX beam path and serves as a stable reference. It defines the zero angle position of the RX beam and is used to measure and/or compensate the parasitic longitudinal motion of the tip-tilt actuators.

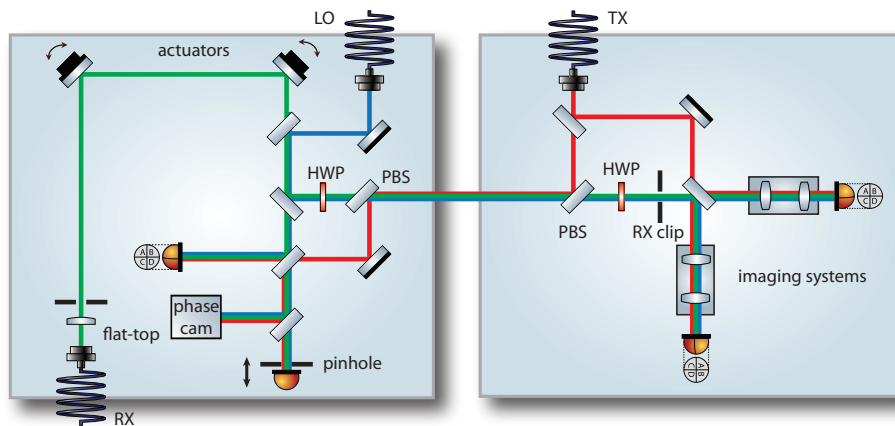
## 3.2 Detailed design of the optical bench

The design and construction of the OB was mainly done by the University of Glasgow and Airbus DS. It is described here to get an overview over the whole experiment.

In fig. 3.2 the layout of the OB is shown with a picture produced with the software OptoCAD. The round baseplate is 58 cm in diameter and was originally intended to be used for an elegant breadboard (EBB) of the optical



(a) Schematic of the OB with the science interferometer and the telescope.



(b) Schematic of the OB and the telescope simulator.

**Figure 3.1:** In (a) the OB with the science interferometer is shown. In the science interferometer the distance to the distant spacecraft is measured with the local TX beam and the RX beam received from the distant optical bench through the telescope. In (b) the telescope is replaced by the telescope simulator, providing the RX beam. The RX beam is tilted via two actuators to investigate tilt-to-length coupling in the science interferometer where this effect is suppressed by imaging optics. The telescope simulator also provides a reference interferometer and the LO beam, a stable reference beam. The light is exchanged between the two benches via periscope optics and separated by polarizing optics. The RX aperture is in the pupil plane of the telescope and is defined as the interface between telescope and OB.

bench for the joined ESA and NASA LISA mission. The design goal in this work was to build a minimal optical bench (MOB) mainly consisting of a science interferometer with the imaging systems to investigate. In addition a CQP (calibrated quadrant photodiode pair) was included for easier alignment.

The baseplate has a hole in its center intended for the test mass interferometer, but not used in this experiment. Next to it a  $45^\circ$  out-of-plane mirror is the interface to the Telescope Simulator. The TX beam is reflected upwards from the plane of the optical bench optics and the RX beam coming from above is reflected down into the OB optics plane. To separate the two beams a polarization beam splitter (PBS2) and a half waveplate (HWP) are used. In the upper left corner the TX fiber injector is placed. The beam is polarization cleaned by a PBS (PCO3) and a power monitor photodiode (TX PWR) can be used for monitoring or stabilizing the laser power in the beam. The beam splitter BS2 is splitting the beam into the beam sent to the telescope simulator and the one for the science interferometer. After passing several mirrors one part of the beam is then interfered at the recombination beam splitter BS21 with the RX beam. The polarization of the beam going to the Telescope simulator from BS2 is rotated from s-polarization to p-polarization and transmitted through PBS2.

The RX beam coming from the telescope simulator is s-polarized and reflected by PBS2. BS23 is a 60/40 beam splitter sending 40% of the light to the CQP photodiodes and 60% to the science interferometer. In the path to the science interferometer the RX aperture is placed in the pupil plane of the telescope. This point is defined as the interface point between telescope assembly and OB. BS21 is the recombination beam splitter of the science interferometer where the TX and the RX beams are interfered. On both output ports QPDs are placed for reading out the interferometer signal. In front of the QPDs imaging systems are suppressing the tilt-to-length coupling. The imaging systems are placed on separate baseplates and can be removed or replaced. In this schematic two different designs of imaging systems are shown in the two output ports.

The position of the telescope simulator baseplate on top of the OB is depicted as a dashed outline. The additional squares are the feet on which the telescope simulator stands. The three extra feet positions mark the position of the telescope simulator in the flipped position, which is used to align the reference photodiode on the telescope simulator.

**FIOS** The FIOSs (fiber injector optical sub-assemblies) used for this experiment were developed and built at UGL [42]. The design is based on the FIOS for LISA Pathfinder [43] which were successfully used in that mission. The main difference is that the FIOSs for this experiment do not have a free space between the fiber end and the lens. The beam is only propagated in fused silica to prevent any damages of the fiber end due to contamination. This

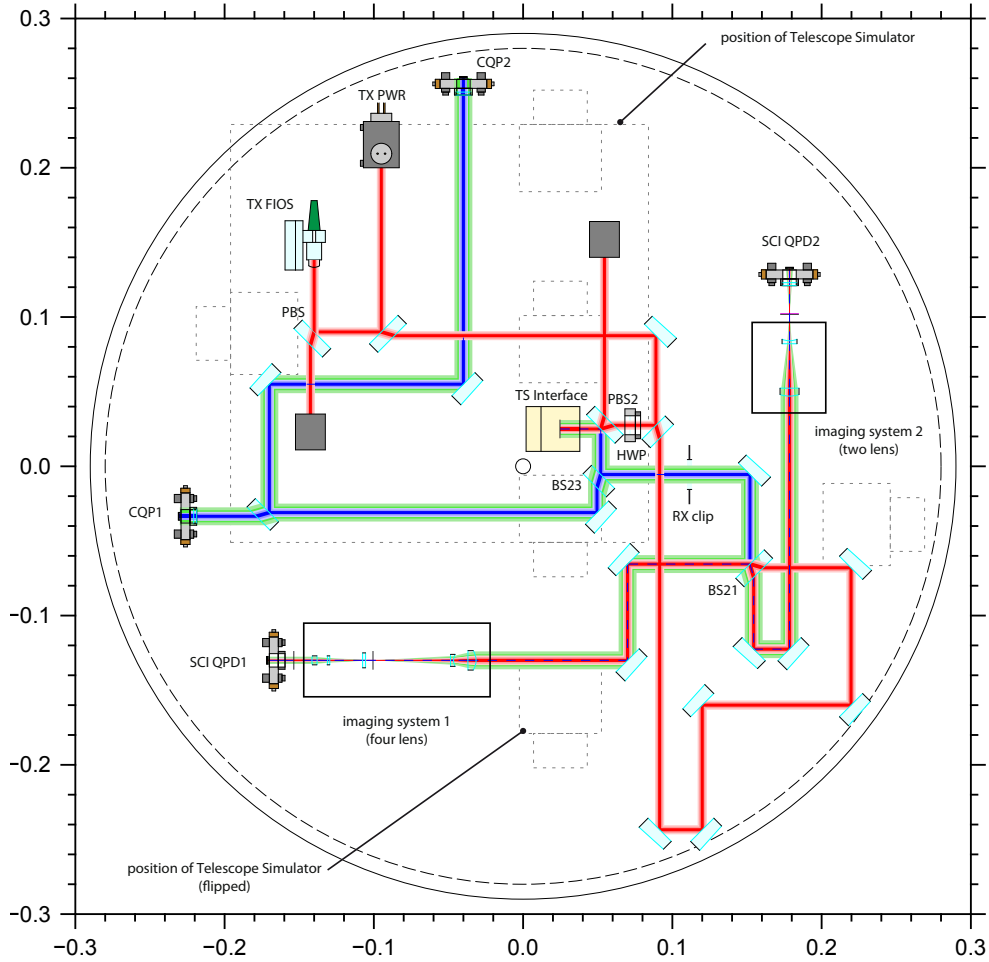


**Figure 3.2:** Layout of the OB with the key components labeled. The TX beam (red) is launched on the OB and interfered at BS21 with the RX beam (green) from the telescope simulator. The imaging systems are placed in both output ports of the science interferometer and mounted on separate baseplates which can be removed. Here two different imaging systems (two-lens and four-lens) are depicted in the layout. The RX beam and the LO beam (blue) are coming from the TS baseplate via the out-of-plane optic labeled TS interface. A part of the beams are going to the CQP photodiodes for position read out, the other part to the science interferometer photodiodes (SCI QPDs). The TX beam polarization is rotated by a half wave plate (HWP) so that the beam is transmitted through the PBS and going to the TS via the TS interface. The dashed outline is marking the position of the TS baseplate and feet in the nominal position. The additional dashed boxes are marking the TS feet in the flipped position.

is necessary for LISA because higher laser power will be used than for LISA Pathfinder.

### Opto-mechanics

The opto-mechanics were mostly designed by Michael Perreur-Lloyd at UGL. The detailed design of the imaging system mechanics, the photodiode mounts, the power monitor mounts, the waveplate mounts and the beam dumps is documented in [34] and reported in [44] and [42]. The photodiode mounts and the beam dumps are also used for the telescope simulator.

All metal parts are in contact with the Zerodur<sup>®</sup> baseplate via flexure feet or isostatic mounts to prevent stress in the parts. The mounts glued to the baseplate have three flexure feet designed such that the front surface of the mount is not moving but it is extending backwards. The feet are glued onto a piece of Kapton<sup>®</sup> tape so that the parts can be removed by removing the tape. This provides flexibility to the setup and the thin tape is not spoiling the stability. The parts clamped to the baseplate – imaging systems and science interferometer photodiode mounts – are mounted isostatically via three ball bearings.

**Photodiode mounts** The photodiode mounts are adjustable in the two lateral directions. The photodiodes are glued into different sized MACOR spacers for electric isolation which are screwed to the mount. The adjustment range is approximately  $\pm 150 \mu\text{m}$  with fine pitch screws. In the science interferometer the MACOR spacer were replaced by POM spacers with elongated holes for the screws holding them to the mount. With these elongated holes the position of the photodiode can be adjusted roughly with a bigger adjustment range of  $\pm 1 \text{mm}$ .

**Imaging system mechanics** The mechanical mounts for the imaging systems were designed by Michael Perreur-Lloyd at the UGL. The detailed design is documented in [34]. The aim of the design was to get a very flexible mount to allow intentional misalignment of the lenses and to switch between different optical designs.

The mounts shown in section 3.3 have a common baseplate for all lens mounts (called super-baseplate) and individual mounts for either two or four lenses. The lens mounts can be adjusted in x, y, yaw, pitch and longitudinally along the beam axis. Two lenses together are mounted on an additional base that is adjustable longitudinally and horizontally on the super-baseplate.

The mounts are thermally compensated by using an aluminum and a titanium part to keep the center of the lens in a stable position and the lenses are glued at three points onto flexures in the mount to avoid stress.

The imaging systems are placed on the optical bench with the super-baseplate which has three ball bearings on the underside for a kinematic



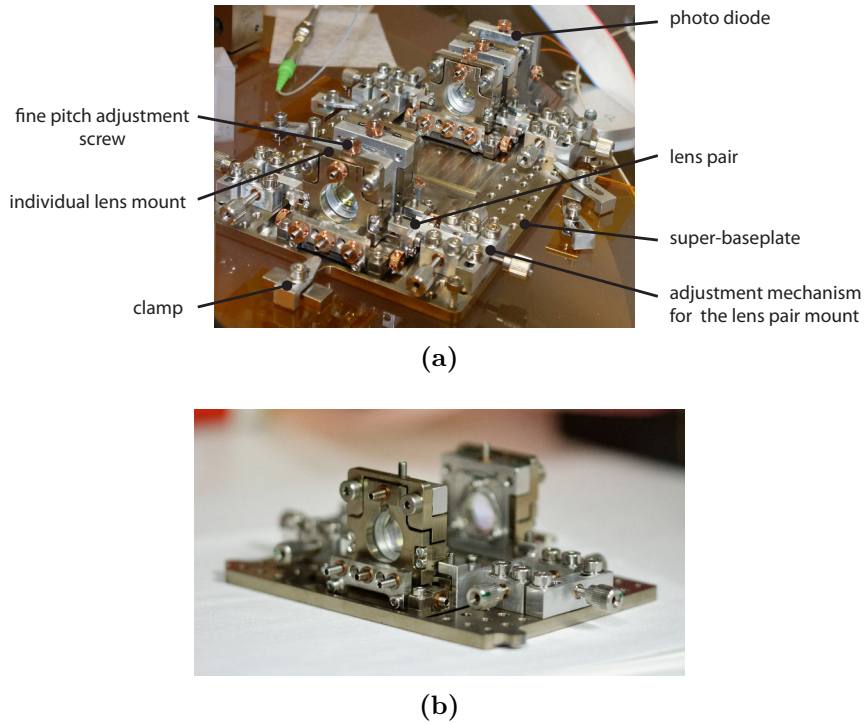


**Figure 3.3:** Photographs of the two different imaging system mechanics. (a) Four-lens imaging systems with two lens pairs and a photodiode mount. The key features are labeled. (b) Two-lens imaging system. The key features are the same but only one lens pair is places on a smaller super-baseplate.

mounting. It can be clamped with tie downs glued to the optical bench baseplate. The science interferometer photodiodes have a separate kinematic mount with an adjustment mechanism in x and y. They are clamped to the optical bench baseplate, too.

**RX clip mechanics** In the RX aperture on the OB a modified photodiode mount allows insertion of a physical aperture (RX clip or aperture) at this point. The magnetic mount, allowing exchange of apertures, was mainly developed by Michael Tröbs (see [45]). A photograph of the mount and an aperture is shown in fig. 3.4. The aperture is held by three spherical magnets which sit in slits to ensure a good positioning. For the calibration of the telescope simulator photodiodes are glued to the apertures. In pre-experiments it was tested that the apertures can be repeatedly positioned within a few microns with this mounting scheme ([45], [46]).

In this thesis the mount was used for the calibration of the TS described in chapter 6. It was not used to insert a RX clip. The defining aperture was the edge of the active area of the science interferometer photodiodes.

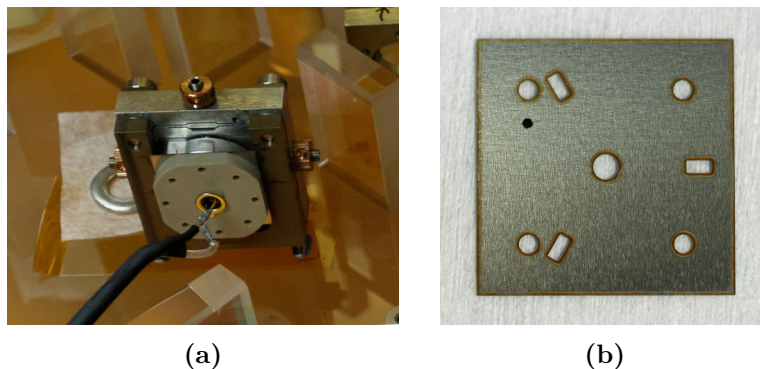


**Figure 3.4:** (a) Mount of the RX clip. Here a pinhole aperture is attached to the mount with a SEP glued to the aperture. This is mounted temporarily for the TS calibration. The aperture is mounted via three spherical magnets and can be exchanged by different apertures or removed. (b) One of the possible apertures for the RX clip mount. The slits are for positioning the clip accurately on the spherical magnets that hold the aperture.

### 3.3 Detailed design of the telescope simulator

The telescope simulator was designed to have a reference interferometer and to produce a simulated RX beam to operate the science interferometer on the optical bench. The RX beam is tiltable to investigate tilt-to-length coupling and a flat-top generator provides a RX beam representative for an actual RX beam coming in through the telescope. A second RX beam with a Gaussian beam profile is implemented to investigate tilt-to-length coupling with two Gaussian beams for the local interferometers (like the test mass interferometer). In fig. 3.5 the layout of the telescope simulator is shown. The detailed design with IfoCAD was mainly done by Ewan Fitzsimons and Sönke Schuster.

In fig. 3.5 the OptoCAD layout of the telescope simulator is shown. The dimensions of the baseplate are 280x280x35 mm. In the lower left corner the big fiber coupler for the RX flat-top beam and the FIOS for the RX Gauss are placed. The RX beam is the beam shown in green. The flat-top beam generator is described in more detail later in this section. On the 50/50 beam splitter BS12 both beam paths are combined, so that it is easily possible to alternate between using the two beams by turning one of them on and blocking the other one on the modulation bench. The two actuators in the corners of the baseplate tilt the RX beam around the center of the RX aperture on the optical bench.

The beam splitter BS1 is splitting the beam into a part going to the OB via the out-of-plane optic and a part going to the reference interferometer on the TS. BS11 is the recombination beam splitter of the reference interferometer, interfering the RX beam and the TX beam (red) coming from the optical bench. The TX beam is p-polarized when it enters the TS via the out-of-

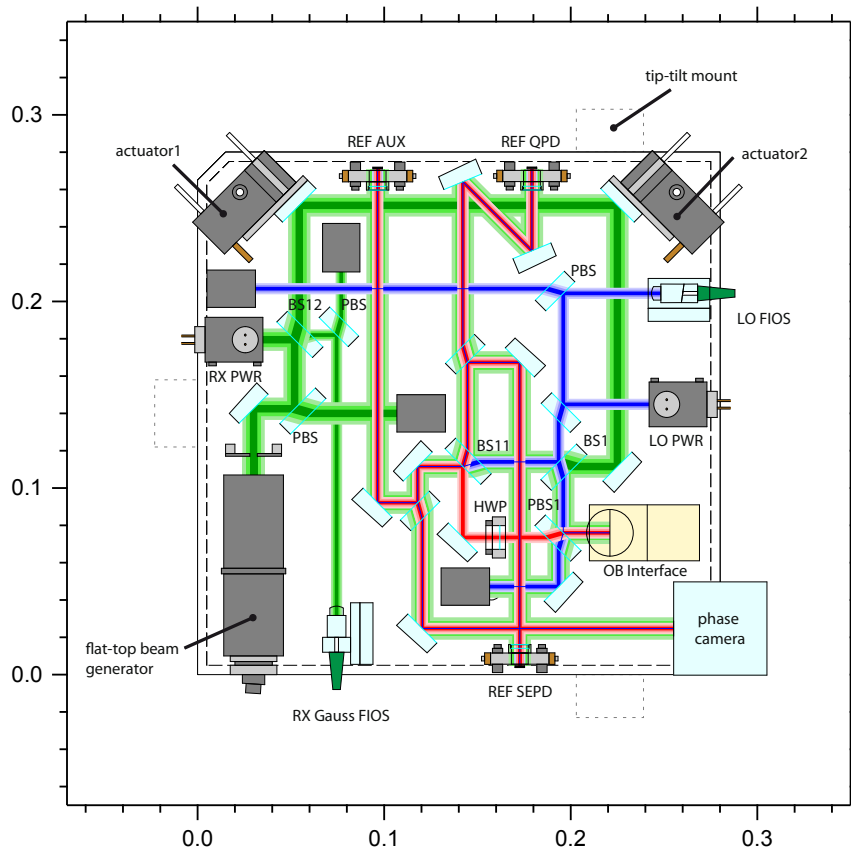


**Figure 3.5:** Layout of the telescope simulator with the key components labeled. The RX beam (green) is launched either by the flat-top generator or the FIOS and tilted via the two piezo actuators. The LO beam in blue is a stable reference beam combined with the RX beam at BS1. At BS11 these two beams are interfered with the TX beam (red) from the OB, coming to the TX via the OB interface. The reference interferometer output ports are split again to get four ports, which are equipped with a QPD (ref QPD), a small pinhole diode (ref SEPD), a large single element diode (aux SEPD) and a phase camera. The dashed outlines indicate the position of the feet for the tip-tilt mount.

plane optic. Therefore it is transmitted at the PBS1 and the polarization is rotated back to s-pol by the HWP before the recombination beam splitter.

The LO beam is shown in blue and it is combined with the RX beam at the beam splitter BS1. It is in s-pol, too and takes the same path as the RX beam after this beam splitter.

The power monitor photodiodes (PWR) are placed behind all fiber couplers to allow a monitoring of the output power. Polarizing beam splitters clean the polarization directly after the fiber couplers before the power monitors.

Both output ports of the recombination beam splitter BS11 are split again to get four output ports. Three different photodiodes and a phase camera are placed in the output ports at the same distance from the recombination beam splitter. This distance puts the photodiodes in the optically equivalent position as the RX aperture. That means the RX beam also tilts around the center of each of the photodiodes and the phase camera.

The reference QPD (ref QPD) is a quadrant photodiode to read out the position of the RX beam. It can be disentangled from the other beams by an amplitude modulation. This signal is used to control the actuators and ensure that the beam is tilted around the center of this photodiode and therefore the center of the RX aperture. The reference pinhole SEPD (ref SEPD) is a single element photodiode with a small  $150\ \mu\text{m}$  diameter pinhole in front of it. This pinhole is small enough to be an approximation of an infinitesimal small pinhole, which does not see any tilt-to-length coupling if it is placed in the point of rotation, because the wavefront curvature is negligible on a small scale (see section 2.4). The RX beam and the TX beam are offset phase-locked to the LO beam on this photodiode. This removes any phase noise induced before entering the interferometer (optical fibers, longitudinal movement of the actuators etc) and it also removes the TTL coupling of the telescope simulator because the photodiode is at the optically equivalent position as the RX aperture which is defining the interface between TS and OB.

The auxiliary SEPD (aux SEPD) is a big single element photodiode and the phase cam an InGaAs camera which can be used for monitoring the phase profile of the interfering beams (see [47] for more details and measurements with the phase camera).

**Tip-tilt mount** The telescope simulator is gravity mounted on the optical bench baseplate. The dashed outline in the layout (see fig. 3.5) marks the position of the three feet of the TS. The feet have two Zerodur<sup>®</sup> parts which are clamped together by a spring loaded screw (see fig. 3.6). This design was developed by Airbus DS. The upper part is a Zerodur<sup>®</sup> block bonded to the underside of the TS baseplate. The lower part is another block with a round base to have a point-like support area. The two parts can slide along their connection surface if the spring loaded screw is loosened. With the adjustment



**Figure 3.6:** One of the adjustable feet for the tip-tilt mount to align the telescope simulator baseplate. The upper Zerodur<sup>®</sup> block is bonded to the underside of the telescope simulator and clamped together with the lower Zerodur<sup>®</sup> block with a spring loaded screw. For adjusting the height of the foot the fine pitch screw in the metal bracket on top of the lower block pushes on the lower block and the two Zerodur<sup>®</sup> parts slide against each other when the spring loaded screw is loosened.

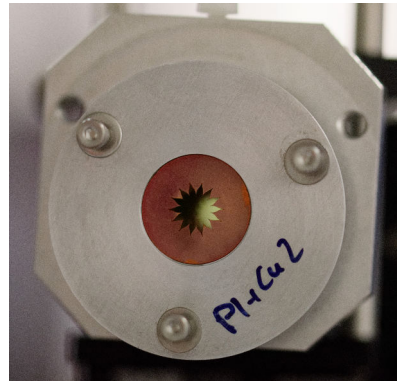
screw pushing on the lower part the length of the foot can be adjusted and thereby the height and tilt of the TS baseplate. When the spring loaded screw is tightened the adjustment screws can be retracted to get an all-Zerodur<sup>®</sup> connection between the TS and OB baseplates. The performance of this mount was tested and the results are presented in section 6.8.

**The actuators** The two actuators are piezo driven tip-tilt mirror mounts from Newport, type Agilis AG-M100LV6. They are vacuum compatible and have a range of  $\pm 2^\circ$  with an angular resolution of  $1 \mu\text{rad}$ . The step sizes are varying ([48]), so counting the number of steps cannot be used for determining the position and aligning the RX beam. Instead the DPS and DWS signals are used (see chapter 6).

The mirrors are not mounted in the space intended by the mount design. Instead they are glued to the actuators using an adapter plate. This ensures the correct height of the mirror and minimizes the parasitic longitudinal motion of the actuators by placing the center of the mirror in front of the rotation point of the actuators (see fig. 4.10 in section 4.6 for a picture of the assembly).

The actuators are screwed onto a mounting platform. Its three feet are glued on the baseplate. This mount has a thermally compensating design to suppress any thermally driven movement of the actuated mirror. This mount was designed by Airbus DS for the original LISA OB project where the actuators were planned to be used in the sensitive path of the interferometer. This is not necessary for the actual scheme where the actuators are not in the sensitive path. They were integrated anyway to reduce the risk of any temperature driven complications and to profit from the flexure feet to reduce temperature induced stress in the Zerodur baseplate. The thermally compensating design is described in detail in [16].

**Figure 3.7:** Photograph of the apodized aperture for the flat-top generator. The petals are shaped to achieve a Gaussian transmission profile from the inner radius to the outer radius where the petals end.



### The flat-top generator

The flat-top generator is an off the shelf fiber injector where the inner part of a large Gaussian beam is cut out by an aperture to get a beam with a quasi flat intensity and phase profile. The design was mainly done by Ewan Fitzsimons from Airbus DS. The mechanical parts were designed by Jan-Simon Hennig [34].

The fiber coupler is a 60FC-T-4-M100S-37 from Schäffter+Kirchhoff providing a big collimated Gauss beam with a 9 mm radius. The aperture has to be placed directly in front of the fiber coupler because the following optical components are not big enough for the 9 mm beam. To avoid diffraction and a destruction of the flat-top beam profile in the far field an apodized aperture design was chosen. This aperture has an inner radius with a clear aperture and a Gaussian transmission from the inner radius to the outer radius. This is achieved here by a accordingly shaped petals (see fig. 3.7). The shape was optimized using a Monte-Carlo simulation to get a flat intensity and phase profile in the inner 3 mm at the working distance of 80 cm, the distance from the apodized aperture to the RX aperture.

The metal tube of the fiber collimator is mounted by two rings which are glued with flexure feet to the baseplate. The mounting structure consists of an aluminum and a titanium part for thermal compensation. The center of the tube is kept at a constant height to reduce beam jitter. The structure has flexures in the longitudinal and the vertical direction to avoid stress.

The apodized aperture is fixed to the front of the tube of the fiber coupler. It was centered to the intensity maximum of the Gaussian beam using a WinCam.

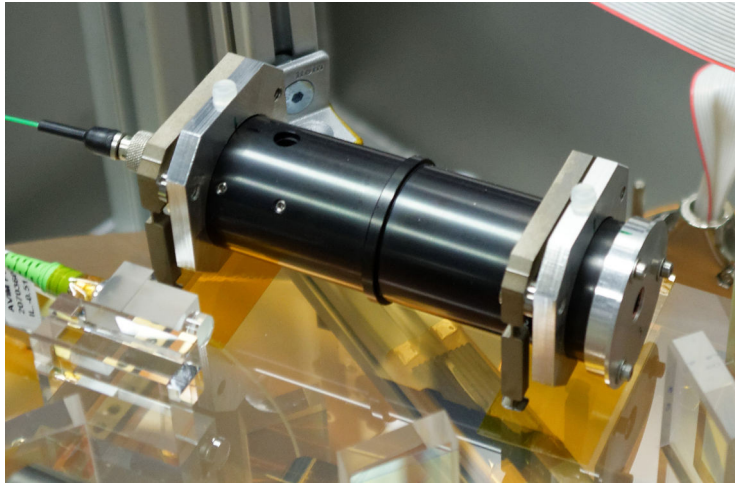


**Figure 3.8:** Flat-top generator. The black tube is a commercial fiber injector from Schäffter+Kirchhoff providing a 9 mm collimated Gaussian beam. On the front face the apodized aperture is aligned to the center of the big Gaussian beam. The mount for the flat-top generator consists of two thermally compensating parts to keep the center of the collimator at the same height above the baseplate. Flexures in the lateral and longitudinal direction reduce stress.





# Construction of the telescope simulator

The test bed was jointly built at the University of Glasgow and at the AEI in Hannover. In this chapter the construction of the telescope simulator is described, especially those construction steps that were done in Hannover within the scope of this thesis. The optical bench was constructed at the University of Glasgow as well as some critical components of the telescope simulator.

Both interferometer benches were constructed using the technique of hydroxide catalysis bonding. This technique is introduced briefly at the beginning of the chapter, as well as the used alignment methods. Next, the alignment plan and the bonding steps are described. The majority of the optical components were bonded using a template and a coordinate measuring machine to align the template. The RX fiber coupler was aligned by measuring the beam vector. In Glasgow, precision alignment techniques were used for the critical alignment steps to bond the recombination beam splitter and the LO reference beam. At the end of the chapter the integration of the metal mounts and parts – like photodiodes and actuators – is reported.

## 4.1 Hydroxide catalysis bonding

Hydroxide catalysis bonding is a technique to form chemical bonds between polished surfaces of material that can be oxidized and form, or attach covalently to, silicate-like networks [49]. This technique was developed for Gravity Probe B [50] and adopted for LISA Pathfinder. In LISA Pathfinder components of the optical bench and the FIOS were built using that technique [51] and it has proven to be a suitable technique to build complex optical systems

with great stability and alignment accuracy like interferometers for space applications [5].

Hydroxide catalysis bonding (in this thesis often referred to simply as 'bonding') was used for building this testbed, the optical bench and the telescope simulator. The experience and techniques developed at UGL mainly for LISA Pathfinder were used and adapted for this project. The bonding procedure and alignment techniques are introduced and summarized here.

**Bonding procedure** The two surfaces to be joined by hydroxide catalysis bonding need to be polished to at least  $\lambda/10$  surface flatness (defined for  $\lambda=632$  nm). Before applying the bonding fluid the surfaces get a final polish with cerium oxide and are cleaned with bicarbonate of soda and deionized water to remove any residuals of the cerium oxide. Directly before bonding the components have to be dried and dehydrated with a high purity grade methanol. The whole procedure is done in a clean room environment to prevent any contamination of the bonding surfaces.

The bonding fluid is a 1:6 solution of a sodium silicate solution (Sigma-Aldrich 338443) and deionized water. The bonding solution provides  $\text{OH}^-$  ions which etch the surfaces. Different solutions providing  $\text{OH}^-$  ions can be used. A silicate-like network based on siloxane bridges then forms between the surfaces [50]. The solution is filtered with a micro filter before use and applied to the bonding surface with a precision pipette. The amount used is 0.4 - 0.6  $\mu\text{l}/\text{cm}^2$ . Before applying the bonding fluid and joining the components a last inspection for any contamination with a white light source is crucial even in the clean room environment.

The bond starts to form after approximately 2 min, so the final alignment has to be fairly quick. If this final alignment fails, it can be tried to remove the component. Removing the component after 2 min, if possible, usually leads to surface damages. To stop the chemical reaction the bond should be flooded with water and the components rinsed extensively. A bottle of water was prepared for an emergency but none of the bonds during the construction of the telescope simulator had to be disassembled after the bonding solution was applied.

**Alignment methods** For building this testbed mainly alignment methods developed for previously built precision interferometers – like the LISA Pathfinder OBI [52] – were used. Other previously built interferometers for lab experiments are for example the Hexagon interferometer [53], the polarization optics interferometer [41] and the suspension platform interferometer [54]. Some mirrors and beam splitter have to be bonded with a few  $\mu\text{m}$  precision and precision alignment techniques are necessary. For the majority of optical components a precision of approximately 50 $\mu\text{m}$  is sufficient. These compo-

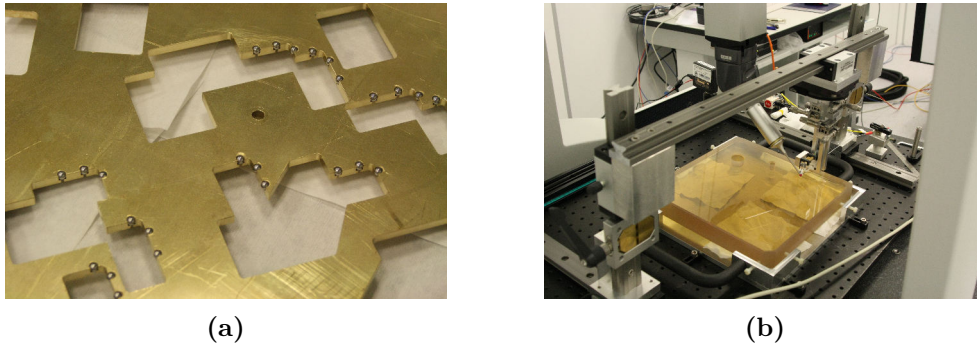


**Figure 4.1:** Template bonding and CMM assisted alignment. The template (a) has precisely machined pockets for the components with three ball bearings defining the alignment. In (b) three adjustable ball bearings are allowing aligning the component. Here it was used for the RX Gauss FIOS to align the beam orientation with the CMM. This bridge to access any point on the base plate was built for a previous experiment [53].

nents can be bonded by template bonding. Both techniques are reported in [52].

Template bonding uses a brass template with ball bearings which define the position of the components. Two ball bearings define the angle and position of the front surface of the components and a third one at the short side ensures that the beam hits the component in the center. The precision achieved with this alignment method is limited by manufacturing tolerances of the template [52]. The orientation of the template on the baseplate can be optimized for reducing these tolerances (see section 4.4).

For the precision alignment a CQP (calibrated quadrant photodiode pair) is used as described in [55]. This target, consisting of two quadrant photodiodes at different distances, allows to measure the beam vector to a high precision of  $\pm 4\mu\text{m}$  and  $\pm 20\mu\text{rad}$ . This technique was used at UGL for the critical alignment steps (see section 4.5).

For the RX Gauss FIOS an adjustable alignment tool developed for previously built precision interferometers ([53]) was used. Here three ball bearings for positioning a component are mounted on multiple translations stages to adjust the angle and position.

## 4.2 Optical components

For building the minimal optical bench and the telescope simulator the components originally purchased for the elegant breadboard design of the optical bench were used. The mirrors, beam splitters and polarizing beam splitters were manufactured by ICOS and the requirements are based on the experience from the LISA Pathfinder optical bench. The bonding surfaces are polished

to better than  $\lambda/10$  and the perpendicularity of the bonding surface to the optical surface is better than 1 arcsec. This angle defines how well the interferometers can be aligned because this angle cannot be adjusted and depends on the manufacturing tolerances. A detailed analysis and component description is given in [19].

The beam splitters are parallel to avoid beam jitter noise, but the mirrors are wedged to avoid reflections from the back surface back into the beam path. The tolerance of the wedge angle is small enough to allow to use also the back surface for template bonding (measured by UGL).

The components have various different coatings for mirrors, polarizing beam splitters and beam splitters with different splitting ratios. A complete list of different sizes and coatings can be found in [19].

### 4.3 Alignment plan for the Telescope Simulator

In this section the alignment plan for the TS is described. The actual construction is reported in the next section.

The TS baseplate is a 28 cm by 28 cm Zerodur plate with a thickness of 35 mm. Both sides are polished for bonding and it has two holes – one for the beams going to the optical bench and back and the other one was intended for a test mass interferometer, but not used in the redirected project. Two corners are cut off because they were damaged during the polishing at the manufacturer. The baseplate was provided by Krombach KG.

**First step** The first component to be bonded was the RX Gauss FIOS provided by UGL. It was aligned using the position of the beam with regard to the baseplate. As the reference coordinate system the surfaces of the baseplate were used, this ensures the correct position of the through hole for the interface to the OB. The orientation of this FIOS is not very critical because the actuators define the final alignment of the beam in the interferometers. The required accuracy is better than 3.5 mrad and less than 1 mm offset.

**Second step** The second and thirds steps were to bond the non-critical components with templates. In the second step the first half of the 18 components was bonded. Because of the tight spacing between the components it was not possible to bond all 18 components with one template. It also takes too long to bond so many components in one session. The components for the first template were chosen in a way that the components closest together were bonded with different templates.

**Third step** The second batch of non-critical components were bonded. The inclination of the baseplate and the template was rotated by  $90^\circ$  to allow

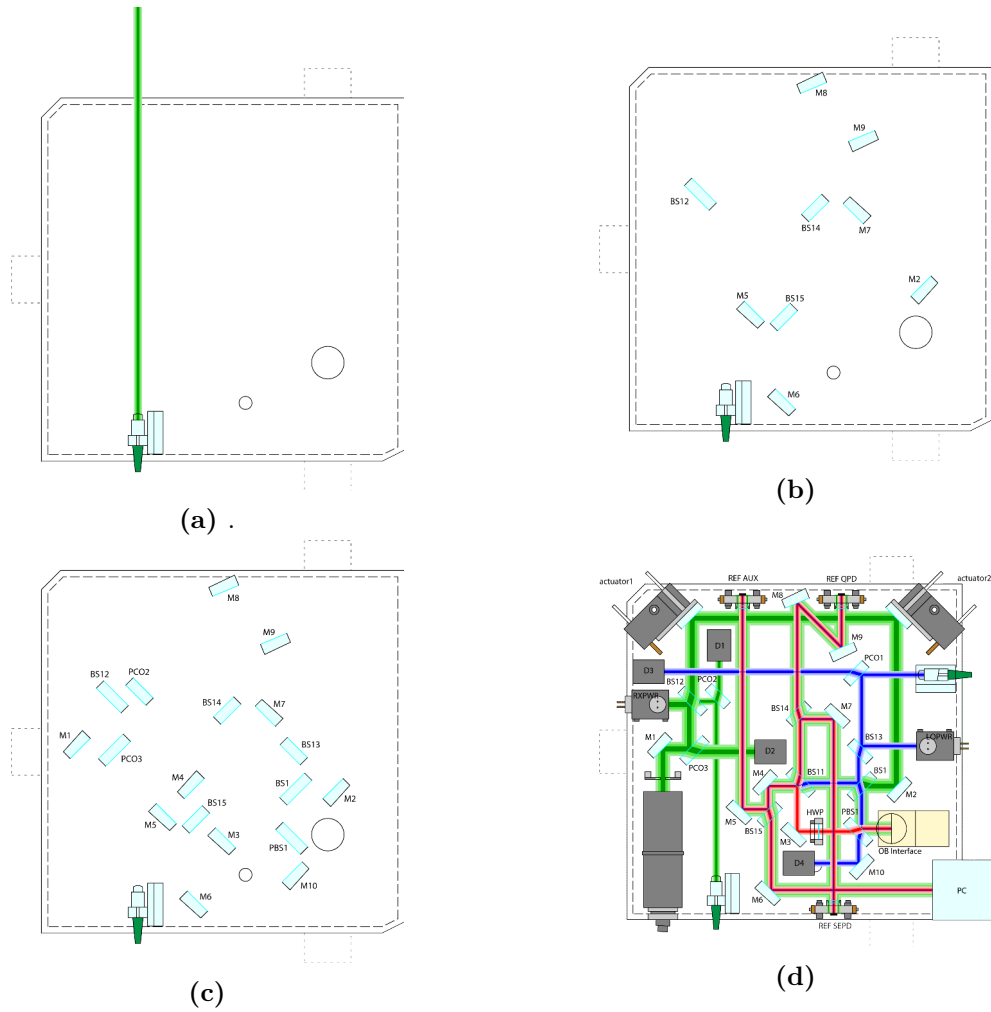


**Figure 4.2:** Construction steps for the telescope simulator. (a) Alignment and bonding of the RX Gauss FIOS. (b) First batch of 9 components bonded with a template. (c) Second batch of 9 components bonded with a template. (d) Finished telescope simulator (see fig. 3.5 for a larger picture). Some critical alignment steps were done at UGL. Back in Hannover the photodiodes and other glued parts were integrated.

a different orientation of the ball bearings for positioning. The  $\lambda/2$ -waveplate was aligned in its mount and glued to the baseplate.

**Fourth step** The TS was shipped to UGL. There the LO FIOS and the missing beam splitters were bonded using their CQP alignment tool ([55]). Also the ref SEPD was glued and the three feet for the tip-tilt mount were bonded to the underside of the baseplate.

**Fifth step** The TS was shipped back to Hannover. The remaining photodiodes were glued to the baseplate. The LO beam was used for the alignment. The big SEPDs, the aux SEPD and the power monitors, were aligned to not clip the beam. The ref QPD was centered on the beam, the positioning accuracy has to be well within the adjustment range of the mount.

The beam dumps were glued using the LO beam for positioning.

**Sixth Step** The flat-top generator and the actuators were glued to the baseplate. For the positioning, a beam splitter and two QPD were placed at the output port for the phase camera – one QPD close to the beam splitter and one further away. The QPDs were centered to the LO beam and then the RX beam was centered to the QPDs for aligning the actuators. The RX flat-top beam was aligned to the RX Gauss beam afterwards.

## 4.4 Template bonding of non-critical components

In this section the integration of the RX Gauss FIOS and the template bonding of the non-critical components is described. For the alignment a coordinate measurement machine (CMM) was used. The CMM used here is a DEA GLOBAL Advantage with the software PC-DMIS from Hexagon Metrology. The measurement accuracy is  $(1.5 + L/333) \mu\text{m}$  due to the last calibration. L is the distance between measurement points. The reference frame for the coordinate system for the CMM measurements was defined by the sides of the TS baseplate. The origin of the coordinate system is the lower left corner of the baseplate (see fig. 3.5), the same as for the IfoCAD simulations. The defining surfaces are the upper side of the baseplate and the two small sides next to the origin. The sides are not exactly orthogonal to each other, so the defining points are the intersection of the upper side and the side facing to the front in fig. 4.3 as the y-axis, the z-axis is in the direction of the normal vector for the upper side and the origin is the intersection of the y- axis, the z-axis and the surface on the right of the baseplate in fig. 4.3. Like this, the y-axis is along the edge of the baseplate and the x-axis is defined perpendicular to the y- and the z-axis. This coordinate systems was used for all alignment steps with the CMM.

For handling the TS baseplate a designated aluminum frame was used to protect both polished sides. The baseplate rests with its underside on three plastic cylinders covered with clean room tissues. The resting points were chosen to be not near the feet positions that were bonded later to the underside to avoid any possible damage of the bonding surface.

The baseplate is clamped in the aluminum frame with plastic screws and the frame has handles for easier handling, especially during the cleaning process.

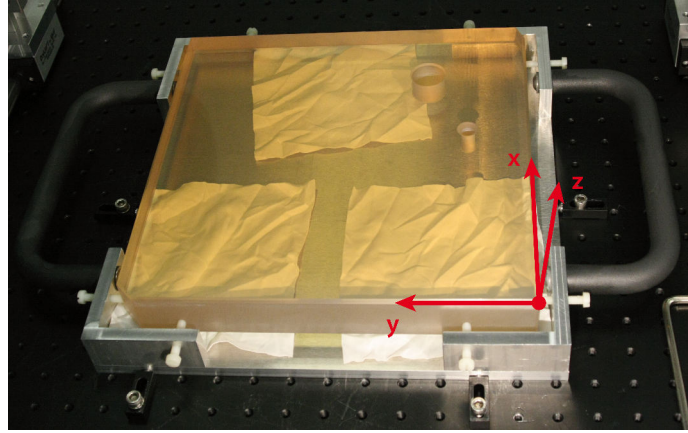


**Figure 4.3:** TS baseplate in the aluminum frame for easier handling. In red the coordinate system used for the CMM measurements is sketched. The baseplate is rotated by  $90^\circ$  in this photograph compared to the usual layout orientations. The origin of the coordinate system is usually in the bottom left corner.

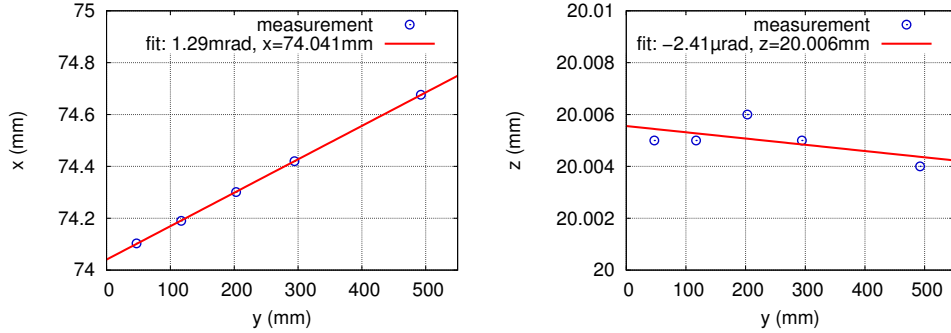
## RX Gauss FIOS

As the other FIOSs, the RX Gauss FIOS was manufactured at UGL [19]. The design is an evolution from the FIOS developed for LISA Pathfinder [43]. The beam is propagated only through fused silica from the fiber end to the collimating lens to improve the pointing stability and be less susceptible to damage due to contamination when operated with high output power [42].

The alignment in height and in vertical direction was also done in Glasgow using a post. For bonding it finally to the TS baseplate only the horizontal alignment had to be controlled. For this the method CABAM (CMM-assisted beam alignment and measurement, [56]) was used:

The position of the beam can be measured using a QPD and the tip of the CMM. The tip is made out of a ruby ball that is transparent and acts like a spherical lens. The QPD is first centered to the beam without the lens. Then the ruby ball is inserted a few millimeters in front of the QPD and positioned so that the focused beam is again centered on the QPD. Now the beam is transmitted through the center of the ruby ball and the CMM position is the position of the center of the beam. By measuring the beam position at at least two different distances the beam vector is given.

With this method the FIOS was aligned. For adjusting the FIOS it was held by an alignment tool with three adjustable ball bearings (see fig. 4.1b) to adjust the position and angle. Octane was used as a buffer fluid during alignment to prevent optical contacting or damage of the bonding surfaces. Using the CABAM method, the alignment is an iterative process. The beam position is measured, the FIOS realigned and the beam position is measured again.



(a) Measured beam position in the horizontal axis. Plotted are the measured points and a linear fit. The offset at the FIOS ( $y = 0$ ) is 0.41 mm and the angular offset 1.3 mrad of the design position.

(b) Measured beam position in the vertical axis. Plotted are the measured points and a linear fit. The offset at the FIOS ( $y = 0$ ) is less than  $6 \mu\text{m}$  and the angular offset less than  $3 \mu\text{rad}$  of the design position.

**Figure 4.4:** The beam orientation of the RX Gauss beam after bonding the FIOS measured with the CMM. The plots are showing the measurement points and a linear fit in the horizontal (x-y) and the vertical (z-y) axis. The design orientation is parallel to the y-axis and the z-plane with an offset of 74.5 mm in x from the origin and a beam height of 20 mm.

The beam position measured after the bonding is shown in fig. 4.4. The beam alignment in z, done by UGL with a post before bonding on the baseplate, is very good. The offset from the nominal beam height of 20 mm is  $6 \mu\text{m}$  and the angle with regard to the baseplate is less than  $3 \mu\text{rad}$ . This is close to the stated measurement accuracy with CABAM of  $3 \mu\text{m}$  [56].

For the alignment in horizontal direction the design position is  $x = 74.5 \text{ mm}$  and parallel to the y axis. The measured beam orientation has a 0.41 mm offset from the design position and an 1.3 mrad angular offset. This is well inside the requirement of 1 mm and 3.5 mrad offset. Should a more precise alignment be required, this should be possible with this method. Before bonding the beam position was aligned to better than  $50 \mu\text{m}$  and  $10 \mu\text{rad}$  with the FIOS on an octane film. The disadvantage of CABAM for bonding is that it is not fast enough to measure several points along the beam axis during the bonding procedure. For checking that the FIOS is sitting correctly in the ball bearings only one measurement point was taken by leaving the CMM tip at a target position measured before. This point was hit while bonding but with one point an offset in position and angle is still possible and probably the FIOS was not resting properly against the ball bearings during bonding.

For cleaning the baseplate before bonding the template had to be removed and the baseplate had to be moved to the sink in its aluminum frame. For bonding the baseplate had to be placed on the CMM table at the same position as before otherwise the CMM tip as a target would be in the wrong position



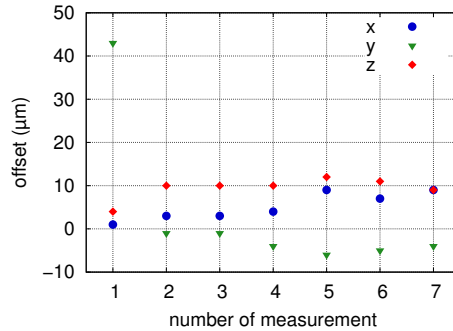


**Figure 4.5:** Measured position accuracy of the telescope simulator baseplate on the CMM table. Every measurement shows the offset of the origin of the coordinate system compared to the original position. In between the measurements the baseplate in its handling frame was removed from the CMM table and placed back into the ball bearings defining the position.

with regard to the baseplate. To test how well this is possible the baseplate was removed several times and the position of the baseplate reference frame was measured. The offsets of the origin of this reference frame are shown in fig. 4.5. In the first measurement the offset in y is significantly bigger probably because the baseplate was not pushed properly into the reference points (three clamps with ball bearings). This was tested later by trying to get a sheet of paper between aluminum frame and ball bearing. In all other measurements the deviation was less than  $15\ \mu\text{m}$ , good enough for bonding the FIOS.

In fig. 4.6 pictures of the curing process of the bond for the FIOS are shown. The picture 4.6a is showing the bond several minutes after placing the FIOS on the baseplate. The bond had started to cure already but several interference fringes are visible over the whole area (only visible from a certain angle so it was not possible to take a photo with the whole bonding area visible). This means the bonding surfaces are not close enough together, probably because of a dust particle or a scratch on one of the surfaces, e.g. from the lengthy alignment procedure. But during the curing the bond can bring the surfaces closer together because of the strength of the newly formed molecular bonds so the FIOS bond was observed for several days.

The second picture 4.6b was taken one day after bonding. It is clearly visible that the fringes nearly vanished and the bond formed over nearly the whole surface. Several days later on picture 4.6c there are no fringes visible anymore but several little "dry spots". They show a reflection from a certain angle and are visible as white spots on the photo. There the bond did not form. However, it formed over most of the surface which gives more than enough stability.

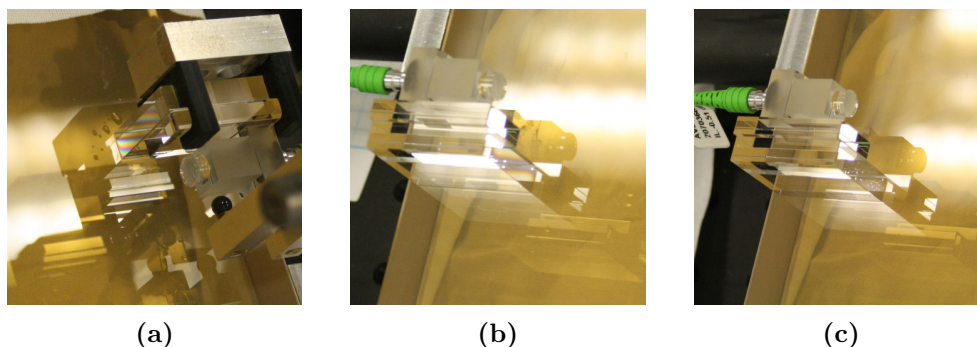


**Figure 4.6:** Curing of the bond of the RX Gauss FIOS. (a) A few minutes after bonding. Several fringes are visible over the whole bonding surface. (b) One day after bonding. The fringes nearly vanished and the bond did pull the surfaces together. (c) Several days after bonding. The fringes are gone and some dry spots are visible but they are only a small percentage of the bonding area.

### Template bonding of non-critical components

18 beam splitters and mirrors were bonded on the TS with a template. The components not bonded with a template are the ones for the alignment of the LO beam, which is critical because it is the alignments reference between the two benches, and the recombination beam splitter of the reference interferometer BS11.

Two different templates were used to bond the components. The templates were manufactured in the in house mechanical workshop out of brass.

**Design of the templates** The templates were designed with the CAD software Autodesk Inventor<sup>®</sup> using the component positions from the IfoCAD model. Each component sits in a pocket with three ball bearings as reference. The positions of the ball bearings were generated in IfoCAD and imported to Autodesk Inventor<sup>®</sup>. For double checking a CAD model of the TS with the template bonded components was generated and combined with the template model. The CAD models are shown in fig. 4.7.

For the bonding the TS baseplate with the template is placed on an inclined breadboard with the ball bearings on the down side of the pockets to push the components into the ball bearings by gravity. For parallel components close together (like the PBS directly behind the RX Gauss FIOS and the beam splitter combining the two RX beams) or component groups close together (like the beam splitter splitting the transmission output port of the reference interferometer and the surrounding mirrors) a scheme had to be found that allowed to fit the second template around the already bonded components. For that the baseplate was rotated by 90° between the two template bonding steps to get the inclination in another orientation.

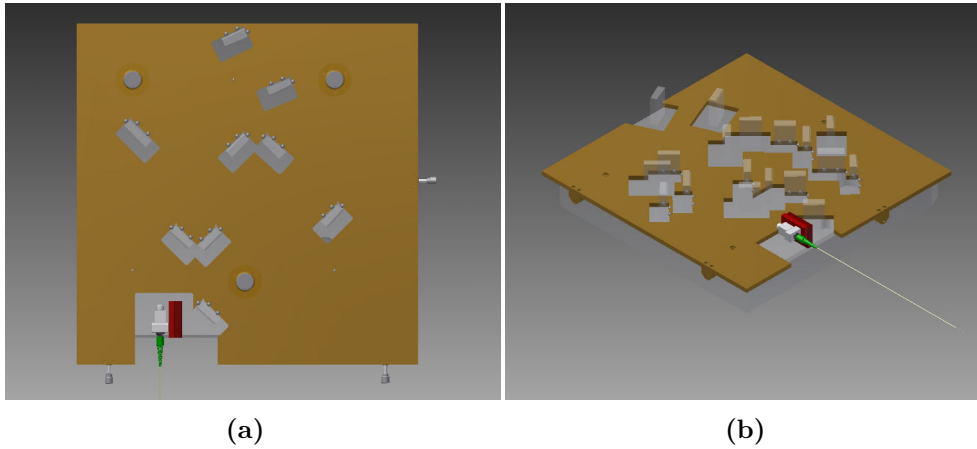


**Figure 4.7:** CAD models of the two templates for bonding the non-critical components of the telescope simulator. The positions for the components were extracted from the IfoCAD model and a CAD model of the baseplate with components was used to check the template design. (a) The first template has pockets with ball bearings for the first batch of components. (b) The second template has pockets with ball bearings for the second batch of components and cut outs for the already bonded components.

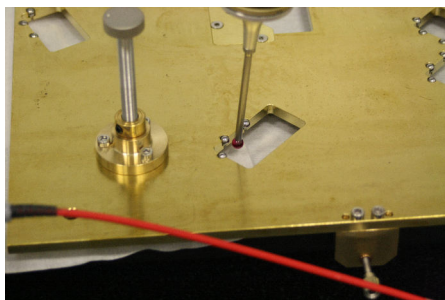
The templates were positioned on the TS baseplate by three fine thread adjustment screws pushing against the sides of the baseplate. Due to the inclination of the baseplate three adjustment screws are enough to fix the position of the template against the baseplate by gravity.

For a controlled lifting and removing of the template after bonding three long screws were integrated to push the template upwards until it could be removed safely by hand without touching any components (see fig. 4.8).

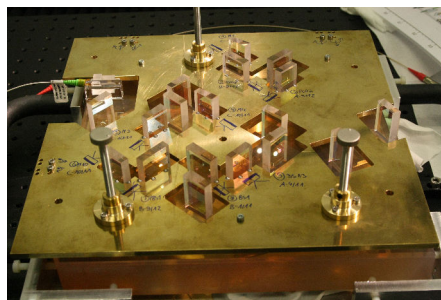
**Alignment of the templates** After manufacturing the positions of the ball bearings in the templates were measured with the CMM to determine the manufacturing tolerances and to optimize the template position. For this the function of the CMM measurement software PC-DMIS was used to fit a sphere to measurement points on a segment of a sphere because only a segment of the ball bearings is accessible in the template.

The measured tolerances for the ball bearing positions is  $10\ \mu\text{m}$  with a maximum deviation of  $24\ \mu\text{m}$ . The diameter tolerance of the ball bearings is  $10\ \mu\text{m}$  with one exception of more than  $50\ \mu\text{m}$ .

The measured positions and diameters of the ball bearings were used to find an optimized position of the template to minimize the alignment error because of tolerances. The offsets are not equally distributed around zero so an offset of the whole template can improve the overall alignment of the components. The optimization was done using the Microsoft Excel Solver Add-in as done before at UGL for templates.



(a) Measuring the position of the ball bearings in the template with the CMM.



(b) Bonding the second batch of components with the first batch already in place.

**Figure 4.8:** Photographs of template bonding.

To measure the orientation of the template on the telescope simulator baseplate the position of three ball bearings that are in different corners of the template was measured with the CMM. With the adjustment screws on the side the template was set in the optimized position on the baseplate.

**Bonding** Before each batch of components the baseplate was cleaned as well as the components to bond (see description in section 4.1). After placing the template back on the baseplate its position was checked by measuring the position of the three ball bearings again that were used for the alignment. In between the two templates the first batch of components were left to cure for several days.

After all the non-critical components were bonded their positions were measured using the CMM. These measurements were used to update the IfoCAD model to an as-built model. The offsets from the design value are  $100\ \mu\text{m}$  or less in  $x$  and  $y$  with a standard deviation of  $45\ \mu\text{m}$  in  $x$  and  $47\ \mu\text{m}$  in  $y$ . The deviation of the angle of the components is less than  $1\ \text{mrad}$  except for one component, the mirror M8 (see fig. 3.5) which is off by  $2.6\ \text{mrad}$ . This is not critical because it is only guiding the already interfered beams to the reference QPD. The reason for this big error is probably that the component was not properly sitting against the ball bearings while bonding. The standard deviation of the angle offsets is  $700\ \mu\text{rad}$  without the  $2.6\ \text{mrad}$  of M8. A complete list of the measured positions and angles can be found in appendix B.

**Waveplate** Gluing the  $\lambda/2$ -waveplate into its mount and onto the telescope simulator was the last step before shipping the telescope simulator to Glasgow. For aligning the orientation for optimal polarization rotation the waveplate was placed between two PBS. The first one ensured the right polarization of the beam and with the second, the transmission was optimized by rotating

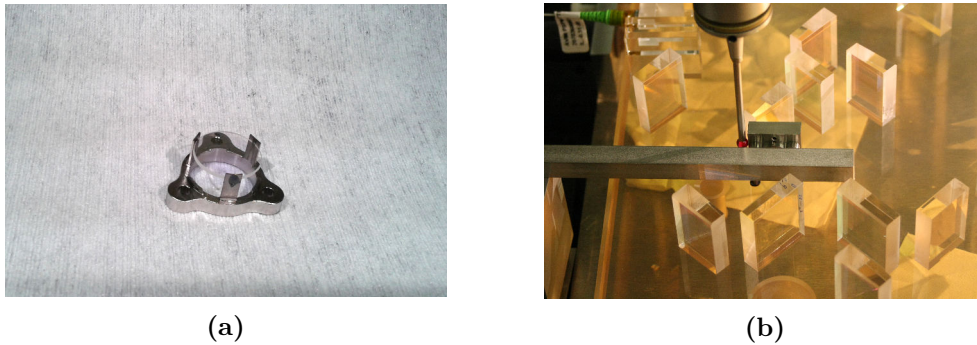


**Figure 4.9:** The  $\lambda/2$ -waveplate was clamped in the flexures without glue for aligning it in the right orientation. Then the glue was applied through little holes in the flexures (a). After aligning the rotation the waveplate mount was glued to the TS baseplate using simple positioning mechanics just to make sure the angle with regard to the beam is slightly offset to  $90^\circ$  and the waveplate is hit in the center (b).

the waveplate. In this position the waveplate was then glued to its mount (see fig. 4.9).

The position of the waveplate on the TS is not very critical so a simple positioning procedure was used. A metal bar for the angle and the tip of the CMM for the lateral position. The angle was chosen to be a little different from  $90^\circ$  with respect to the beam direction to avoid stray light in the same direction as the nominal beam. The measured angle after gluing for the mount of the waveplate is  $88^\circ$ .

## 4.5 Critical alignment steps

For some bonding and alignment steps the telescope simulator was shipped to UGL. There the LO FIOS was bonded and the beam aligned to the telescope simulator and optical bench baseplate with the following components. The achieved precision is  $10\ \mu\text{m}$  and  $20\ \mu\text{rad}$  with an uncertainty of  $5\ \mu\text{m}$  and  $20\ \mu\text{rad}$  ([57], [58]). The LO beam was aligned to a misplaced target and it has an offset of about  $200\ \mu\text{m}$ . When the telescope simulator is aligned to the optical bench the LO beam is aligned to the center of the TX beam on the optical bench. That means the beams are well aligned in the science interferometer but offset by  $200\ \mu\text{m}$  on the telescope simulator. But with the  $1\ \text{mm}$  radius beams the overlap is still more than enough and the offset is not critical.

Also the recombination beam splitter of the reference interferometer BS11 was bonded and the upper part of the feet for the tip-tilt mount. The bond for the feet needs to be strong because during the alignment some force might be applied to the bond.

The pinhole photodiode was also aligned to the LO beam in Glasgow. It needs to be centered to the beam better than the adjustment range of the mount of  $150\ \mu\text{m}$  with some margin. For achieving this the beam size was reduced with a lens and the power detected on the pinhole was maximized.

The methods and results for measuring the final alignment of the beams on the OB and the telescope simulator are reported in [58]). After these critical alignment steps the telescope simulator was shipped back to Hannover to continue the integration of the remaining parts.

## 4.6 Integration of metal parts and mounts

In this section the integration of the remaining metal parts and mounts, like photodiodes, beam dumps, the flat-top generator and the actuators is described. All parts were glued not directly on the baseplate but on pieces of Kapton<sup>®</sup> tape. The sticky tape was stuck flat on the baseplate and the components were glued with a two component glue (Hysol<sup>®</sup> EA 9361) on top of the tape. That allows to remove the components and keeps the setup flexible.

**Reference interferometer photodiodes** The reference pinhole SEPD was already integrated by UGL. Two more photodiodes were integrated for the reference interferometer. The reference QPD is a QP-22Q quadrant photodiode for aligning the RX beam. It was aligned to the center of the LO beam using the optical signal. It was mounted on a three degrees of freedom translation stage during the gluing process to ensure a good alignment.

The auxiliary SEPD is a big single element photodiode with an active area of 8 mm diameter. The alignment is not critical because the photodiode is bigger than the beam and it was aligned by eye to the center of the LO beam.

**Power monitor photodiodes** After each FIOS a PBS ensures the right polarization (s-pol) and a power monitor behind the PBS can be used for monitoring the actual laser power that enters the interferometers. The power monitor mount holds a beam splitter and two single element photodiodes. The beam splitter reflects one part of the beam upwards to save space (in comparison to a sideways orientation). The mount was designed and assembled by UGL and only had to be glued to the baseplate. With the big single element photodiode it was also sufficient to align them by eye to the LO beam and RX beam, respectively. To be sure the photodiode signals were monitored during gluing.

The beam splitters in the power monitors are not used in the polarization they are designed for because they are rotated by  $90^\circ$ . So their splitting ratio is not 50/50.

**Flat-top generator** For the alignment of the apodized aperture, a Shack-Hartmann sensor was needed. The aperture was aligned to the intensity center of the Gaussian beam and the flat phase profile was checked. There was no Shack-Hartmann sensor available at the AEI at that time, hence the alignment was done at Airbus DS. On the baseplate, the flat-top beam was aligned to the RX Gauss beam as good as possible to make switching between beams easier. In principle an alignment within the angular range of the actuators is sufficient. To overlap the two RX beams a beam splitter and two QPDs in different distances were installed next to the TS baseplate. Because the actuators were not yet integrated the RX beams were leaving the baseplate at the position of the first actuator. In the horizontal axis the beams could be overlapped quite well, in the vertical axis this was not possible because the mount for the flat-top generator does not have an adjustment mechanism in this axis. But the angle is small enough to have an DPS and DWS signal on the reference QPD for both beams with the same initial alignment by the actuators (see section 6.3 for the automatic alignment procedure).

**Actuators** Fig. 4.10 shows the actuator assembly. The piezo tip-tilt actuator Agilis AG-M100LV6 from Newport are screwed to the brass base with an aluminum adapter plate for the thermally compensated mount design. The brass base has three flexure feet to be glued on the telescope simulator baseplate. On the front, on the actuated part of the tip-tilt mount, a 1" mirror is attached. It is placed in front of the pivot point of the actuator to reduce longitudinal motion of the mirror. The adapter plate between actuator and mirror allows to glue the mirror in this position and its thickness is defined by the thermally compensating design.

After assembling the two actuator assemblies the actuators were set in the middle of their adjustment range and glued to the TS baseplate. The RX Gauss beam was overlapped with the LO beam during integration to make sure the correct alignment is well in the middle of the actuator adjustment range.

To determine the actuator position where the RX beam is aligned with the LO beam, the overlap of both beams was optimized after gluing by actuating the mirrors step by step with the dedicated controller and control software. The built-in position read out was then used to measure this position. Due to the varying step size of the actuators this position readout and commanding the actuators to this position is not very accurate. But it is accurate enough to get initial contrast between the RX and LO beam and start the automatic alignment procedure.

**Beam dumps** Beam dumps are placed at the open ports of the PBSs. The holes for dumping the beams have a spiral shape to minimize the reflections



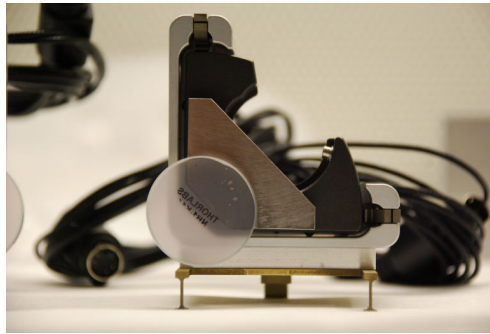


**Figure 4.10:** Actuator assembly. The mirror is glued via an adapter plate to the mirror mount to place it in the right height and in front of the actual rotation point of the actuator. The actuator is screwed to a brass baseplate with flexure feet. The whole assembly is designed to be thermally compensated to keep the mirror front face in a stable position.

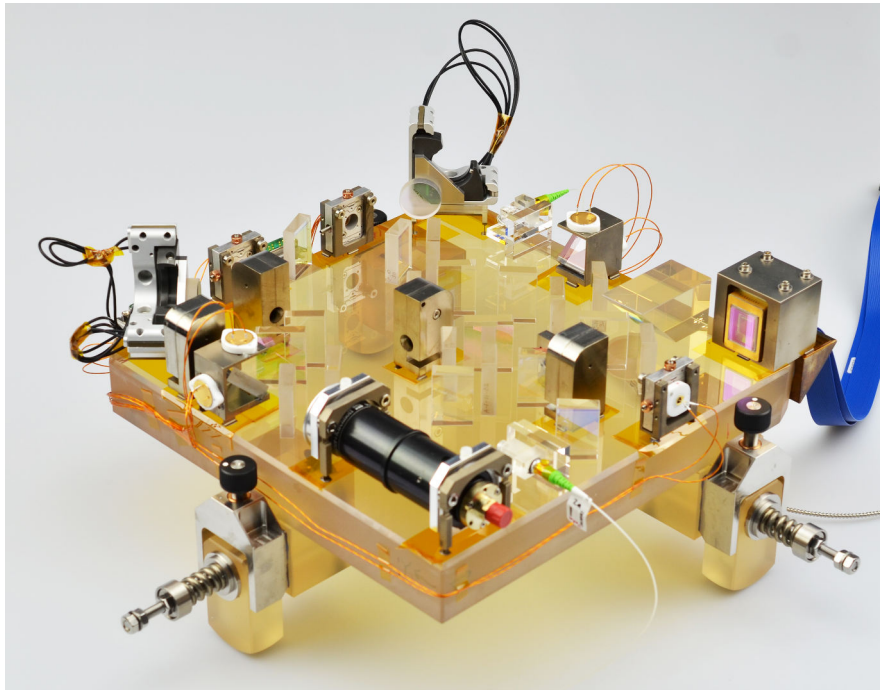


**Figure 4.11:** Photograph of completed telescope simulator

coming out of the beam dump. Their alignment is not critical but they were glued to the baseplate with flexure feet anyway to avoid stress.



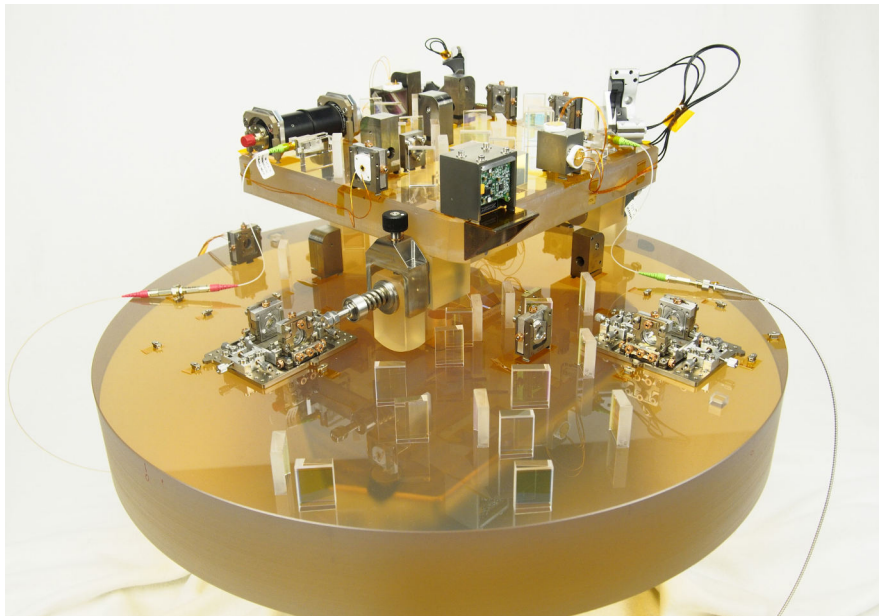


**Figure 4.12:** Photograph of completed optical bench and telescope simulator



# Electronics, laser preparation and vacuum tank

In this chapter an overview of the whole setup is given. This includes the electronics, the laser preparation with modulation bench, the automatic alignment and measurement procedure and the vacuum tank. The readout electronics and the phasemeter are described briefly. Most parts of this chapter have been recently published in the test report [45] and in [57].

An overview of the entire setup with telescope simulator, optical bench and laser preparation is shown in fig. 5.1. The laser preparation for operating the setup is done on a three-arm modulation bench, which is described in the next section 5.1. The telescope simulator and the optical bench are inside a vacuum chamber (see section 5.4) and the photodiode signals are recorded by a phase meter. A PC controls the alignment and measurement procedure and saves the data (section 5.3).

## 5.1 Modulation bench

The modulation bench provides three laser beams with different frequencies to allow a simultaneous measurement of all phase differences between the three beams (LO, RX and TX). A schematic and a picture of the modulation bench are shown in Fig. 5.2.

The laser is an NPRO 1064 nm laser, frequency stabilized to an iodine reference (Prometheus from Coherent), with an output power of about 700 mW. The beam is divided into three parts to generate the three different frequencies for OB and TS. The frequency is shifted by AOMs, the used frequencies and resulting heterodyne frequencies are listed in Tab. 5.1a and Tab. 5.1b. The different heterodyne signals are called A, B and C in the following. They are chosen to be in the range of a few kHz and not to have a harmonic relation.

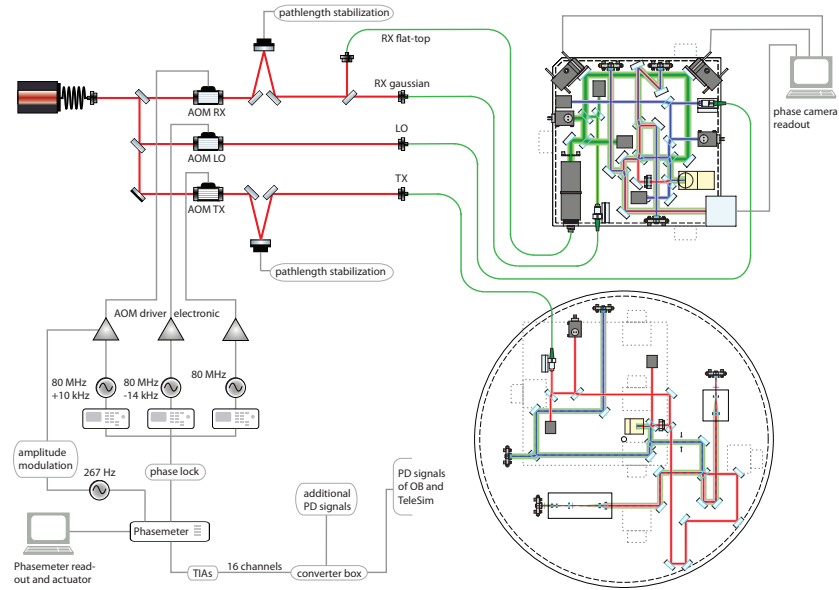


**Figure 5.1:** Schematic of the laser preparation and electronic setup for the heterodyne frequency generation and the phase readout.

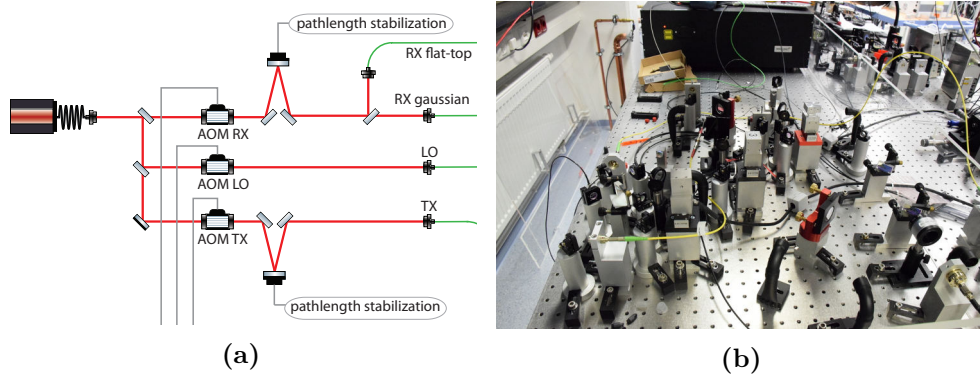


**Figure 5.2:** For the laser preparation one frequency stabilized laser is split into three beams which are frequency shifted on a three-arm modulation bench using AOMs. A schematic overview (a) and a picture (b) of the modulation bench are shown.

**Table 5.1:** AOM and heterodyne frequencies

(a) AOM driving frequencies		(b) Heterodyne frequencies		
beam	frequency [MHz]	phase	beams	frequency [kHz]
LO	79.9853515625	A	TX-RX	9.765625
TX	80.0	B	TX-LO	14.6484375
RX	80.009765625	C	RX-LO	24.4140625

The three beams are delivered to the setup by optical fibers and the RX beam is split again and coupled into two different fibers to allow an easy switching between the RX Gauss and RX flat-top beam. One of the two is always blocked in front of the fiber coupler on the modulation bench.

Mirrors mounted on linear piezo actuators are included in the TX and RX beam paths after the AOMs. They are used for an optical difference path-length stabilization (OPD) implemented in the phase meter ([59]). The phase difference between LO-TX and LO-RX is stabilized on the pinhole reference SEPD on the telescope simulator by actuating the pathlength with the piezo mounted mirrors. It was chosen to use the piezo mirrors in a small angle instead of using a PBS and a waveplate to avoid any additional spurious polarization effects. An earlier version of the modulation bench was built and characterized by Max Zwetz ([60]).

In Fig. 5.3 a schematic overview of the electronics for the modulation bench is shown. The heterodyne frequencies are generated with frequency generators which are locked to an external frequency reference provided by the phase meter. The signals from the frequency generators are amplified in the AOM driver electronics, which also provides an output power stabilization and an amplitude modulation input. This amplitude modulation input is used to modulate the RX beam with 267 Hz provided by the phase meter. In the phase meter the photodiode signals are demodulated with this frequency and used to read out the position of the RX beam on the reference QPD independent of the other beams.

## 5.2 Signal readout

The signal readout and overall organization is performed with a single-bin discrete Fourier transform phasemeter [27] and a "readout and control" software. The phasemeter has 16 input channels for reading out the photo diode signals. All photodiodes are connected via 25 D-Sub feedthroughs in the vacuum tank and divided into signals going to the phasemeter and additional signals in a converter box. The signals going to the phasemeter are amplified with transimpedance amplifiers (TIAs) and connected to the analog-to-digital

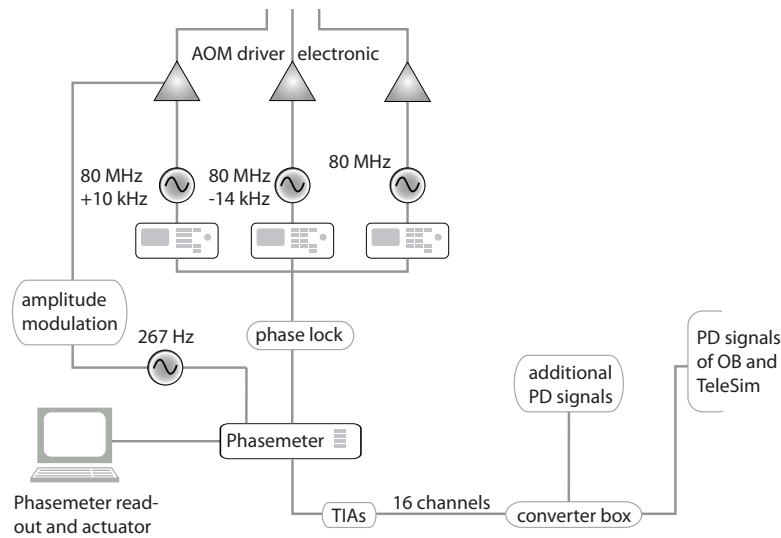


**Figure 5.3:** Schematic overview of the electronics for the modulation bench. The AOM driver frequencies are generated by frequency generators locked to the phasemeter. The RX beam is amplitude modulated using the modulation input of the AOM driver electronic.

converter of the phase meter. More details and circuit layouts of the converter box and the TIAs can be found in [34].

Not all photo diodes can be read out simultaneously with the 16 channels. The CQP and the temporary four-hole aperture QPD are connected to separate TIAs and the signals are displayed with an oscilloscope for the alignment. However, the converter box can be used to feed different signals to the phasemeter temporarily like the CQP diodes or the power monitor diodes for debugging.

### 5.3 Control software

The actuation of the tilt mirrors on the TS is controlled via a PC and piezo driven mirror mounts (Newport Agilis<sup>TM</sup> AG-M100LV6). An automated measurement procedure performing a tilt measurement with all the necessary actuation and alignment of the tilt mirrors is implemented in a measurement program. The 16 channels of the phase meter are recorded with the DC value, phase and amplitude of all three heterodyne signals and the amplitude modulated signal. In addition error signals and actuation signals of the two OPD locks are recorded. For the TTL measurement averaged values for every step are recorded as well as a log file for checking alignment and measurement steps. A screen shot of the terminal output of the measurement program is shown in Fig. 5.4.

```

lob_khz_pm      Freq A: 9765.625000 |   Freq B: 14648.437500 |   Freq C: 24414.062500 |
Package counter: 218 |Missing packages: 1

Signals
DC      : +0.520      +0.102      +0.351      +0.322      +0.320      +0.370      +0.253      +0.974
A:Amp   : +0.000360  +0.000299  +0.000130  +0.000126  +0.000110  +0.000235  +0.000500  +0.000004
A:Phase : -16.437634  -1.432242  -0.555411  -12.858567  -6.832785  +5.360979  -3.549856  -2.441380
B:Amp   : +0.241019  +0.056411  +0.175364  +0.118672  +0.112452  +0.168390  +0.001877  +0.000014
B:Phase : -0.851137  -4.464284  -4.078254  -4.160079  -3.904684  -3.368930  +1.801105  -3.996865
C:Amp   : +0.000035  +0.000026  +0.000034  +0.000036  +0.000037  +0.000037  +0.000483  +0.000001
C:Phase : +11.773949  -21.919137  -1.136836  -1.250497  -1.151608  +5.135440  +2.702498  -15.517671
AM:Amp  : -0.000081  +0.000022  +0.000050  +0.000032  +0.000030  +0.000047  +0.000001  -0.000000

Signals
DC      : +0.228      +0.216      +0.211      +0.218      +0.194      +0.215      +0.200      +0.211
A:Amp   : +0.000160  +0.000206  +0.000216  +0.000183  +0.000184  +0.000063  +0.000010  +0.000683
A:Phase : -3.048602  +0.351219  +0.797881  -4.450737  -1.529202  -1.701803  +1.210180  -1.737835
B:Amp   : +0.001352  +0.000152  +0.000339  +0.001049  +0.000551  +0.000750  +0.000644  +0.001801
B:Phase : +1.903783  -0.337742  -1.678720  -3.189383  +1.425021  +2.136903  -3.999013  +0.819992
C:Amp   : +0.000010  +0.000001  +0.000003  +0.000012  +0.000004  +0.000002  +0.000003  +0.000052
C:Phase : -4.016811  +23.418885  -4.311483  -4.315987  -2.885089  +23.399485  +0.494460  -3.785195
AM:Amp  : -0.000001  -0.000003  -0.000000  -0.000000  -0.000002  -0.000002  -0.000001  +0.000005

OPD1:      ERR      : -0.000002
OPD2:      ERR      : -0.000296
ACT      : +0.000      ACT      : -0.032
CH/FREQ: 02 | c      CH/FREQ: 02 | a

---- Ref QPD ----      ---- Sci QPD 1 ----      ---- Sci QPD 2 ----
DPS 1:  -0.000006      DPS 1:  +0.017876      DPS 1:  -0.002422
DPS 2:  +0.000019      DPS 2:  +0.021026      DPS 2:  -0.012469
DWS 1:  -0.276653
DWS 2:  +0.416192

```

**Figure 5.4:** Screen shot of the user interface of the measurement program. For each phasemeter channel the DC value, phase and amplitude for all three heterodyne frequencies and the amplitude modulated (AM) signal is displayed. In addition error signals and actuator signals for the OPD locks and DPS and DWS signals are displayed.

The program has a watch-mode where it is run without the tilt actuation for alignments and debugging. For this mode it displays the DPS signals of the science QPDs.

The complete measurement procedure is described in detail in [45]. In summary the procedure executes the following steps:

- Initial alignment by commanding the actuators to absolute positions. The position is chosen, so that there is some contrast on the ref QPD.
- Maximizing the heterodyne amplitude on the ref QPD.
- Minimizing the DWS signal on the ref QPD.
- Starting the measurement steps. The averaging for every angle and the number of cycles can be varied.

The step size of the actuators is varying ([48]) and cannot be used for positioning. For every angle step the angle is set by the first actuator and the second actuator is used to center the RX beam on the ref QPD again using the DPS signal. This leads to slightly varying angle step sizes and instead of the set angles the DWS signal is used to determine the actual angle.

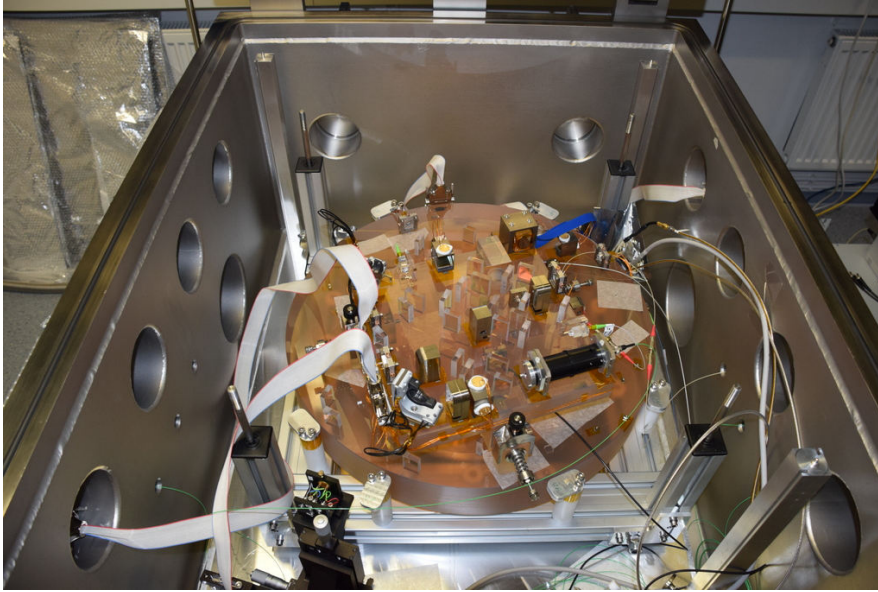


**Figure 5.5:** Picture of OB and TS in the vacuum tank with open lid. The modulation bench is on an optical table next to the vacuum tank.

## 5.4 Vacuum tank

The OB and the TS are inside a vacuum tank (see Fig. 5.5). The modulation bench and the electronics are outside the vacuum tank connected via electrical and fiber feedthroughs with the setup inside. The experiments for this projects were all performed at atmospheric pressure with a vented vacuum tank. Vacuum is not needed to measure coupling factors and the frequent alignment changes would make it very time consuming to measure in vacuum. However, the vacuum tank is providing a good shielding from air flows, fast temperature changes and electric cross coupling from the surrounding lab. The vacuum tank was closed for all measurements. For some measurements (see section 6.8 the temperature inside the vacuum tank was recorded using an FPGA thermometer with PT10k sensors (for more information on the temperature readout system see section 10.1).

## 5.5 Representivity of the operation parameters

As stated in [34] the parameters for operating the setup are chosen to be efficient and not fully representative where this is not necessary.

- kHz heterodyne frequencies are used instead of MHz heterodyne frequencies and the laser light power levels are mW instead of pW. This is not influencing the effects under investigation and would add extra complexity.



- Operation in air does not allow picometer stability. The measurement of coupling factors does not require picometer stability.
- To have a representative testbed it was constructed to have the ability to measure a few pm/ $\sqrt{\text{Hz}}$  with pW light levels and MHz heterodyne frequencies (with modified FEE). This also offers the possibility of more representative further investigations.

The key parameters are fully representative for this tilt-to-length coupling investigation:

- Operation with an RX beam with a flat phase and intensity profile, or two Gaussian beams with different beam parameters, is possible.
- The RX beam is tilting around the center of the RX aperture, which will be the position of the pupil plane of the telescope.
- By placing the reference QPD in an optical equivalent position of the RX aperture, only the tilt-to-length coupling on the optical bench is measured.
- The distance of the science interferometer photodiodes to the point of rotation, as well as the magnification factor, comparable to expected layout of the LISA optical bench.
- All-Zerodur design with components intended for an elegant breadboard for a full LISA optical bench. The telescope simulator is only mounted by gravity without any additional interfaces or mounts on the optical bench.



## Part II

# Experimental investigation of tilt-to-pathlength coupling in LISA

*The results presented in this part were mainly produced within the LISA optical bench development project. These results have been published already in the project test report [45] and in [57] and most figures and some text are similar in these documents. In some parts the same wording might have been used. The author performed most of the shown measurements, the analysis and interpretation of the results was often a combined effort, and the simulations were mostly done by Sönke Schuster.*

# Alignment and calibration

In the following chapter various calibration measurements are reported which are necessary for the TTL coupling investigations. First the differential power sensing signal (DPS) and the differential wavefront sensing (DWS) alignment signals are calibrated for the different beams and photodiodes and second the alignment and calibration of the telescope simulator are shown. The calibration of the telescope simulator is necessary to ensure that only the TTL coupling contribution of the optical bench is measured. The reference pinhole photodiode on the telescope simulator was aligned to the temporary pinhole photodiode in the RX aperture. To ensure the centering of both pinholes to the beam a flipping procedure is used where the telescope simulator baseplate is rotated by  $180^\circ$  to flip the sign of the TTL coupling contribution of the telescope simulator.

The results of the calibration of the telescope simulator are different for the RX Gauss and the RX flat-top beam. The measurements with the RX Gauss show good alignment of the pinhole photo diodes and a residual coupling well inside the requirements. The RX flat-top shows a larger residual coupling, the source of which is currently unknown. Different possibilities were investigated like ghost beams and a micro structure on the phase profile. The micro structure is currently the most likely candidate for the residual coupling and further investigations are discussed.

At the end of this chapter a tilt-to-length coupling measurement without imaging systems is shown to demonstrate the readiness for operation of the complete setup. The measured TTL coupling also shows that imaging systems are necessary to meet the LISA requirement.

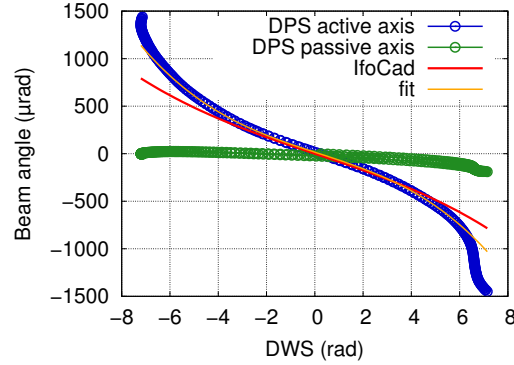


**Figure 6.1:** Calibration of the DWS signals for Gaussian RX beam; beam angles calculated from calibrated DPS signals are plotted versus the DWS signals for the active (actuated) axis and the passive axis. A third order polynomial is fitted to the measured data. The IfoCad simulation fits well to the measured data.

## 6.1 Photodiode signal calibration

The DPS and the DWS signals were calibrated. The calibration depends on the beam parameters and the photo diodes and if possible the results were verified with simulations. The DPS signals are used later for aligning the RX beam and investigating beam walk. The DWS signal of the reference QPD is used for measuring the actual angle of the RX beam. The information from the tip-tilt actuators cannot be used because the step size varies too much.

### Calibration for the Gaussian beams

For the LO beam and the RX Gauss beam with a Gaussian beam profile the DPS signals can be calculated analytically with the measured beam sizes (see 2.2). The beam radii are  $1109\ \mu\text{m}$  for the LO beam and  $1355\ \mu\text{m}$  for the RX Gauss beam measured with a WinCamD at the distance of the RX aperture from the FIOS. With the beam position on two QPDs and the known distance between them the beam angle can be calculated. Here the reference QPD on the telescope simulator and the QPD2 from the calibrated quadrant photodiode pair (CQP) on the optical bench are used for measuring the angle of the RX Gauss beam. The beam angle is then used to calibrate the DWS signal (see fig. 6.1).

The DWS signal can also be calculated with IfoCAD for a Gaussian beam. The third order polynomial fit from IfoCAD provided the following fit parameters (rounded):  $y = -0.48x^3 - 0.01x^2 - 85.05x + 0.05$ . The result is plotted in fig. 6.1 and shows a good agreement with the measured calibration. The DWS signal below and above approximately  $\pm 6$  rad (optical phase) is not valid because the contrast is too low.



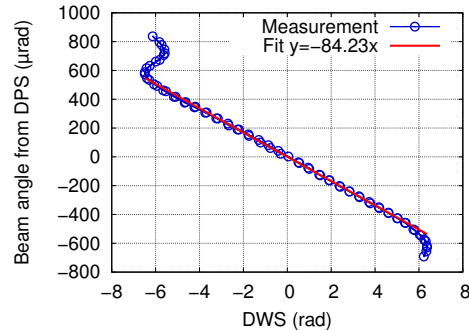


**Figure 6.3:** Beam angle vs. DWS signal for the RX flat-top beam. The beam angle is calculated from the calibrated DPS signal.

this fit. Again the DWS signals below and above approximately  $\pm 6$  rad are not valid.

The coefficients measured here are used in the following to calculate the beam angle from the DWS signal in the TTL coupling measurements and thus provide the x-axis for most plots to follow.

## 6.2 Telescope simulator alignment on optical bench

The telescope simulator needs to be aligned to the optical bench. Therefore the telescope simulator position and orientation can be adjusted in all degrees of freedom using the mounting feet described in [34]. The target for the alignment are the two CQP diodes on the optical bench which are aligned to the nominal beam position of the LO. With these two photo diodes the offset and the angle of the Telescope simulator is measured by reading out the position of the LO on the optical bench. For the x, y and roll degrees of freedom the telescope simulator is shifted using the technique of micro hammering. Here, the telescope simulator is shifted by tapping against it. For roll, yaw, and z degrees of freedom the height of the individual feet is adjusted. The alignment steps are described in more detail in [61]. With this method the beam can be centered on the CQP diodes with a 1-2 $\mu$ m accuracy. This is sufficiently accurate because other components like the pinhole positions, the science interferometer QPDs and others influencing the TTL coupling performance cannot be aligned with a higher accuracy. The alignment of the telescope simulator is limited by beam jitter due to air movement.



### 6.3 Tilt actuation of the RX beam

The RX beam is tilted around the pivot in the RX aperture with the two piezo actuators on the Telescope Simulator.

For the measurement steps and the alignment an automatic procedure was implemented in the readout program (see section 5.3). The main steps for a TTL measurement are:

- Alignment of the RX beam to zero DPS and DWS
- The first actuator is commanded to do one angle step.
- The RX beam is aligned to zero DPS with the second actuator. The beam is now tilted and centered on the reference QPD, which means it is rotated around the RX aperture.
- Measurement. The measured phase is averaged over several data points.
- First actuator is commanded to do the next angle step.
- and so on...

Before starting the automatic procedure, the alignment between the beams has to be sufficiently good to have some heterodyne amplitude for the optimization. Setting the actuators to a default position is enough to have a starting point.

In the first step the RX beam is aligned to the zero position by minimizing the DPS and the DWS signal on the reference QPD. Then the actuator 1 (the first in the beam path from the FIOS) is commanded to do the first angle step. By aligning the RX beam with the actuator 2 back to the center of the reference QPD, the RX beam now is tilted around the center of the photodiode, which means it is tilted around the center of the RX aperture. In this position a measurement point is taken by averaging the phase for the measurement time. After completing the measurement point the first actuator is commanded to do the next angle step and the procedure is repeated.

The resulting angle after an angle step is slightly different from the set angle but this is not critical because the actual angle can be measured with the DWS signal (see section 6.1). In the program the maximum angle in both directions and the number of steps can be specified.

Without loss of generality the actuation axis is vertical to the baseplate plane.

In the combined setup of optical bench and telescope simulator the TTL coupling has a contribution from the OB but also from the Telescope Simulator. To characterise only the optical bench contribution, the contribution of the Telescope Simulator has to be removed by a calibration (also called phase center characterization). This is done in two steps described in [61]. In

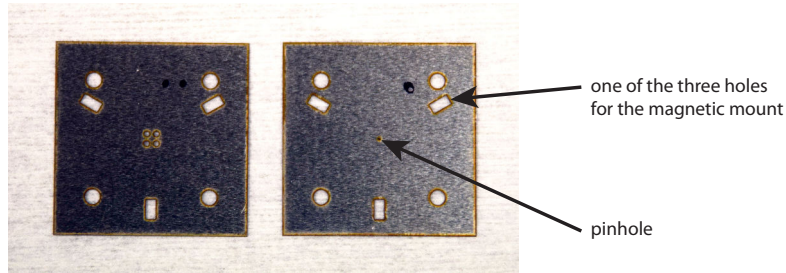


**Figure 6.4:** Photograph of a four-hole (left) and a pinhole (right) aperture. The apertures are clipped into the RX aperture mount by three spherical magnets that fit into the three rectangular holes. Behind the four-hole aperture a QPD is fixed so that each hole is in front of a different quadrant. Like this a DPS signal is measured which is only dependent on the exact position of the four holes and not on the position of the QPD. The apertures are machined to have the four holes and the single pinhole exactly in the center of the three mounting holes.

the first step the reference pinhole photodiode on the Telescope Simulator is aligned to a temporary pinhole photodiode in the RX aperture, so that they are optically equivalent copies of each other. In the second step the Telescope Simulator is flipped by  $180^\circ$  to flip the sign of the TTL coupling contribution of the Telescope Simulator.

## 6.4 Pinhole alignment

The reference pinhole SEPD on the telescope simulator should be optically equivalent to a pinhole placed in the center of the RX aperture. The latter is realized by actually placing a temporary pinhole SEPD in the center of the RX aperture that will be removed again after the calibration. The reference pinhole SEPD on the telescope simulator is aligned to this temporary pinhole so that it is equivalent. In fig. 6.4 a photograph of a pinhole aperture and a four-hole aperture is shown. The four-hole aperture is an alignment tool.

Alignment procedure:

- Align the telescope simulator to the optical bench.
- Place a temporary QPD with a four-hole aperture in the RX aperture and align it to the LO beam using the DPS signals.
- Exchange the four-hole aperture by the pinhole aperture with a SEPD. The pinhole is in the center of the four hole aperture.

The temporary pinhole SEPD is mounted in the RX aperture with a magnetic kinematic mount and has to be aligned to the LO beam after aligning the telescope simulator with respect to the OB. The pinhole SEPD is the pinhole

aperture shown in fig. 6.4 glued in front of a single element photo diode, so that only the light transmitted through the pinhole is hitting the photodiode. The pinhole itself cannot be used for aligning it to the center of the LO beam because the accuracy that can be achieved using a Gaussian intensity profile much bigger than the pinhole is not accurate enough (see [34]). Instead a four-hole aperture in front of a QPD is used with one hole in front of each segment. This allows to use the position of the aperture as the alignment reference instead of the position of the QPD. The four-hole aperture is aligned to the mount with the same magnetic mount but it is not trivial to align the QPD to a few microns and thus the aperture was used as the reference. After aligning the QPD is then exchanged by the pinhole photodiode. The different apertures are accurately machined to ensure the center of the apertures is in the center of the rectangular holes defining their position on the magnetic mount. They are interchangeable and placed with micron accuracy on the mount with the magnetic kinematic mount.

The critical part of this procedure is to be able to place the apertures repeatedly on the RX aperture mount within a few microns. The manufacturing tolerances of the apertures and the repeatability of their placement were checked before (see [45]).

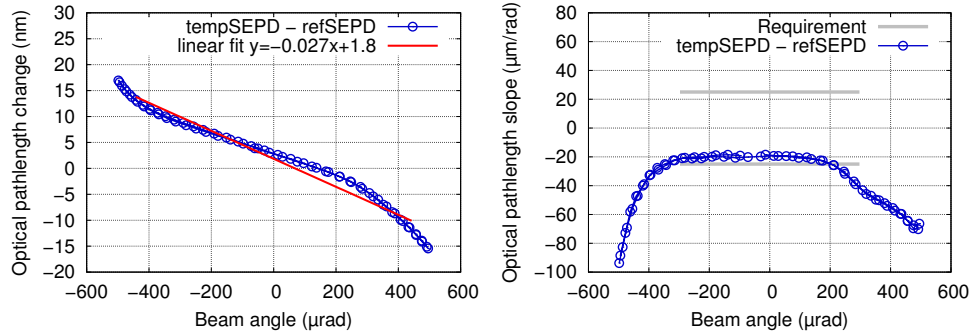
## 6.5 Reference pinhole on the Telescope Simulator

The reference pinhole has to be aligned to be equivalent to the pinhole in the RX aperture. The longitudinal alignment is less critical, a few mm is sufficient. The RX aperture mount and the mount of the reference pinhole were positioned carefully and the distance of the Telescope Simulator to the optical bench was adjusted to the default height with the tip-tilt mount.

The lateral alignment has to be accurate to micrometers and is done by measuring the TTL coupling difference of the two pinhole photo diodes. The coupling should be the same on both pinhole diodes if they are copies of each other. A lateral misalignment leads to a linear coupling.

The following alignment procedure was used:

- Perform a TTL measurement and look at the difference of the two pinhole photodiodes.
- If there is a difference move the reference photodiode laterally.
- Perform another TTL measurement.
- Repeat until the difference between the two pinhole photodiodes is minimized.



(a) Pathlength change vs. beam angle. (b) Slope of pathlength change vs. beam angle.

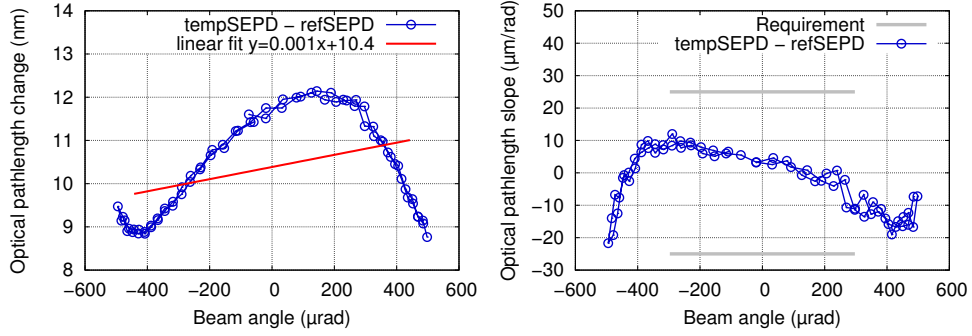
**Figure 6.5:** Difference of the pathlength signal between the reference pinhole photodiode and the temporary pinhole photodiode in the RX aperture with the RX Gauss beam. The reference pinhole photodiode is not aligned which leads to the linear pathlength change.

An intermediate step in this procedure is shown in Fig. 6.5. Fig. 6.5a shows the pathlength difference between temporary photodiode and reference photodiode on the telescope simulator versus beam angle. Figure 6.5b shows the corresponding slope of the pathlength change. The reference pinhole photodiode is laterally not aligned to the temporary pinhole photodiode, which leads to a linear coupling.

Figure 6.6 shows the resulting situation after completion of the alignment procedure for the RX Gauss beam. The linear coupling could be reduced to be well below the requirement of  $25 \mu\text{m}/\text{rad}$  by aligning the pinhole photodiode laterally. The linear fit in the pathlength change shows the the residual linear part of the coupling and is a measure of how well the photodiode is aligned. The quadratic coupling that is still visible after the alignment cannot be reduced by a lateral alignment of the pinhole photodiode but it is small enough to fulfill the requirements.

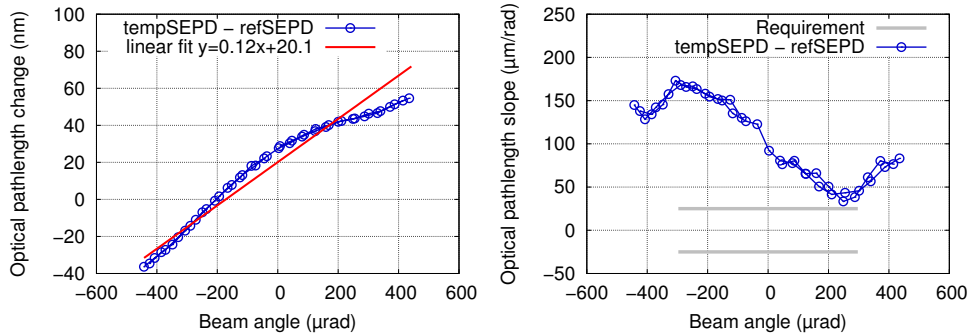
Figure 6.7a shows the pathlength difference between temporary pinhole photodiode and reference photodiode for the RX flat-top beam at an intermediate step during alignment. The reference pinhole photodiode is laterally not aligned to to temporary pinhole diode. This leads to the linear coupling shown in Fig. 6.7b.

Figure 6.8 shows the resulting situation after completion of the alignment procedure for the RX flat-top beam. There the linear part of the coupling could also be removed by a lateral alignment of the pinhole photodiode. The linear fit shows again the linear part of the coupling which is a measure of how well the photodiode is aligned laterally. However, the quadratic part of the coupling is larger than for the Gaussian beam and the requirement could not be fulfilled. The quadratic contribution cannot be removed with the



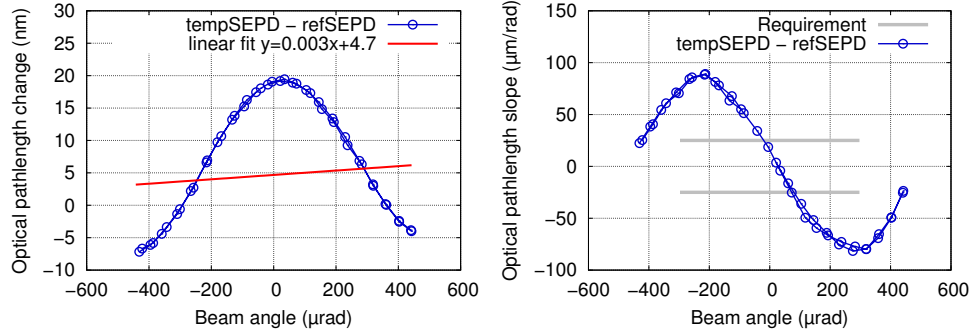
(a) Pathlength change vs. beam angle. (b) Slope of pathlength change vs. beam angle.

**Figure 6.6:** Difference of the pathlength signal between the reference pinhole photodiode and the temporary pinhole photo diode in the RX aperture with the RX Gauss beam. The reference pinhole photodiode is aligned to minimize the pathlength change.



(a) Pathlength change vs. beam angle. (b) Slope of pathlength change vs. beam angle.

**Figure 6.7:** Difference of the pathlength signal between the reference pinhole photodiode and the temporary pinhole photodiode in the RX aperture with the RX flat-top beam. The reference pinhole photodiode is not aligned which leads to the linear pathlength change.



(a) Pathlength change vs. beam angle. (b) Slope of pathlength change vs. beam angle.

**Figure 6.8:** Difference of the pathlength signal between the reference pinhole photodiode and the temporary pinhole SEPD in the RX aperture with the RX flat-top beam. The reference pinhole SEPD is aligned to minimize the pathlength change.

foreseen procedure of lateral alignment of the pinhole photodiode. The cause of the high quadratic term in the coupling is not known for sure. Further investigations and a discussion can be found in section 6.7. However the requirement for the TTL coupling in the science interferometer was met in the measurements with imaging systems. The correct position of the reference pinhole was ensured with the RX Gaussian beam to validate the calibration as shown in the next section. That means the measurement between pinholes with the flat-top beam shown here does not indicate an incorrect alignment of the reference pinhole and it is not likely to have an influence on the imaging system performance measurements.

## 6.6 Alignment test using the flipping procedure

The reference pinhole photodiode was aligned to the temporary pinhole photodiode in the RX aperture by minimizing the differential coupling between these two photodiodes. This means they see the same coupling and are hence in equivalent positions with regard to the beams. The temporary pinhole photodiode was placed in the center of the LO beam using the four-hole aperture (see section 3.2 and [45] for details), which is also the point of rotation, and both pinhole photo diode should be centered on the point of rotation. This was tested by flipping the whole telescope simulator baseplate by  $180^\circ$ . By rotating the telescope simulator, the beam on the temporary pinhole photodiode is rotated by  $180^\circ$ . If the two pinholes both had an offset from the point of rotation before flipping, the sign of the offset changes for the temporary pinhole by the flipping.

For the lifting and rotation of the telescope simulator an additional support structure and a crane were used. Although the telescope simulator is not as

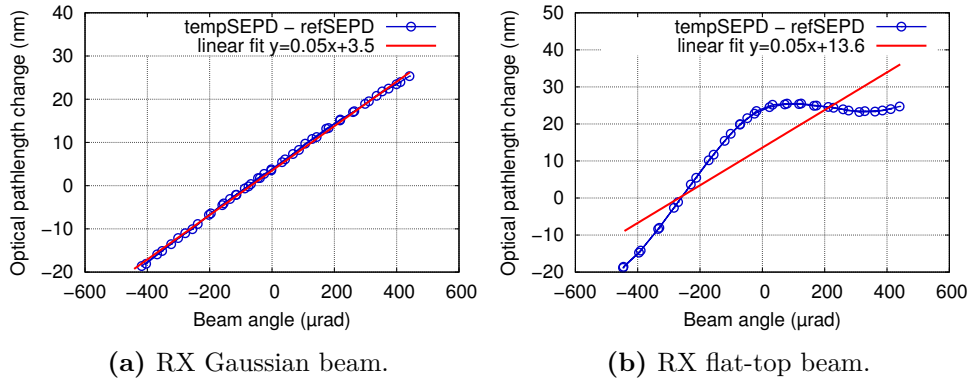


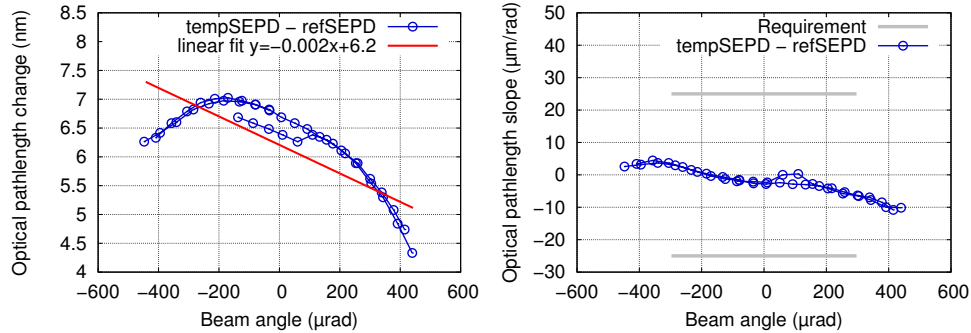
**Figure 6.9:** Difference of the pathlength signal between the reference pinhole photodiode and the temporary pinhole photodiode in the RX aperture after the flipping, before adjusting the temp photodiode.

big and heavy as the optical bench it is not easily handled in the vacuum tank because a lot of care is needed to not damage any of the components on the optical bench or the telescope simulator. After the rotation the LO beam and the CQP are again used for the fine alignment to ensure that the rotation axis is the LO beam.

The results for the flipping procedure are shown in fig. 6.9 for both, Gaussian and flat-top RX beam. Here again the difference between the reference pinhole photodiode and the temporary pinhole photodiode in the RX aperture is shown. That means the measured TTL coupling is a result of an offset of the pinholes and the pinholes were not centered on the point of rotation before flipping. To align both pinholes to the center of the rotation axis (beam axis of LO and TX), they are shifted by half of the total offset after the flipping towards the middle. The measured TTL coupling after the flipping was  $51 \mu\text{m}/\text{rad}$  for both RX beams (see fits in fig. 6.9a and fig. 6.9b). That means both pinholes have to be shifted by  $25 \mu\text{m}$  in opposite directions.

In fig. 6.10 the result after the realignment of the pinhole photodiodes is shown for the Gaussian RX. The procedure was successful and the remaining TTL coupling of the aligned telescope simulator and optical bench setup is well inside the requirement with the RX Gauss beam.

The TTL coupling with the RX flat-top beam does not meet the requirement, not even before flipping as shown in fig. 6.8. The cause of the additional quadratic coupling is not yet understood. However, it was shown with the RX Gauss beam that the telescope simulator and the reference pinhole photodiode are aligned. The RX Gauss and the RX flat-top are both aligned in the same way with regard to the LO beam, so the alignment of the telescope simulator and the reference pinhole is valid for both beams. The additional coupling with the flat-top beam is probably an effect of the quality of the flat intensity and wave front profile in combination with the very small pinholes and is not



(a) Pathlength change vs. beam angle. (b) Pathlength change slope vs. beam angle.

**Figure 6.10:** Difference of the pathlength signal between reference pinhole SEPD and temporary pinhole SEPD in the RX aperture with the RX Gauss after flipping, after adjusting the reference pinhole

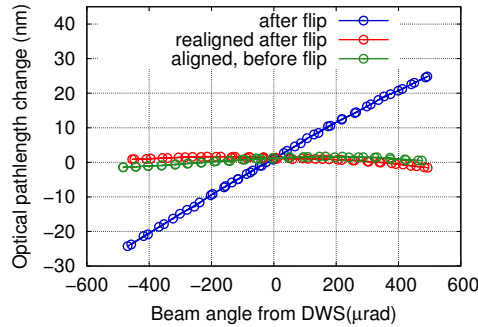


**Figure 6.11:** Difference of the pathlength signal between reference pinhole SEPD and temporary pinhole SEPD in the RX aperture with the RX Gaussian before and after flipping, as well as after realignment of the reference pinhole.

present in the TTL measurements with the science interferometer to test the performance of the imaging systems.

For comparison, the pathlength measurements before flipping, after flipping and after realignment of the reference pinhole are shown in fig. 6.11. Before flipping the difference of the two pinholes is small because they are in equivalent positions with regard to the beams but both with the same offset from the point of rotation. After flipping the sign of the offset changed for the temporary pinhole and the distance between the two pinholes is now twice the offset from the point of rotation, causing the linear coupling. After realigning both pinholes towards the point of rotation by half of their distance they are again in equivalent positions and on the center of rotation.



## 6.7 Investigation of the pinhole-pinhole measurement with the flat-top beam

In this section the investigation of the cause of the remaining higher order TTL coupling in the pinhole-pinhole calibration measurements with the RX flat-top beam, shown in fig. 6.8, is presented. This higher order coupling exceeding the requirement is only present in this measurement where the phase on the reference pinhole photodiode on the telescope simulator and the temporary pinhole photo diode in the RX aperture on the optical bench are compared. The same measurement with the RX Gauss beam showed that the two pinholes are both aligned to the rotation point of the RX beam and should in principle see exactly the same phase signal, because they are placed in optically equivalent positions. This is true well within the requirement for the RX Gauss beam which shows that the measurement principle is working. The additional coupling with the flat-top beam has to be caused by some effect that is different for the two pinhole diodes so that they are not seeing the same phase signal anymore.

Several hypotheses were investigated and are discussed in the following.

### Back reflection from pinhole aperture

One difference between the two pinhole diodes is the material of the apertures. The metal foil of the temporary pinhole is more polished and has therefore a higher reflectivity. The whole flat-top beam and the LO beam are hitting the front surface of the aperture (the 150  $\mu\text{m}$  pinhole is much smaller than the beams) and some fraction is reflected back into the interferometer.

The back reflection was first reduced by inserting a non-reflective black cardboard pinhole – slightly bigger than the metal pinhole – in front of the temporary pinhole. Fig. 6.13a shows that this did not influence the remaining TTL coupling.

Then a quarter waveplate was inserted instead in front of the temp pinhole. See fig. 6.12 for a close-up view of the modified set-up with the back reflected beams visible behind BS23 and PBS2. The back reflected light is passing the waveplate twice and therefore its polarization is rotated by  $90^\circ$  from s- to p-polarization. It is therefore transmitted by PBS2 and not going back to the telescope simulator. In fig. 6.13b a TTL measurement is shown in this configuration. The TTL coupling remains the same, so the back reflected light from the temporary pinhole is not the source of the additional TTL coupling.

Behind the beam splitter BS23 the back reflected light can be measured. One of the science QPDs was placed in the open port of the beam splitter (see fig 6.12). The measured amplitude is plotted in fig. 6.14. It is clearly visible how the amplitude of the C phase decreases with larger angles.

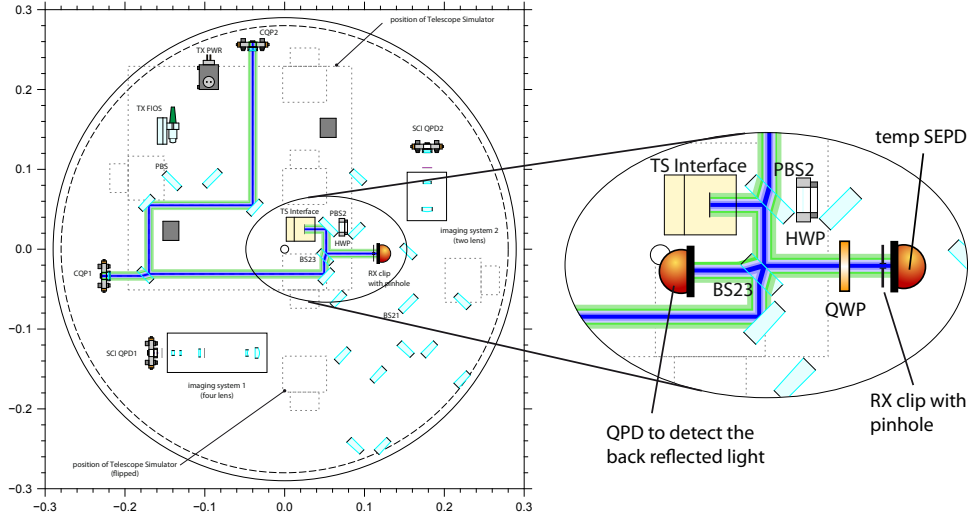
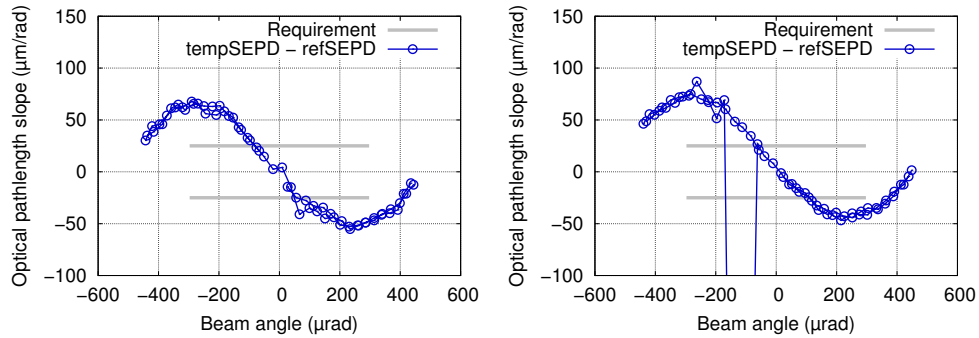


**Figure 6.12:** Setup on the optical bench to measure and suppress the light back reflected from the pinhole aperture surface. The temporary pinhole photodiode is placed in the RX aperture and an additional quarter-waveplate (QWP) is placed in front of the pinhole. The quarter-waveplate is rotating the back reflected light from s-pol to p-pol so that it is transmitted through PBS2 and not going back to reference interferometer on the telescope simulator. BS23 is a 90/10 beam splitter so the back reflected light can be detected on a photodiode placed in the open output port. The TX beam was switched off to avoid any interference.



**(a)** Slope of path length change vs. beam angle. Black cardboard pinhole in front of temp SEPD.

**(b)** Slope of path length change vs. beam angle. A QWP in front of the temp SEPD is changing the polarization of the reflected light from s- to p-pol.

**Figure 6.13**

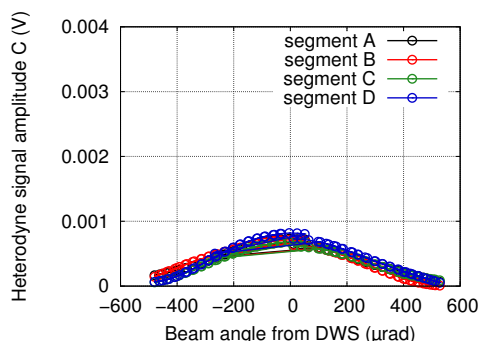


**Figure 6.14:** Amplitude of the heterodyne signal of the C phase (RX-LO) behind the open port of BS23. One of science interferometer QPDs, moved to BS23, was used for this measurement.

### Saturation of the temporary photodiode

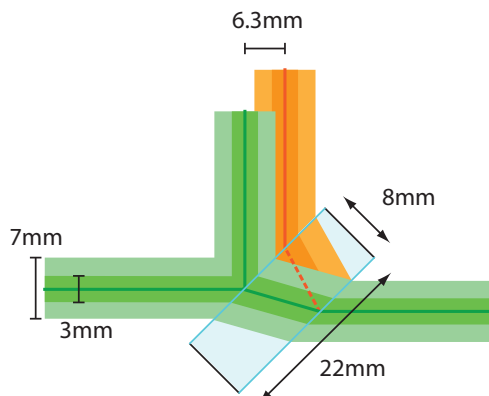
A saturation of a photodiode can lead to a phase shift, this was observed in an earlier measurement in the science interferometer. The heterodyne amplitude is angle dependent, it decreases with increasing beam angle, and this can lead to a situation where the photodiode is saturated for small angles but not for larger angles. On a pinhole photodiode the contrast does not change with angle, however it might be possible that a saturation leads to a phase drift because the photodiode response becomes non-linear. On the temporary pinhole photodiode nearly 2.5 times the power as on the reference photodiode is incident, because the beam is passing two 50/50 beam splitters before the reference photodiode, but only one 60/40 beam splitter before the temporary pinhole. However a measurement with an OD 0.5 (transmission of 0.3) neutral density filter in front of the temporary pinhole photodiode did not change the measured TTL coupling and a saturation effect was ruled out.

### Ghost beams

Ghost beams can possibly influence the two pinhole diodes differently and cause the phase difference. They occur as parasitic beams in the optical components. In fig. 6.15 the green beam is the nominal beam and the orange beam is the ghost beam, a parasitic reflection at the rear side of the component. If the component is parallel, the ghost beam is propagating in the same direction as the nominal beam with an offset dependent on the thickness of the component. In this setup the mirrors are all wedged to avoid ghost beams from the second surface co-propagating with the nominal beam, but the beam splitters are parallel.

The beam splitters have a thickness of 8 mm, which gives an offset of 6.3 mm between the nominal and the ghost beam at a  $45^\circ$  angle of incidence. The flat-top beam has an outer diameter of 7 mm, which means the inner

**Figure 6.15:** Illustration of a ghost beam from the back side of a beam splitter. The nominal beam is in green, the ghost beam in orange. The inner part of the flat-top beam is  $\sim 3$  mm in diameter, the outer part with the petals  $\sim 7$  mm. The ghost beam is not overlapping with the center of the nominal beam where the pinhole is placed but the outer part is close to the edge of the beam splitter.



150  $\mu\text{m}$ , seen by the pinhole photodiode, have no overlap with the ghost beam. However, the ghost beam gets close to the edge of the beam splitter, where the dielectric coating ends, and the ghost beam might be diffracted. The smaller beam splitters have a width of 22 mm and the coating is only 18 mm wide and does not cover the whole surface (for dimensions see [34]). Stray light from a diffracted beam could interfere with the nominal beam on the pinhole photodiode and cause small vector noise, because due to the additional distance in the beam splitter the ghost beam has a different phase to the nominal beam.

To test if ghost beams from the polarizing beam splitters are influencing the TTL coupling between the two pinholes, the power in the ghost beam was increased. The polarization of the RX beam was rotated with a half-waveplate in front of the out-of-plane optic on the telescope simulator. This increases the ghost beam generated in PBS2 on the optical bench, because more power is transmitted through the front surface and thus there is more power in the spurious reflection on the back surface. This did not affect the TTL coupling, even with a nearly  $90^\circ$  polarization rotation to maximize the ghost beam.

The ghost beams from the beam splitters have an offset parallel to the baseplate surface, the beam height and angle is the same, because the front and back surfaces are parallel. If the part of the ghost beam interfering with the nominal beam on the pinhole photodiode is coming from the outer – petal shaped – part of the flat-top beam the orientation of the aperture should make a difference. It should make a difference if a petal is exactly on the same height as the pinhole or if the pinhole position is in between petals.

This was investigated by slightly rotating the whole flat-top generator because the apodized aperture is carefully aligned to the center on the big Gaussian beam and this alignment would be spoiled if only the aperture is rotated. The rotation results in a rotation of the polarization, but this is only causing a small reduction in power in the RX beam, because the polarization is cleaned with a PBS after the fiber coupler.

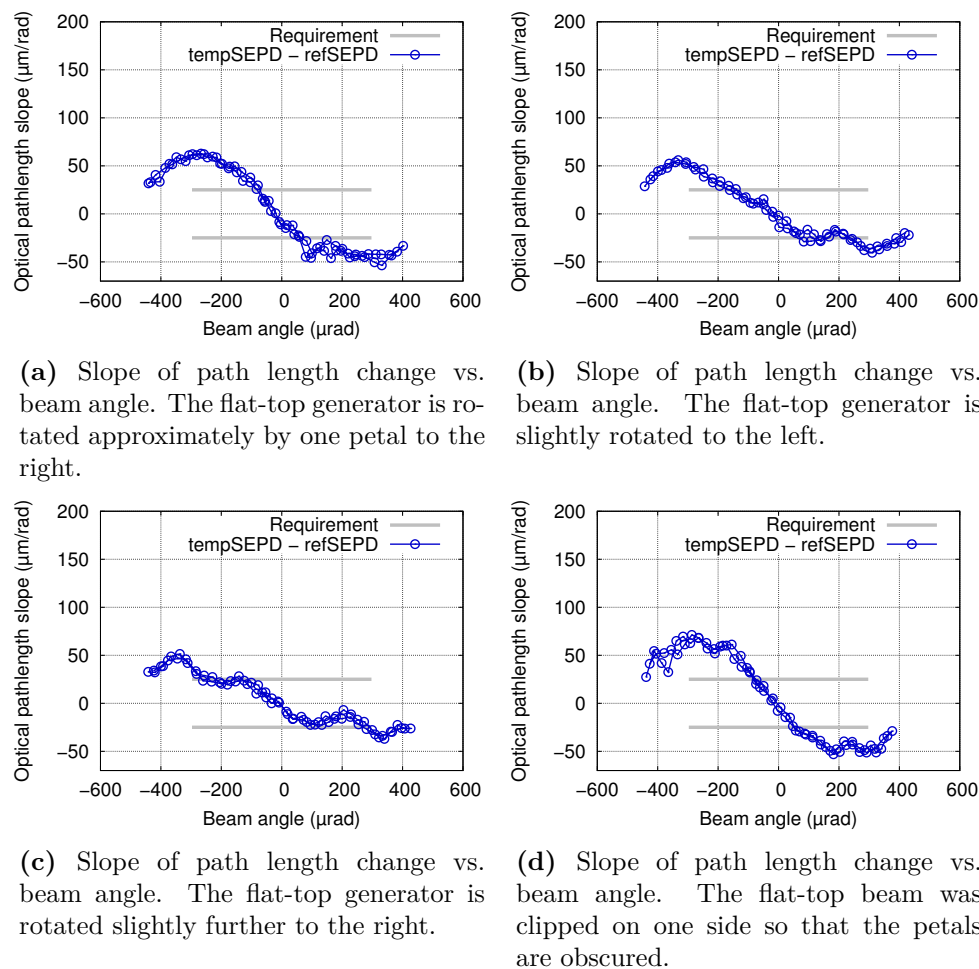


Figure 6.16

In fig. 6.16 the results are shown. The rotation of the flat-top generator did have an influence on the TTL coupling difference on the two pinhole photodiodes. In one position the requirement was nearly met, but no position could be found where the coupling was as small as for the Gaussian RX beam. Due to the lack of a fine adjustment mechanism for the rotation of the flat-top generator, it was not possible to do a systematic investigation. Even going back to the original position did not reproduce the results before starting to rotate the flat-top generator.

These results suggest that the position of the petals has an influence on the TTL coupling difference on the two pinholes. However with the unreproducible results it is not possible to understand how the orientation is affecting the coupling. If the hypothesis is true that the outer part of the flat-top beam is scattered into the nominal beam path and is interfering with the nominal

beam on the pinhole photodiode, clipping the flat-top beam on the side should remove, or at least influence, the ghost beam. In fig. 6.16d one side of the flat-top was clipped right behind the apodized aperture so that the petals on this side were not visible anymore. This did not make a difference on either side of the flat-top beam. That means the rotation of the flat-top generator has to couple in a different way.

By rotating the flat-top generator not only the orientation of the apodized aperture changes but also the polarization of the beam. Behind the PBS this should only result in a decrease of the the power. However, this was verified by changing the polarization independently of the petal positions of the aperture, by inserting a half-waveplate behind the apodized aperture. As expected that did not influence the TTL coupling measurement.

### Beam walk

A beam walk of the RX beam during the TTL coupling measurement could result in a coupling if the beam has a micro structure that is changing the phase signal on the pinhole photodiode, when the beam is scanned over the pinhole during the measurement. If the lateral position of the two pinholes in the passive axis (the one perpendicular to the tilt axis) is not exactly the same, this phase change can be different for the two pinholes.

By centering the RX beam after each angle step on the reference QPD, beam walk should be avoided, but it is possible that the centering is not very accurate for the flat-top beam. The DPS signal on the QPD is used, which is very sensitive for a Gaussian beam smaller than the photo diode, like the RX Gauss beam. The flat-top beam however, is bigger than the photo diode which has a diameter of 5.3 mm (see datasheet [62]) and the petal-shaped edge might also disturb the DPS signal.

A first attempt to improve the centering was to reduce the diameter of the flat-top beam with an additional focusing lens in front of the flat-top generator. The longest focal length available was a 1000 mm that reduced the size already significantly on the reference QPD. The measurement showed less TTL coupling but it is not clear if a better centering is responsible for the result, or the modified RX beam which was not a good flat-top beam anymore.

A different approach was taken in parallel by Max Zwetz, reported in [47]. The phase profile of the flat-top beam was analyzed, using the phase camera on the telescope simulator and a Shack-Hartmann sensor to measure the phase front of the identical spare flat-top generator. A micro structure was identified with the Shack-Hartmann sensor that could be responsible for the measured TTL coupling difference. The measurements with the phase camera also suggest that there is a beam walk of the order of 20  $\mu\text{m}$ . It could not be shown that this is the mechanism causing the additional coupling with the flat-top beam, because the resolution of both sensors is too low compared

to the pinhole to identify the exact phase structure and beam walk. It is a possible explanation, but further investigations are necessary.

### Summary and discussion

Several causes for the increased TTL coupling with the flat-top beam in the pinhole-pinhole measurement could be ruled out in this investigation. The back reflection from the pinhole aperture material, saturation effects of the temporary pinhole photodiode, ghost beams from the beams splitters and a not optimally aligned polarization of the RX beam.

A possible source of the increased coupling is a micro structure on the phase profile of the flat-top beam. For a micro structure to cause a TTL coupling difference on the two pinholes, a beam walk during the tilt measurement and an offset of the two pinholes in the passive axis is necessary, otherwise the difference between the two pinholes would be still constant. With a beam walk, the beam is scanned over the pinhole and if the pinholes are not seeing exactly the same part of the beam this can cause a TTL coupling difference. The pinholes are aligned very well in the active axis (the axis in which the beam is tilted) but not in the passive axis because that should not be critical if the phase of the flat-top beam is really flat.

Two approaches were taken to investigate this mechanism: reducing the beam walk or investigate the quality of the phase profile. A first attempt to improve the centering of the flat-top beam on the reference QPD was to reduce the beam size, but this also altered the phase profile. The measured TTL coupling was improved but it is not clear if this was caused by the improved centering or the modified beam. The phase profile was investigated by Max Zwetz, using a Shack-Hartmann sensor and a phase camera, but the resolution of both sensors was not high enough to get a clear result.

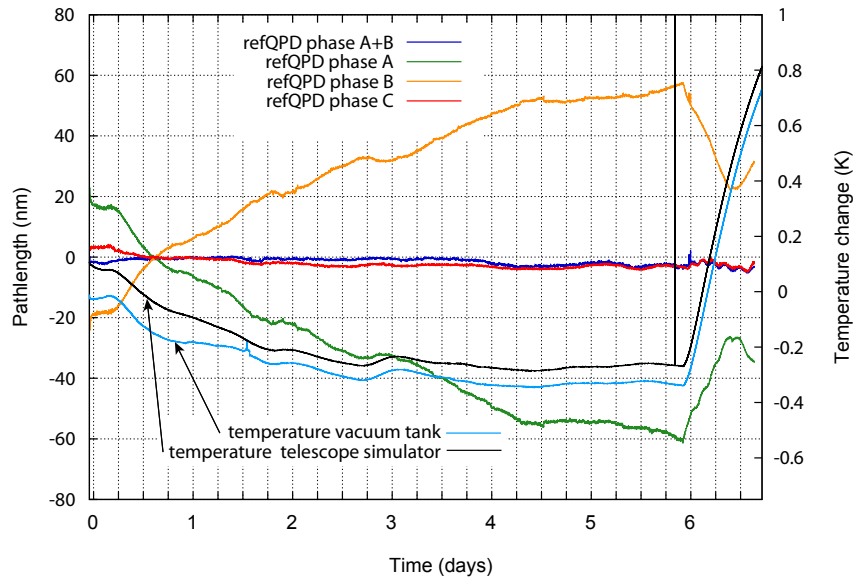
Promising ideas for future investigations of this phenomenon are, for example, using a larger QPD as the reference QPD to improve the DPS signal or installing a third pinhole photo diode to have another reference. It would be possible to replace the large auxiliary single element photodiode by a pinhole photodiode identical to the other two. The auxiliary photodiode is at the same optical distance as the other photodiodes and a pinhole there is another copy of the pinhole in the RX aperture. Another approach would be to change the properties of the flat-top beam. For comparison, the spare flat-top generator could be used or the apodized aperture could be moved slightly. This should change the micro structure in the center of the flat-top beam. If the performance cannot be improved, a different design approach for the flat-top generator might be considered. The current design is a pragmatic solution to save cost and space on the telescope simulator.

## 6.8 Temperature dependencies of the tip-tilt mount

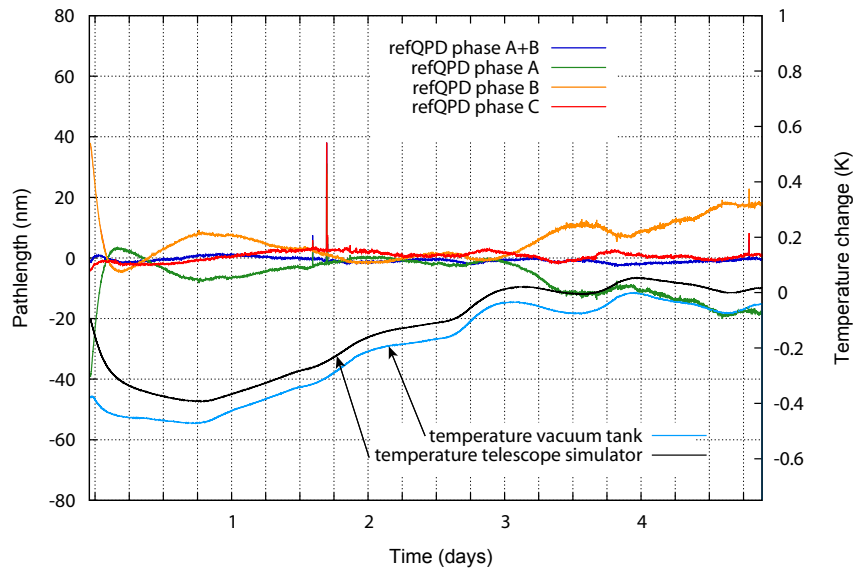
The long-term stability of the tip-tilt mount of the telescope simulator (see section 3.3) was investigated. The interferometric signals on all photodiodes were measured for several days while the tilt actuators for the RX beam were standing still. Furthermore, temperature sensors were placed within the vacuum tank to monitor the temperatures of the vacuum tank wall, the optical bench baseplate and the telescope simulator baseplate. This measurement was performed twice, once with the adjustment screws in contact to the mounting feet and once with the adjustment screws retracted, which means there was no contact between adjustment screws and mounting feet. Only with retracted adjustment screws is there an all-Zerodur<sup>®</sup> connection between the two baseplates, as intended in the design. Figure 6.17 shows the variation of the pathlength signals between science interferometer and reference pinhole for the scenario with the adjustment screws attached to the mounting feet. Figure 6.18 shows the measurement setup with the adjustment screws retracted from the mounting feet. Shown are the three phase signals, A, B and C, individually as well as the sum of the A and the B phase. The A and the B phase (shown in yellow and green) are showing a pathlength change in opposite direction because the height of the telescope simulator above the optical bench is sensed in opposite directions. The C phase is the interference of the two beams launched on the telescope simulator and the height variation is common mode for these two beams. The residual pathlength variations in the C phase and the A+B signal are probably due to angular movement of the telescope simulator which induces a tilt-to-length coupling. Both figures show additional temperature data for the vacuum chamber and the telescope simulator. In fig. 6.17 the temperature was increased at day 6 in order to investigate the experiment's response. This was achieved by increasing the temperature in the lab. In the measurement with the adjustment screws attached, a strong relation between temperature and pathlength change in the A and the B phase can be observed. Presumably the temperature driven length change of the adjustment screws is responsible for this behavior. This can not be observed in the measurement with the adjustment screws retracted. In this situation the all-Zerodur<sup>®</sup> path between optical bench and telescope simulator provides a connection with no temperature driven expansion. However, a variation in the A and B phase can still be observed. The clamping mechanism seems not strong enough in order to provide a stable connection between the two Zerodur<sup>®</sup> parts. By increasing the clamping force an improvement in the mounting feet stability was observed. The measurement in fig. 6.17 was performed with the maximal possible clamping force that can be obtained by the given mechanical design, see fig. 6.19.



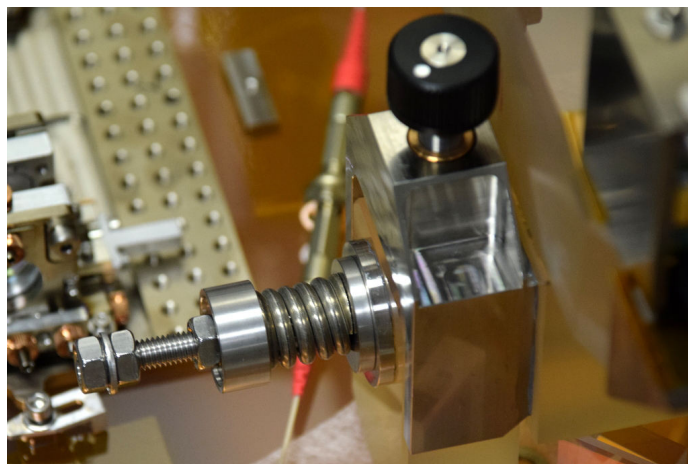
6.8. TEMPERATURE DEPENDENCIES OF THE TIP-TILT MOUNT 105



**Figure 6.17:** Longterm measurement with adjustment screws attached to the mounting feet. Phase signals and temperature data are plotted in one plot.



**Figure 6.18:** Longterm measurement with adjustment screws retracted from the mounting feet. Phase signals and temperature data are plotted in one plot.



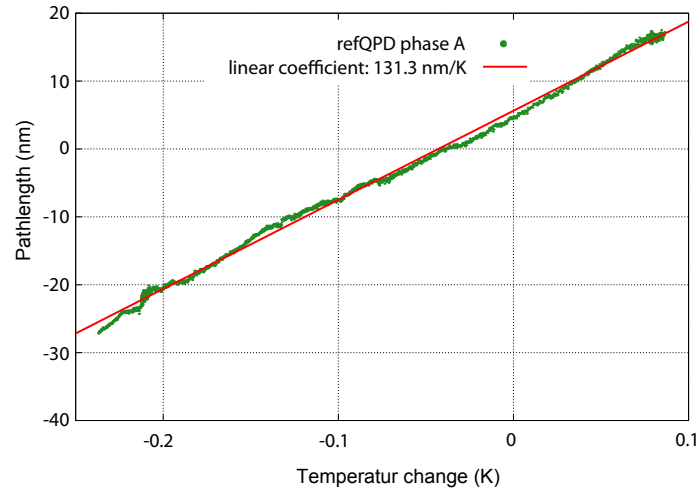
**Figure 6.19:** Clamping spring of the mounting feet in the position with the maximal possible clamping force.

Figure 6.20 and fig. 6.21 show the relation between pathlength change and temperature with adjustment screws attached and retracted, respectively. When the adjustment screws are attached, a linear correlation between temperature and pathlength can be seen with a slope of approximately 130 nm/K. The telescope simulator displacement amounts to half of this optical pathlength change. This measurement is compatible with the thermal expansion of 3 mm stainless steel ( $10.17 \cdot 10^{-6}/\text{K}$ ), 10 mm Invar ( $2 \cdot 10^{-6}/\text{K}$ ), and 120 mm Zerodur<sup>®</sup> ( $2 \cdot 10^{-8}/\text{K}$ ), which is combined approximately 53 nm/K. The amount of these three materials contributing to the total thermal expansion of one telescope simulator foot was estimated by the dimensions.

Figure 6.21 shows no linear behavior, the pathlength change seems to be not temperature driven anymore.

When the adjustment screws are attached, the height of the telescope simulator changes with temperature due to the expansion of the adjustment screws. When the adjustment screws are retracted, the change in the height of the telescope simulator is much smaller, since the Zerodur<sup>®</sup> has a much smaller coefficient of thermal expansion. However, the height of the telescope simulator is still not stable. Possibly the friction between feet and telescope simulator is not strong enough which leads to stick-slip processes.

## 6.8. TEMPERATURE DEPENDENCIES OF THE TIP-TILT MOUNT 107



**Figure 6.20:** Pathlength change plotted over the temperature change of a longterm measurement with adjustment screws attached to the mounting feet. The data is the same as in fig. 6.17 for approximately 55 h, starting half a day after the start of the measurement.

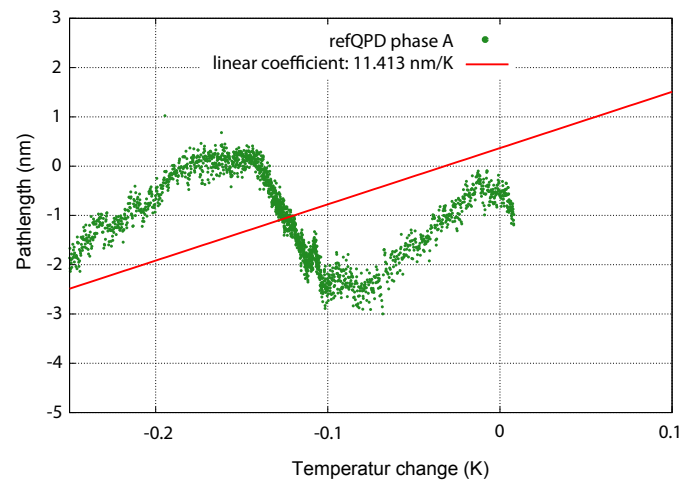


**Figure 6.21:** Pathlength change plotted over the temperature change of a longterm measurement with adjustment screws retracted from the mounting feet. The data is the same as in Fig. 6.18 for approximately 72 h, starting half a day after the start of the measurement.

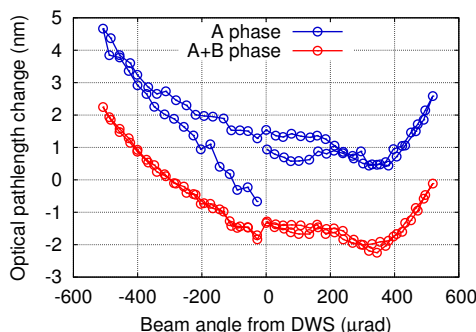


**Figure 6.22:** Pathlength change plotted over the beam angle for a comparison between A phase and A+B phase. The angle moved from zero to  $+500 \mu\text{rad}$ , then to  $-500 \mu\text{rad}$  and back to zero.

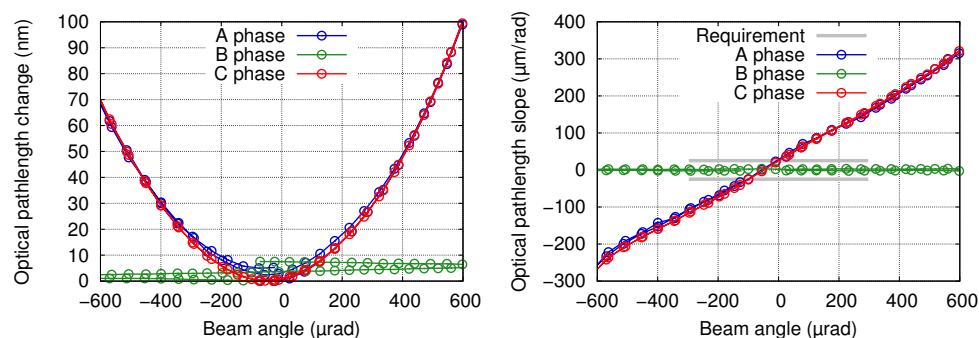
## 6.9 Telescope simulator height variation removal

The height of the telescope simulator is measured in two phase signals, in signal A between TX and RX and in signal B between LO and TX. Since the phase B measures the phase relation between two stable beams, it is a good measurement of the height variation of the telescope simulator. In the following, the phase signal of the B phase is used to correct for the height variations of the telescope simulator in the A phase. Therefore, the telescope simulator can be used with the adjustment screws attached to the mounting feet, because it is not sensitive to telescope simulator movement in the z axis anymore. Figure 6.22 shows a comparison between only A phase and A+B phase for a two-lens imaging system. In the only A phase scenario a drift can be observed which is caused by a height change of the telescope simulator. If the B phases is added, the drift disappears and the measured curve is not affected by the height variation anymore.

The remaining small variation in the A+B phase is in the same order of a few nanometers in both cases, with retracted and with attached adjustments screws. Hence, if the large drift is subtracted by using the A+B phase the performance is not improved by using the all-Zerodur feet in the design configuration without the adjustment screws. Realigning the telescope simulator is much less time consuming if the adjustment screws are attached already and it was decided to operate the setup in this configuration.

## 6.10 TTL coupling without imaging systems

In this section an initial TTL coupling measurement without imaging systems is presented. In fig. 6.23a the pathlength versus the beam angle is shown, in fig. 6.23b the numerically calculated slope of this pathlength change versus the angle.



(a) Pathlength change vs. beam angle. (b) Slope of path length change vs. beam angle.

**Figure 6.23:** TTL coupling measurement with the RX Gauss beam and no imaging systems in the science interferometer. All three phase signals A,B and C are plotted for one science interferometer photodiode. The slope is calculated numerically.

The three phase signals – A, B and C – are plotted for one science interferometer photo diode. The signal for the photo diode in the other output port looks very similar and is not plotted here. The B phase is between the two fixed beams (TX and LO) and is therefore stable over the measurement as expected. In the phase signals A and C with the tilting RX beam a large quadratic coupling is present. It is about a factor of 6 above the requirement for  $\pm 300 \mu\text{rad}$ . This clearly shows the necessity of TTL coupling suppression by imaging systems.

This initial measurement is also demonstrating the successful commissioning of the setup. The measurement procedure is working as expected and in the following it was used to investigate the performance of imaging systems.

## 6.11 Summary and conclusion of the commissioning

In this chapter the alignment, calibration and commissioning of the telescope simulator and optical bench setup was presented. Alignment signals like the DPS and DWS signals were calibrated, the telescope simulator was aligned on the optical bench using the LO beam as the alignment reference and the reference pinhole photo diode was aligned to remove the TTL coupling of the telescope simulator from the measurements.

The alignment of the reference pinhole did work well with the RX Gauss beam and the pinhole-pinhole measurements (meaning the phase difference between the reference pinhole on the telescope simulator and the temporary pinhole in the RX aperture) could be used to minimize the differential TTL coupling between the two pinholes. To center the pinholes on the beam ro-

tation point the flipping procedure was used. This ensures that the pinholes are in optically equivalent positions and in the science interferometer only the TTL coupling on the optical bench is measured.

With the flat-top beam a higher order TTL coupling remained in this pinhole-pinhole measurements, exceeding the requirement. The cause for that could not be determined, although a micro structure on the phase profile is a likely candidate. This larger higher order coupling is not present in the science interferometer and the flat-top beam can be used for the imaging systems investigations anyway.

The tip-tilt alignment mechanism of the telescope simulator was not as stable as expected from the all-Zerodur design. It is moving in the order of a few nanometers over the duration of a TTL measurement. The height change of the telescope simulator can be subtracted by using the B phase, the phase signal between the two stable beams.

At the end of the chapter, a TTL coupling measurement without imaging systems was shown to demonstrate the operational readiness of the setup and the necessity of imaging systems to meet the LISA requirements.

# Investigation of the two-lens imaging system design

Without an imaging system the RX beam tilts around the center of the RX aperture and the beam has an angle-dependent offset on the photodiode of the science interferometer. This results in a large tilt-to-length coupling as shown in section 6.10. The requirement for LISA is not met. The imaging systems are placed in the science interferometer in front of the photodiodes to reduce the tilt-to-length coupling. The pupil plane of the telescope (which will be in the RX aperture) is imaged onto the photodiode surface. With an ideal imaging system, the RX beam rotates exactly around the center of the photodiode surface with no lateral beam walk. Two sorts of imaging systems with different design approaches are tested and characterized in this thesis. In this chapter the results for the two-lens design are presented. The results for the four-lens design are presented in the next chapter.

In this chapter first the design of the two-lens imaging system and the alignment procedure are described. Then the results for the nominal performance with aligned imaging systems are shown and the results of an alignment sensitivity analysis, where individual components were misaligned intentionally.

All the measurements in this chapter show the A phase, the interference of the TX beam from the optical bench and the tilted RX beam. For the performance measurements and the sensitivity analysis the flat-top RX beam is used. In the last section an investigation with the Gaussian RX beam is shown.

## 7.1 Design and alignment

The two-lens imaging system is not using a classic pupil plane imaging scheme. The beam is not collimated on the photodiode after the two lenses. It was designed with off-the-shelf lenses to meet the requirements – tilt-to-length coupling suppression and a magnification factor of 0.4. The two-lens imaging systems was designed by Sönke Schuster using an algorithm developed by Gerhard Heinzl [63]. The main idea is to fulfill the requirements of reducing beam walk, reducing TTL coupling and providing the right magnification factor, but discarding the collimated beam that seems not to be important to fulfill the other requirements. The design is shown in fig. 7.1a more details on the lens specifications, requirements and the design criteria are given in [45], [63] and [34].

The two-lens imaging systems were pre-aligned outside of the testbed. An external setup with a tilting beam was used to reduce the beam walk behind the imaging system at the distance of the photo diode [60]. With this procedure the distance between the lenses and the relative alignment could be optimized. The height of the lenses above the optical bench could not be set to a high precision because the beam in the external setup did not have the exact same beam height as the measurement beams on the optical bench.

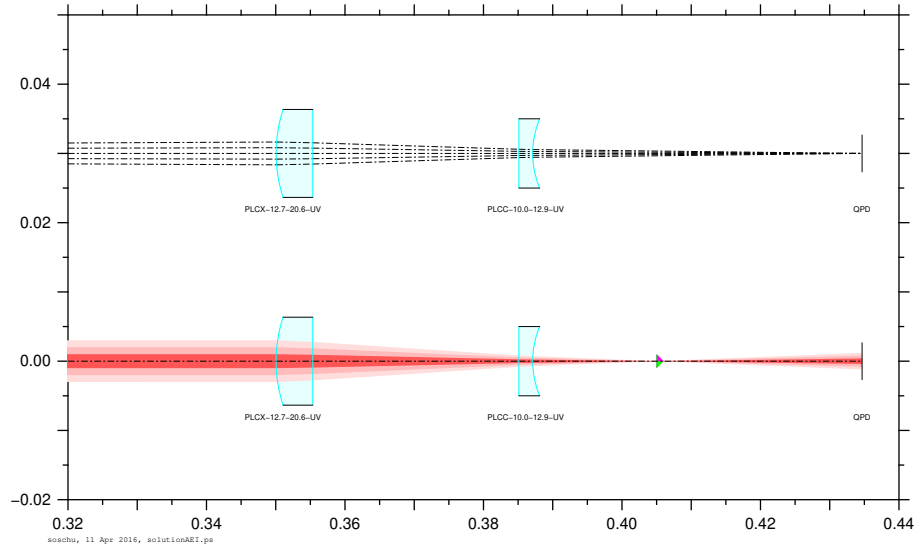
On the optical bench the height of the lenses was set by using the LO beam. The beam was centered on the science interferometer QPD first without the imaging system by adjusting the height of the photodiode and then again with the imaging system by keeping the photodiode at the same position and adjusting the height of the lenses. The horizontal positioning of the complete imaging system was also done using the QPD. The photo diode was aligned again to the center of the LO beam without an imaging system and then the imaging system position was aligned to center the beam again on the QPD.

Two identical two-lens imaging systems were built. They were both aligned and tested for nominal performance. Only one was misaligned later for the alignment sensitivity analysis.

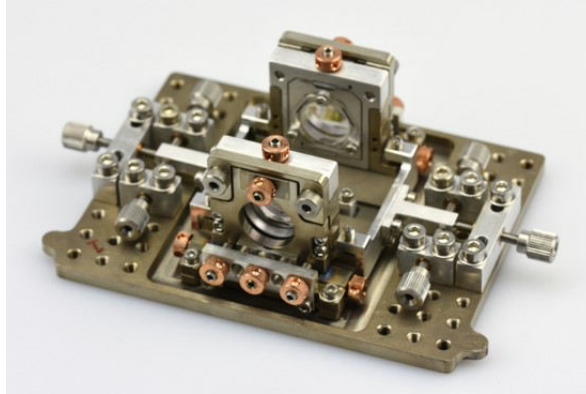
## 7.2 Nominal performance

In fig. 7.2 the nominal performance of the two-lens imaging systems with the RX flat-top beam is shown. The two measurements were taken simultaneously with a two-lens imaging system in front of both science interferometer photodiodes. On the left the pathlength change is shown, on the right the numerically calculated slope of the pathlength change. In the slope plot the  $\pm 25 \mu\text{m}/\text{rad}$  requirement is shown in grey. The measured angular range of approximately  $\pm 500 \mu\text{rad}$  is bigger than the angular range for the requirement which is  $\pm 300 \mu\text{rad}$ .



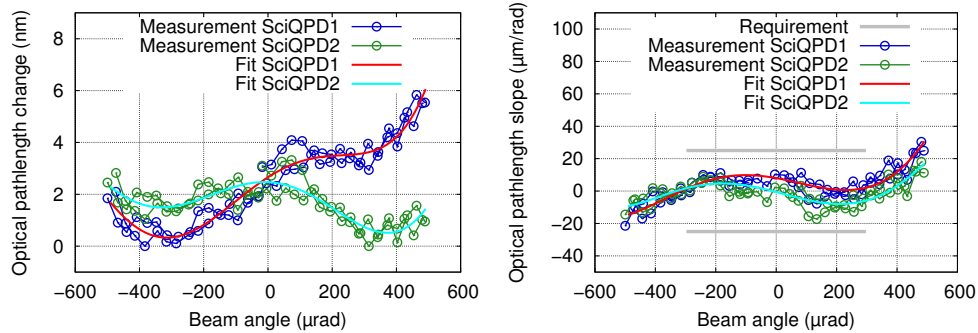


(a)



(b)

**Figure 7.1:** Optical design (a) and a photograph (b) of the two-lens imaging system. Design and figure by Sönke Schuster (reproduced from [45]). In (a) the upper plot shows the propagation of different rays, which start at the point of rotation (RX aperture) under different angles. The plot illustrates, that there is no beam walk on the photodiode. The lower plot shows the propagation of a Gaussian beam, illustrating the beam radius compression and the waist position (triangle). The beam is not collimated behind the imaging system and the waist position is in between the second lens and the photodiode. The photograph (b) of the two-lens imaging system is without the photodiode.



(a) Path length change vs. beam angle. (b) Slope of path length change vs. beam angle.

**Figure 7.2:** Two-lens imaging systems: nominal performance with the RX flat-top beam. SciQPD1 and SciQPD2 are the photodiodes in the two ports of the science interferometer. The grey lines are indicating the upper and lower bound of the requirement of  $\pm 25 \mu\text{m}/\text{rad}$  for the angular range of  $\pm 300 \mu\text{rad}$ .

The slope of the pathlength change was computed as the rolling average of the slope between two neighboring pathlength data points. Five data points, with the point for which the mean is calculated in the center, are used for the averaged slope. The slope of the pathlength change was calculated in the same way in all following plots as well.

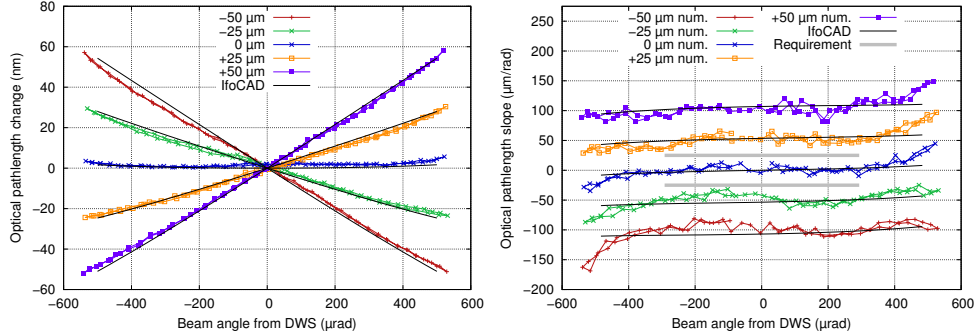
Both imaging systems are showing a very similar behavior over the measurement range and are well inside the requirement. They were both aligned using the procedure described in section (7.1). After the alignment, a small linear coupling was left because of alignment errors. This was optimized by adjusting the photo diode vertically (the direction of the tilt actuation) to get the best possible nominal performance. The imperfect alignment explains the small difference in the linear part of the coupling between the two imaging systems. One micron of photodiode misalignment already leads to  $\sim 2 \mu\text{m}/\text{rad}$  linear coupling and it is difficult to adjust the mounts with single micron resolution.

The fits plotted in fig. 7.2 are higher order polynomial fits. Details of the fit parameters are given in [45].

### 7.3 Sensitivity to misalignments

The effect of intentional misalignment of different components was investigated. Single components were systematically misaligned and the measurements are compared with optical simulations with IfoCAD done by Sönke Schuster.

The imaging system mechanical mounts were designed to allow misalignments with fine pitch screws. The lenses can be shifted individually and the



(a) Pathlength change vs. beam angle. (b) Slope of pathlength change vs. beam angle.

**Figure 7.3:** Two-lens imaging system: sensitivity to lateral QPD displacement in the vertical direction. A TTL coupling measurement in the nominal position is plotted along with measurements for four different offsets. A displacement of the photo diode results in an additional linear TTL coupling.

photo diode can be moved laterally with adjustment screws, or longitudinally by moving the whole mount on the baseplate. The sensitive axis for the alignment is in the direction of the tilt actuation.

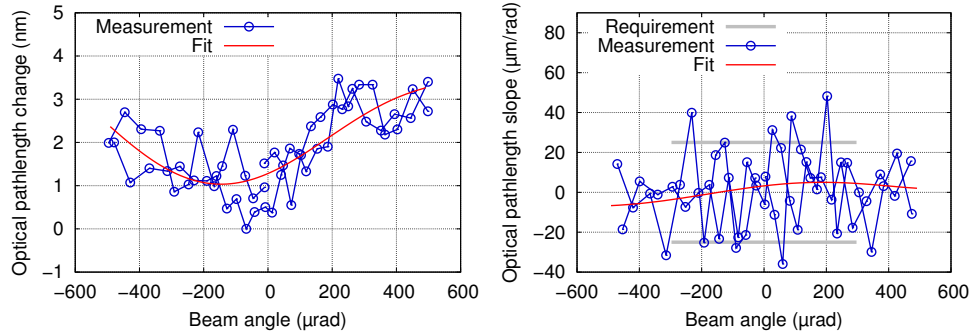
For the simulations a fundamental Gaussian TX beam with 1 mm waist radius was assumed with the position of the waist at 550 mm in front of the RX aperture. The RX flat-top beam was simulated by a large Gaussian beam with a 100 mm waist radius and a waist position at the RX aperture.

### Lateral QPD shift

Figure 7.3 shows the sensitivity of the two-lens imaging system to lateral QPD displacements in vertical direction, which is the direction of the tilt actuation.

The measurements show that a lateral misalignment of  $\pm 25 \mu\text{m}$  results in an additional TTL coupling of approximately  $\pm 50 \mu\text{m}/\text{rad}$ . With a nominal magnification factor of 0.4 for the imaging system in mind, these results match very well with the expected performance. Doubling the displacement results in a coupling twice as big and it is symmetrical for the ‘up’ and ‘down’ direction. The same result can be obtained from numerical simulations, which match the measurements very well. The slight mismatch between the two can be explained by the alignment screw which was used to adjust the QPD position. This screw has a resolution of  $200 \mu\text{m}$  per turn. Therefore, the misalignment of  $\pm 25 \mu\text{m}$  is affected by an uncertainty of at least a few micrometer.

The measurement in the nominal zero position of the photodiode was taken after the misalignment. The photodiode was adjusted to the same DPS signal



(a) Pathlength change vs. beam angle. (b) Slope of pathlength change vs. beam angle.

**Figure 7.4:** Two-lens imaging system: sensitivity to lateral displacement of the entire imaging system in x direction (perpendicular to the tilt direction). As expected this is not inducing an additional linear TTL coupling.

as in the measurement of the nominal performance, which was not exactly zero to compensate alignment errors.

### Lateral imaging system shift

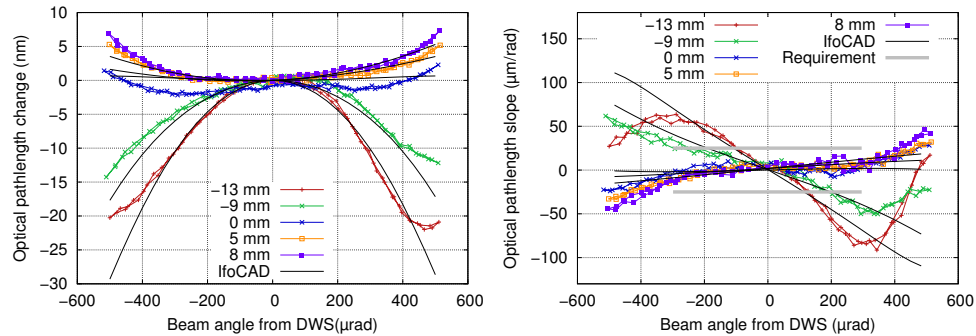
Figure 7.4 shows the sensitivity of the two-lens imaging system to lateral displacement in x direction of the entire imaging system. The x direction is horizontal, parallel to the OB baseplate and perpendicular to the tilt direction of the RX beam.

The shift of the two lenses is approximately  $25\ \mu\text{m}$  and this shift does not show in the TTL coupling. Without realigning the photo diode vertically a small linear coupling was visible because the slits of the photodiode are not aligned perfectly to the x and y direction. But by realigning the photodiode in y direction this coupling could be removed. The measurement is a little bit noisier than other measurements but this does not affect the behavior to be demonstrated and was therefore not repeated. A lateral shift in the direction perpendicular to the tilt direction does not induce an additional TTL coupling.

The same is assumed to be true for a shift of the photodiode position in the same direction. This was not verified in an additional measurement but the same principle should apply here, meaning that the alignment of the photodiode is not critical in the horizontal direction for measurements with a vertical tilt, what was observed to be true.

### Longitudinal QPD shift

Figure 7.5 shows the sensitivity of the two-lens imaging system to longitudinal QPD displacement. The longitudinal misalignment is resulting in a higher order coupling, that is dependent on the direction of the photodiode offset



(a) Pathlength change vs. beam angle. (b) Slope of pathlength change vs. beam angle.

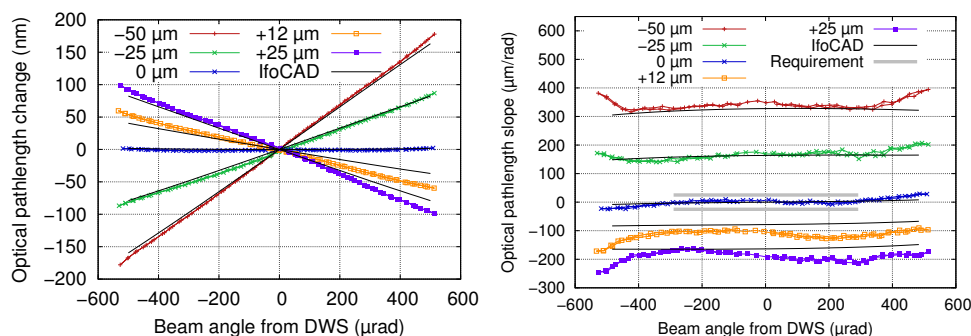
**Figure 7.5:** Two-lens imaging system: sensitivity to longitudinal displacement of the QPD. The offsets are in the order of several mm and result in an additional higher order coupling which could be reproduced by simulations in the angular range of approximately  $\pm 300 \mu\text{rad}$ .

and it is not symmetrical for both directions. The chosen offsets are larger in the negative direction – which is closer to the imaging system – because in the positive direction the tie down (part of the clamping mechanism glued to the baseplate) for the photodiode is in the way and is not allowing a position further away. Note that the offsets for these measurements are in the order of mm, much larger compared to the displacements in the lateral direction which are in the order of 10s of  $\mu\text{m}$ .

The IfoCAD simulation matches the measurements well, but not perfectly, because there are unknown parameters in the measurement. The nominal position with 0 mm offset is not defined very well in the experiment. The longitudinal distance between the two lenses of the imaging system is changing this position and the distance was only aligned by measuring the distance between the lens mounts. The longitudinal distance of the photodiode to the imaging system was also measured by measuring the distance between the mounts and estimating the position of the photodiode inside the mount. For adjusting the longitudinal position of the photodiode, the whole mount is moved on the optical bench baseplate.

Additional parameters are the beam parameters, the waist sizes and positions. They are also not known with a good precision. Given these uncertainties, the deviation between measurements and simulations are reasonable.

In the simulation the lateral shift of the photodiode was adjusted by a few microns to fit the simulation better to the measurements, which show a small linear component in the coupling.



(a) Pathlength change vs. beam angle. (b) Slope of pathlength change vs. beam angle.

**Figure 7.6:** Two-lens imaging system: sensitivity to lateral displacement of lens 1 in vertical direction. A TTL coupling measurement in the nominal position is plotted along with measurements for four different offsets which were chosen differently in the + and - direction. A displacement of the lens results in an additional linear TTL coupling.

### Lateral shift of lens one

Figure 7.6 shows the sensitivity of the two-lens imaging system to lateral displacements of lens 1 in the vertical direction. Lens 1 is plano-convex and it is the first lens in the beam path, the one furthest from the photodiode.

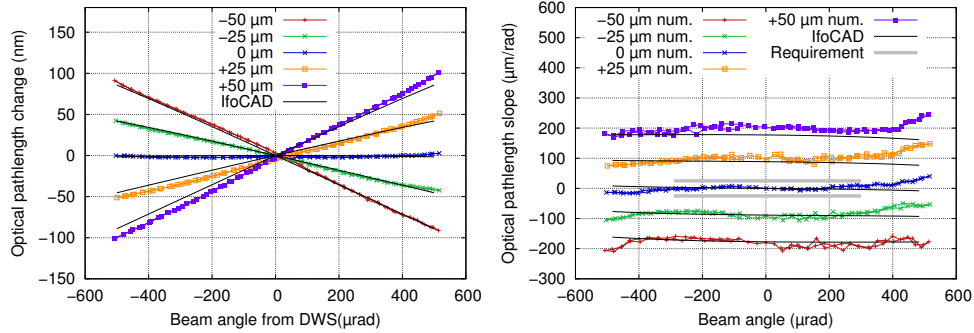
The measurements show that a lateral misalignment of  $\pm 25 \mu\text{m}$  results in an additional TTL coupling of approximately  $\pm 170 \mu\text{m}/\text{rad}$ . This is more than three times larger than the effect of a similar QPD misalignment.

In one direction, the lens is adjusted by only  $12 \mu\text{m}$ . This was one of the first measurements and it was difficult to reliably adjust the lens by such a small distance. This is probably why the simulation for the  $+12 \mu\text{m}$  has the largest deviation from the measurement. As such,  $25 \mu\text{m}$  was chosen as a more reliable step size in subsequent measurements.

### Lateral shift of lens two

Figure 7.7 shows the sensitivity of the two-lens imaging system to lateral displacement of lens 2 in vertical direction. Lens 2 is a plano-concave lens and it is directly in front of the photodiode.

The measurements show that a lateral misalignment of  $\pm 25 \mu\text{m}$  results in an additional TTL coupling of approximately  $\pm 100 \mu\text{m}/\text{rad}$ . This means that the alignment of lens 2 is a little bit less critical than the alignment of lens 1.



(a) Pathlength change vs. beam angle. (b) Slope of pathlength change vs. beam angle.

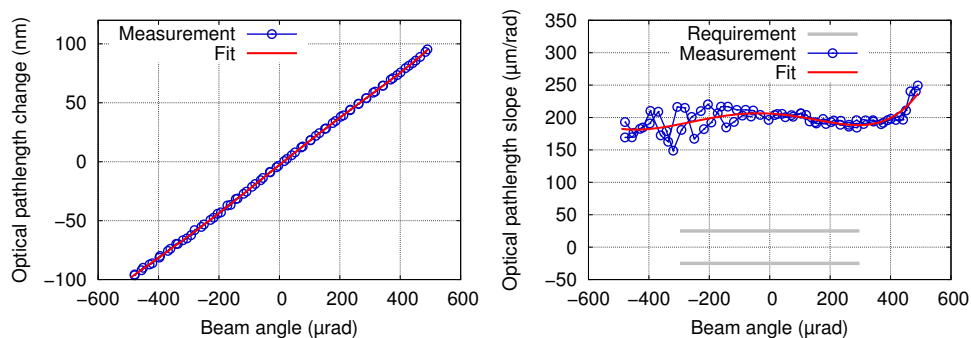
**Figure 7.7:** Two-lens imaging system: sensitivity to lateral displacement of lens 2 in vertical direction. A TTL coupling measurement in the nominal position is plotted along with measurements for four different offsets. A displacement of the lens results in an additional linear TTL coupling.

## 7.4 Compensation by photodiode alignment

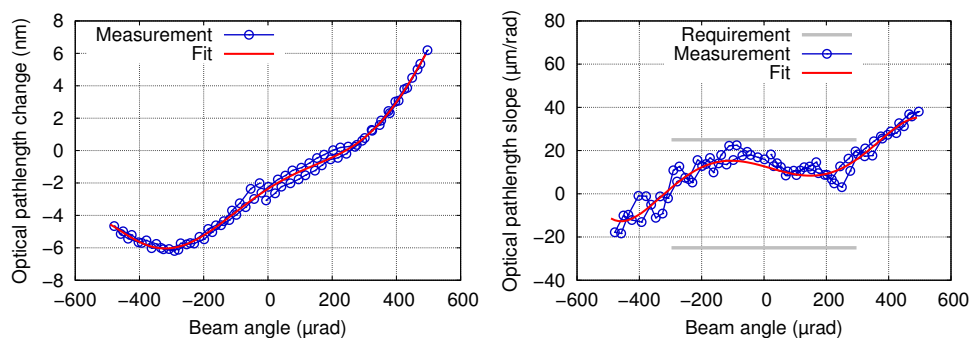
In this section it is shown that a misalignment of the imaging system can be compensated by realigning the photodiode. Here the second lens is shifted by 50  $\mu\text{m}$ , leading to a big linear coupling if the photodiode is at the nominal position (see fig. 7.8a). In fig. 7.8c and fig. 7.8d the photodiode was aligned to the center of the tilting RX beam, using the LO beam, to  $\text{DPS} = 0$ . Although the lens is still in the shifted position, the TTL coupling is reduced significantly and is within the requirement.

In fig. 7.9 the position of the photodiode was further optimized to minimize the TTL coupling. Because the imaging system is not aligned perfectly the point of minimal coupling is not exactly at  $\text{DPS} = 0$ .

Here, in this section, a dedicated measurement with a deliberate misalignment of the imaging system was made to illustrate this mechanism and to show that the compensation works. However, this method of compensation was already used to optimize the nominal performance of the imaging systems in section 7.2. This was done because the nominal alignment of the two-lens imaging system is not perfect. The initial alignment was done with an external setup to align the lenses with regard to each other and minimize the beam walk. In this setup it is not possible to control the beam height and beam angle perfectly, so the alignment was done with a slightly different beam than the beam on the Optical Bench, which leads to a height deviation of the lenses from their nominal height. However, as shown in this section, small deviations can be compensated by adjusting the photodiode position.

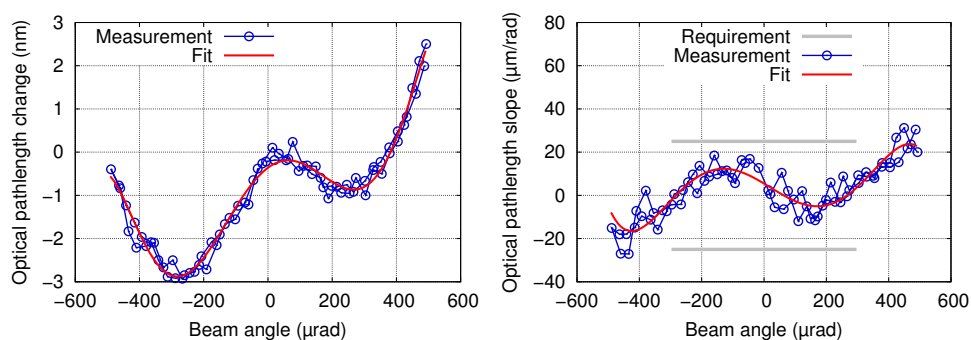


(a) Pathlength change vs. beam angle. (b) Slope of pathlength change vs. beam angle.



(c) Pathlength change vs. beam angle. (d) Slope of pathlength change vs. beam angle.

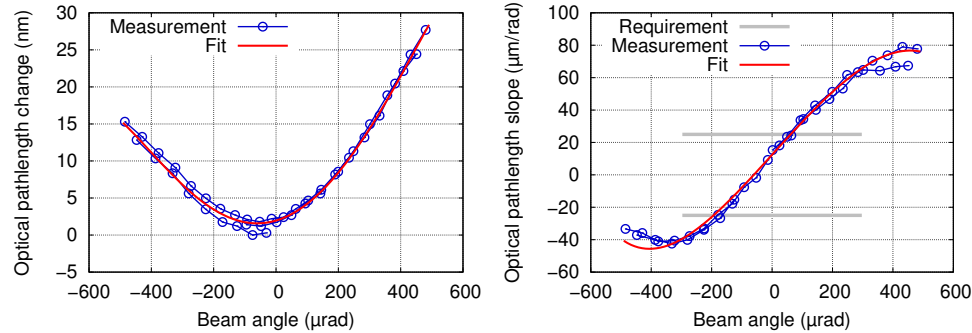
**Figure 7.8:** Linear TTL coupling because of a 50  $\mu\text{m}$  lateral misalignment of Lens2 and the result after aligning the photo diode to  $\text{DPS} = 0$ .



(a) Pathlength change vs. beam angle. (b) Slope of pathlength change vs. beam angle.

**Figure 7.9:** Result after realigning the photo diode to an optimized position to get the smallest TTL coupling.





(a) Pathlength change vs. beam angle. (b) Slope of pathlength change vs. beam angle.

**Figure 7.10:** Two-lens imaging system: nominal performance with Gaussian RX beam. The requirement is not met due to an unfortunate beam parameter combination of the RX and the TX beam.

## 7.5 Investigations with the Gaussian RX beam

The performance of the two-lens imaging system was measured with the flat-top RX beam, shown in chapter 7, and with two Gaussian beams. In this section the influence of a beam parameter mismatch of the two interfering Gaussian beams is investigated. It is shown, that initially the requirement could not be met with the two-lens system and the unmodified RX Gauss. The behavior was investigated by simulations and the beam parameters of the RX Gauss beam were modified by inserting an additional lens with a long focal length in front of the fiber coupler.

### Influence of beam parameters

Figure 7.10 shows the nominal performance of the two-lens imaging system placed in front of SciQPD1, when the Gaussian RX beam was used. The pathlength change between the averaged phase signal of SciQPD1 and the reference pinhole signal versus beam angle between the RX and the TX beam and the slope of the pathlength change versus beam angle are shown. In both cases, the beam angle was determined from the calibrated DWS signal of the reference QPD on the telescope simulator. The calibration is different to the calibration for the flat-top beam (see section 6.1).

The remaining TTL coupling does not fulfill the requirement, but it is shown later that the requirement is met with modified beam parameters. The dependency on the beam parameters was reproduced in simulations.

Sönke Schuster performed numerical simulations with IfoCAD to investigate the influence of the beam parameters. With the current setup, it was not possible to systematically investigate this effect experimentally. The simulations showed that the beam parameter combination of the TX and RX beam

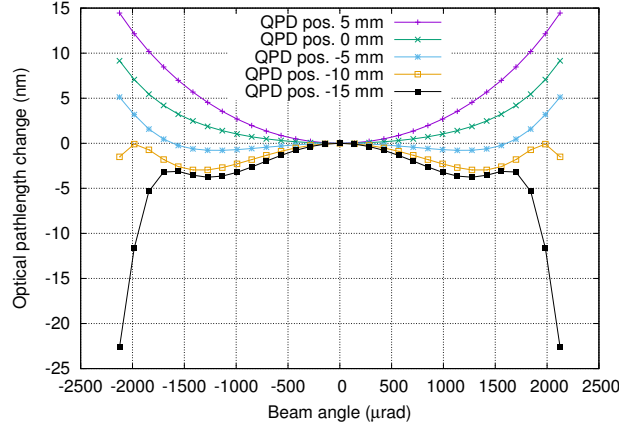


**Figure 7.11:** In this simulated data the TTL coupling of unfavorable beam parameter combinations is shown. The TTL coupling for different QPD positions is shown in order to demonstrate that the residual coupling can not be reduced with an adjustment of the QPD. The simulation was performed by Sönke Schuster.

are very unfavorable. The exact beam parameters are unknown, but for the simulations only a few unique combinations showed a comparable behavior. Most beam parameter combinations showed a much smaller TTL coupling.

An example of this behavior can be seen in fig. 7.11. For this simulation the RX beam was rotated directly around the center of the QPD, equivalent to using a perfectly aligned imaging system. This leads to a larger angular range because of the magnification factor of the imaging system of nominally 0.4. The angle scales with the inverse of the magnification factor.

The simulation parameters are: RX beam waist position 50.6 mm in front of the QPD, waist radius 25  $\mu\text{m}$ ; TX beam waist position 51.6 mm, waist radius 25  $\mu\text{m}$ ; and QPD radius 0.45 mm with a gap size of 20  $\mu\text{m}$ . The only change to a nominal two-lens system is a change of the RX waist position from 51.6 mm to 50.6 mm.

The longitudinal position of the QPD is varied to demonstrate that the residual coupling cannot be removed completely with an adjustment of the QPD. Usually, with nominal beam parameters, the parabola shaped TTL coupling becomes flat at one QPD position. With the beam parameters chosen here, this never happens because higher order polynomials appear before the parabola flattens.

The simulation shows qualitatively the behavior observed in the experiment. The beam parameters in the simulation are chosen without experimental evidence, they are solely used to reproduce the experiment's behavior. Shifting the QPD longitudinally did change the amount of TTL coupling be-

hind the imaging system, but it could not be reduced further than shown in 7.10. In this simulation the amount of remaining TTL coupling for an optimized QPD position (see QPD position -5 mm in fig. 7.11) is still smaller than in the measurement and only illustrates the behavior in principle. The simulation shown here is a preliminary result and the investigation by simulations was continued in [64], where the beam parameters are varied in a more systematic approach covering a wide range of possible mismatched beam parameters.

### TTL coupling measurements with modified beam parameters

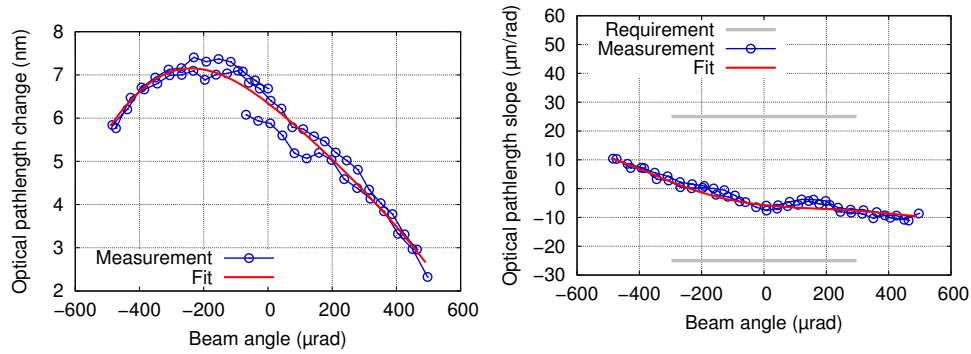
To improve the performance in this setup, the beam parameters of the RX beam were changed, in a more or less arbitrary way, by inserting an additional lens with a large focal length to move away from the unfortunate beam parameter combination.

Two different lenses were tested, with 1 m and 0.5 m focal length. Other lenses with a longer focal length would have been preferred to produce a less divergent beam, but were not at hand at that time. The lenses were placed directly behind the FIOS, before the actuators. Like this, an alignment and centering by hand without micrometer translation stages was possible, because the actuators can compensate small offsets and angular misalignment.

Figure 7.12 shows the nominal performance of the two-lens imaging system placed in front of SciQPD1 when the Gaussian RX beam was used with an additional 500 mm focal length lens in front of the RX FIOS. Due to the modified RX beam, the DWS signal calibration used for the plot in fig. 7.10 is no longer valid here. The calibration factors were scaled so that the RX beam angle range covered the same range as before (see e.g. fig. 7.10). This assumes the minimum and maximum angles are always the same and the DWS signal can be interpolated in between. This is an easy way to scale the angle without a new calibration, since the angular range does not change significantly between measurements. The optical pathlength fit parameters are shown in [45].

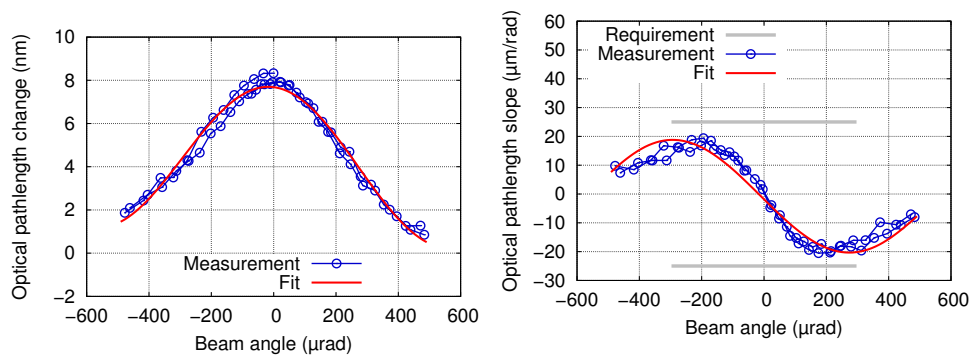
Figure 7.13 shows the nominal performance of the two-lens imaging system placed in front of SciQPD1 when the Gaussian RX beam was used with an additional 1 m focal length lens in front of the RX FIOS. The calibration for the DWS signal was scaled again, so that the RX beam angle range covered the same range as before. The optical pathlength fit parameters for this plot are also shown in [45].

With both additional lenses, the remaining TTL coupling is reduced and fulfills the requirement. The behavior is different for the different lenses, illustrating again that the TTL coupling is dependent on the specific beam parameters. However, this investigation is only qualitatively illustrating this effect, since the exact beam parameters behind the lenses could not be measured.



(a) Pathlength change vs. beam angle. (b) Slope of path length change vs. beam angle.

**Figure 7.12:** Two-lens imaging system: nominal performance with the Gaussian RX beam and an additional 500 mm focal length lens in front of the RX FIOS on the telescope simulator.



(a) Pathlength change vs. beam angle. (b) Slope of path length change vs. beam angle.

**Figure 7.13:** Two-lens imaging system: nominal performance with the Gaussian RX beam and an additional 1 m focal length lens in front of the RX FIOS on the telescope simulator.

### **Conclusion TTL coupling with two Gaussian beams**

Unequal beam parameters are in principle not a problem, but it was observed that some special combinations generate additional TTL coupling that disturbs the measurement significantly. More extensive and systematic simulations of beam parameter combinations were done in [64]. The results confirm the hypothesis that only a few unfortunate combinations lead to an increased TTL coupling. The underlying effect is the difference in the wavefront curvature of the two beams on the photodiode. The difference changes with a longitudinal shift of the photodiode because the beams are divergent behind the two-lens imaging system. If the radius of curvature is changing too much over a small range it might not be possible to find a position of the photodiode where the TTL coupling is small.

This effect is much smaller for the four-lens imaging system because the beams are collimated on the photodiode. The simulations suggest that the beam parameters are not critical for the four-lens system. In [64] an alternative two-lens design with a bigger waist radius behind the imaging system is suggested. This would be much less sensitive to unfortunate beam parameter combinations.



# Investigation of the four-lens imaging system design

The four-lens imaging system has the same purpose as the two-lens design, reducing the tilt-to-length coupling. The RX aperture is imaged on the surface of the photo diode and other design parameters, such as the distance between the RX aperture and the photodiode, and the magnification factor, are the same.

In this chapter the design of the four-lens imaging system and the alignment procedure are described. The alignment was performed at Airbus DS with a Shack-Hartmann sensor that utilised a built-in light source. The results for the nominal performance with aligned imaging systems are shown along with the results of an alignment sensitivity analysis, where individual components were misaligned intentionally. These measurements are similar to those made with the two-lens system.

All the measurements in this chapter show the A phase, the interference of the TX beam from the optical bench and the tilted RX beam, using the RX flat-top beam.

## 8.1 Design and alignment

In this section the design and the alignment procedure for the four-lens imaging systems is described. The four-lens imaging system was proposed and designed by Airbus DS.

It was designed using a classical optics approach. It has the same magnifications factor of 0.4 as the two-lens imaging system, but the beam is collimated on the photodiode. It uses spherical fused silica lenses with radii of curvature chosen from the standard tools of Zeiss. It has a pupil plane in between the first and the second pair of lenses, where a field stop can be placed to block

off-axis stray light. In fig. 8.1 the optical design and a photograph of the imaging system are shown. Details of the design requirements and chosen lenses are given in [45] and [34].

The internal alignment of the four-lens imaging system was done at Airbus DS in Ottobrunn according to their alignment plan. The first system was aligned by the author, the second by Airbus DS. The alignment could not be done at AEI because a Shack-Hartmann sensor (SHS) with a built-in light source was required.

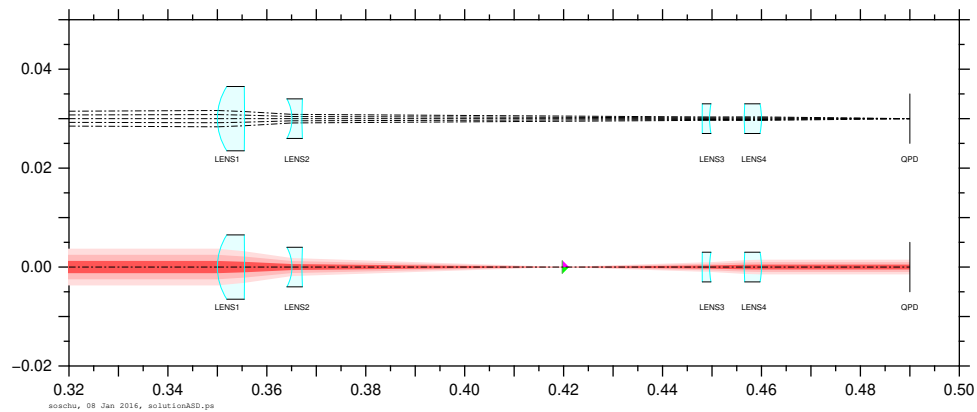
To align the lenses, a double-pass setup was used. The light from the SHS passes through the lenses twice by placing a plane mirror behind the imaging system, reflecting the beam back the same path into the SHS. The sensor compares the outgoing and incoming wavefronts internally and the difference between the wavefronts is a measure of how well the lenses are aligned with respect to the beam. The setup is shown in fig. 8.2. For aligning one lens or a pair of lenses, the beam was focused to the focal point of the lens or lens pair to obtain a collimated beam on the plane mirror. An example for the alignment of the lens pair lens 1 (L1) and lens 2 (L2) is shown schematically beneath the photograph.

After aligning the pair L1+L2, these lenses were removed from the super-baseplate (the baseplate of the whole imaging system, see 3.3 in section 3.2) and the super-baseplate was rotated by  $180^\circ$  to align the pair L3+L4 in the same way. When both lens pairs were aligned internally, the two pairs were positioned on the baseplate and aligned with regard to each other without changing the internal alignment of the lens pairs. For this step, a collimated beam from the SHS was used to get again a collimated beam behind the imaging system on the plane mirror. In fig. 8.3 the measured wavefront after aligning all four lenses is shown. The remaining tilt is subtracted because the tilt is depended on the alignment with regard to the beam of the SHS, which is different on the optical bench. The measured RMS is below  $0.02 \lambda$ , which is well inside the requirement of  $0.03 \lambda$ , defined in the design of the imaging systems [34].

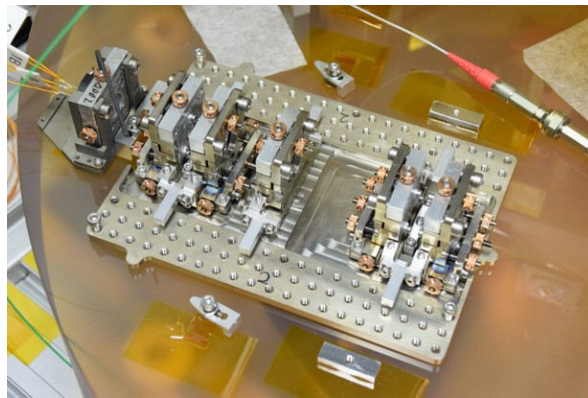
This method uses the beam of the Shack-Hartmann sensor as a reference and in the used setup it was not possible to control the position of the beam well enough to match it exactly with the height and orientation of the beams on the optical bench. For the alignment of the beam of the SHS to the imaging system super-baseplate, two pinholes were used which were manufactured to have the design height of the beam on the optical bench of 20 mm. This was sufficient for the internal alignment of the lenses, but not accurate enough to match the actual beam height, because of manufacturing tolerances and the positioning accuracy of the beam to the pinhole.

The deviation in shift and tilt in the horizontal axis is not critical, because this alignment has to be done on the optical bench directly anyway. Only the internal alignment is critical. In the vertical direction however, there is no adjustment mechanism foreseen in the mechanical design of the imaging





(a)



(b)

**Figure 8.1:** Optical design and a photograph of the four-lens imaging system. This imaging system was designed by Airbus DS and is a classic pupil plane imaging system. In (a) the upper plot shows the propagation of different rays, which start at the point of rotation (RX aperture) under different angles. The plot illustrates that there is no beam walk on the photodiode. The lower plot shows the propagation of a Gaussian beam, illustrating the beam radius compression and the waist position (triangle). The beam is collimated behind the imaging system and the waist position is in between the second and the third lens.

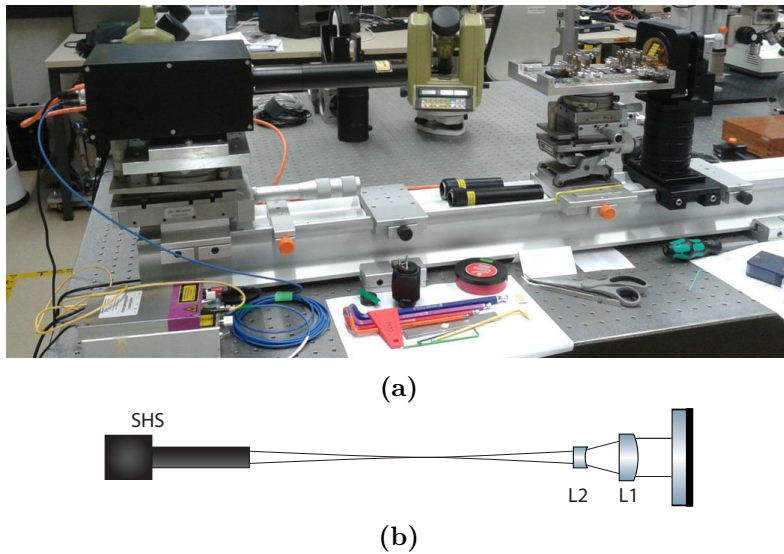


**Figure 8.2:** The setup for aligning the four-lens imaging system at Airbus DS. The back box on the left is the Shack-Hartmann sensor (SHS) with an integrated light source, mounted on translation stages to align the outgoing beam parallel to the imaging system. The imaging system is mounted on translation stages as well and behind it, a big plane mirror reflects the beam back to the SHS. In (b) a schematic of the alignment setup with lens 1 (L1) and lens 2 (L2) is shown.

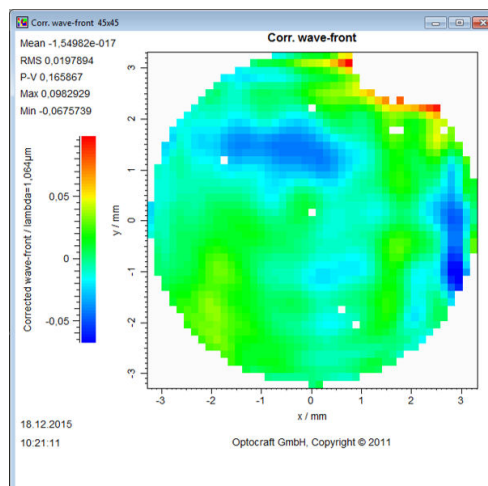


**Figure 8.3:** The wavefront measured with the SHS after aligning all four lenses. The remaining RMS of less than  $0.02 \lambda$  is well inside the requirement of the design. This figure was produced using the software provided with the SHS.

systems. Already for the internal alignment shims were required to achieve good results. Shimming was not an option on the optical bench because the deviations are too big. Shims with a height between  $100\ \mu\text{m}$  and  $200\ \mu\text{m}$  would be needed, adjusted to within  $10\ \mu\text{m}$  of the correct height, requiring a stack of shims with different thicknesses. This is unstable and not reproducible because no large clamping force can be applied to press the stack of shims together.

The first four-lens assembly, imaging system 1 in fig. 3.2, was installed on adjustment screws instead of ball-bearings. The screws, fastened to the system baseplate, allowed the height and tilt to be corrected. The LO beam was used as the reference. First, the photodiode was aligned to the center of the LO beam without the imaging system, then the imaging system was inserted and aligned such that the LO is centered again on the photodiode.

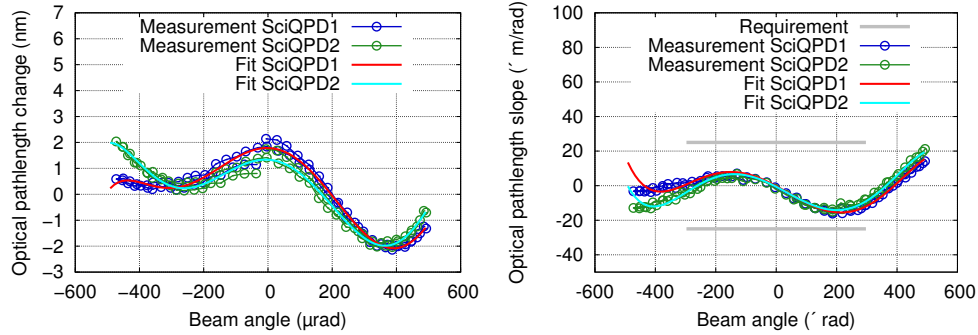
The second four-lens assembly, imaging system 2 in fig. 3.2, had lenses that were too high after the alignment. There was no simple way to lower the imaging system, instead the method of compensation by photo diode alignment was used (see section 8.4). The imaging system was aligned on the optical bench horizontally and in the vertical axis the photodiode was moved until the DPS signal was approximately zero, with a small correction to achieve the optimal performance as shown in fig. 8.4.

## 8.2 Nominal performance

In fig. 8.4 the nominal performance of the four-lens imaging system is shown. The  $\pm 25\ \mu\text{m}/\text{rad}$  requirement is shown in grey in the plot showing the slope of the pathlength change. The measured angular range of approximately  $\pm 500\ \mu\text{rad}$  is bigger than the angular range for the requirement, which is  $\pm 300\ \mu\text{rad}$ . Shown are the results for both four-lens imaging systems with the RX flat-top beam, which were measured at the same time in the two output ports of the interferometer. SciQPD1 and SciQPD2 are the two science interferometer photodiodes. To achieve this performance, the imaging systems were aligned on the optical bench as described in the previous section. The vertical angle and the height of the imaging systems had to be adjusted in addition to the horizontal positioning.

Both four-lens imaging systems are well inside the requirement and show similar behavior over the measurement range. This also demonstrates the effectiveness of adjusting the lateral position of the photodiode to compensate for the height error, as necessary for the imaging system 2 in front of SciQPD2.

The fits plotted in fig. 8.4 are higher order polynomial fits. Details of the fit parameters are given in [45].



(a) Pathlength change vs. beam angle. (b) Slope of pathlength change vs. beam angle.

**Figure 8.4:** Four-lens imaging systems: nominal performance with RX flat-top beam. SciQPD1 and SciQPD2 are the photodiodes in the two ports of the science interferometer. The grey lines indicate the upper and lower bound of the requirement of  $\pm 25 \mu\text{m}/\text{rad}$  for the angular range of  $\pm 300 \mu\text{rad}$ .

### 8.3 Sensitivity to misalignments

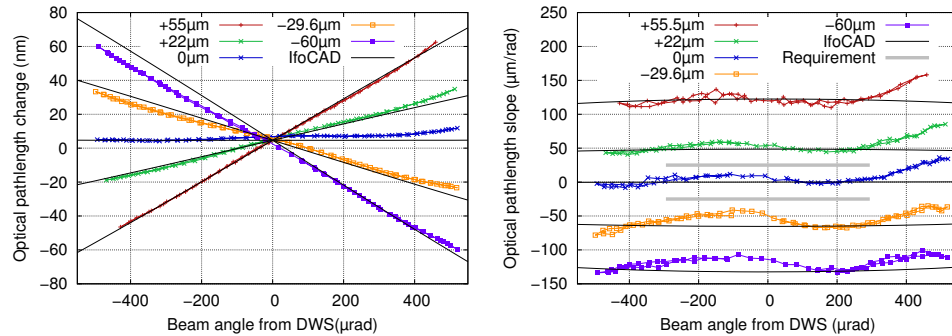
Similar to the investigation of the two-lens imaging system, systematic misalignments were investigated for the four-lens imaging system. With the fine pitch alignment screws, all components of the imaging system can be shifted individually. The change in the TTL coupling was measured for offsets of all four lenses and of the photodiode. The results are again compared to IfoCAD simulations by Sönke Schuster.

In the simulations, the same beam parameters are assumed as for the two-lens imaging system. The TX beam is a fundamental Gaussian beam with 1 mm waist radius and a waist position 550 mm in front of the RX aperture. The RX flat-top beam was simulated by a large Gaussian beam with a 100 mm waist radius and a waist position at the RX aperture.

#### Lateral QPD shift

Figure 8.5 shows the sensitivity of the four-lens imaging system to lateral QPD displacements in the vertical direction (direction of the tilt). The measurements show, that a lateral misalignment of approximately  $\pm 25 \mu\text{m}$  results in additional TTL coupling of approximately  $\pm 50 \mu\text{m}/\text{rad}$ . With a nominal magnification factor of 0.4 for the imaging system in mind, these results match very well with the expected performance.

For this measurement, the adjustment mechanism of the QPD did not work reliably and a different approach was used. Instead of estimating the offset with the alignment screw, the DPS signal was used to calculate the beam position on the QPD, and therefore the offset. To get the beam position from the analytical calculation of the DPS signal, the beam parameters and



(a) Pathlength change vs. beam angle. (b) Slope of pathlength change vs. beam angle.

**Figure 8.5:** Four-lens imaging system: sensitivity to lateral QPD displacement in the vertical direction. A TTL coupling measurement in the nominal position is plotted along with measurements for four different offsets. A displacement of the photo diode results in an additional linear TTL coupling.

the beam radius (calculated via the magnification factor) are needed. The analytical expression is given in section 2.2. The uncertainty in the actual beam radius is quite large and results in an uncertainty of the beam offset on the photodiode. Therefore, this method was only used for the QPD offsets and not for the following measurements misaligning the lenses.

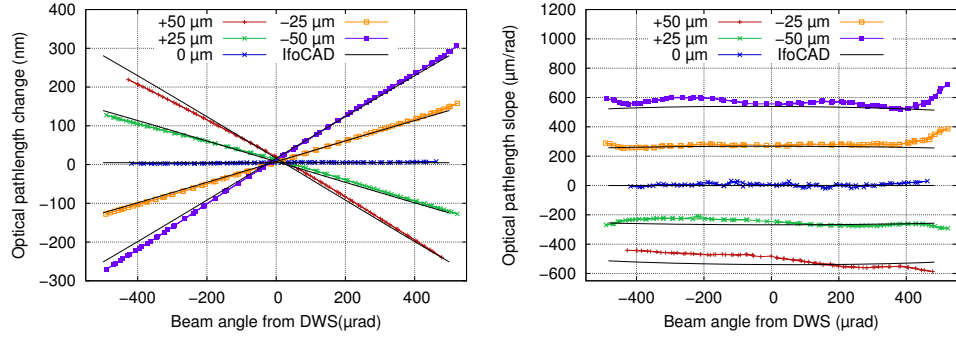
### Lateral shift of lens one

Figure 8.6 shows the sensitivity of the four-lens imaging system to lateral displacement of lens 1 in vertical direction. Lens 1 is the first lens in the beam path, the one furthest away from the photodiode. The TTL coupling depends linearly on the lens shift. For a  $\pm 25 \mu\text{m}$  shift, an additional TTL coupling of approximately  $\mp 250 \mu\text{m}/\text{rad}$  was measured. For a shift of  $\pm 50 \mu\text{m}$ , the TTL coupling becomes approximately  $\mp 530 \mu\text{m}/\text{rad}$ . This is significantly more than for the same shift of the photodiode.

### Lateral shift of lens two

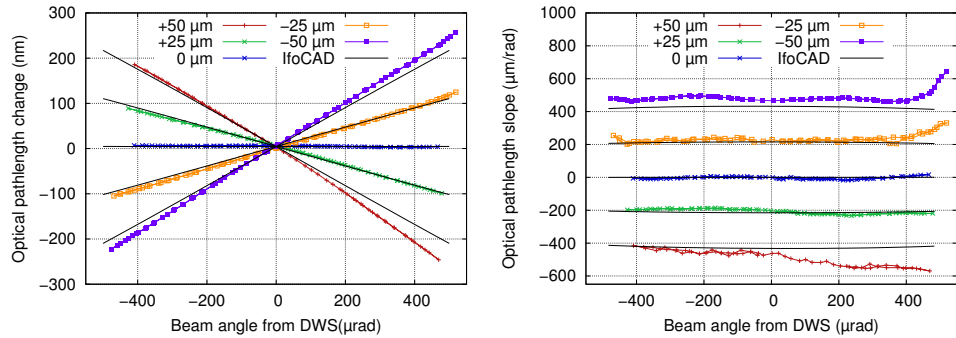
Figure 8.7 shows the sensitivity of the four-lens imaging system to lateral displacement of lens 2 in vertical direction. This is the lens directly after lens 1 in the beam path. For lens 2 for a  $\pm 25 \mu\text{m}$  shift, an additional TTL coupling of approximately  $\mp 200 \mu\text{m}/\text{rad}$  was measured. The additional coupling is a little bit less than for lens 1 for the same shift.

The measurements fit the simulations quite well here, except for some small deviations for the larger lens shifts. This is probably due to the lens mount that moves less smoothly than the other ones. For the  $+ 50 \mu\text{m}$  shift, the mechanism was stuck and the adjustment screw was turned further, until



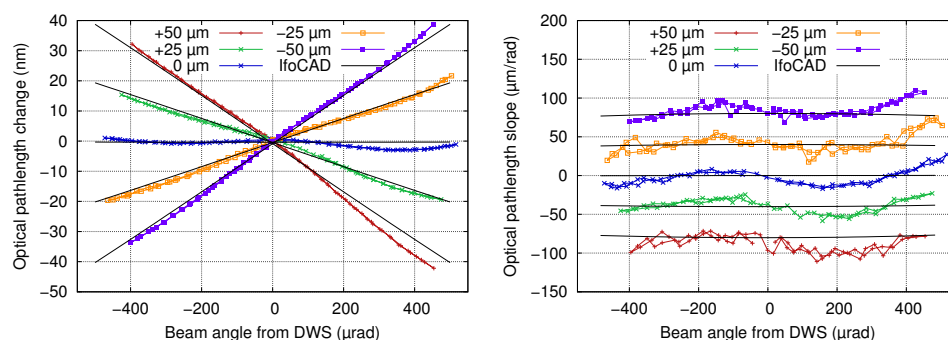
(a) Pathlength change vs. beam angle. (b) Slope of pathlength change vs. beam angle.

**Figure 8.6:** Four-lens imaging system: sensitivity to a lateral displacement of lens 1 in the vertical direction. A TTL coupling measurement in the nominal position is plotted along with measurements for four different offsets. A displacement of the lens results in an additional linear TTL coupling.



(a) Pathlength change vs. beam angle. (b) Slope of pathlength change vs. beam angle.

**Figure 8.7:** Four-lens imaging system: sensitivity to lateral displacement in vertical direction of lens 2. A TTL coupling measurement in the nominal position is plotted along with measurements for four different offsets. A displacement of the lens results in an additional linear TTL coupling.



(a) Pathlength change vs. beam angle. (b) Slope of pathlength change vs. beam angle.

**Figure 8.8:** Four-lens imaging system: sensitivity to lateral displacement in vertical direction of lens 3. A TTL coupling measurement in the nominal position is plotted along with measurements for four different offsets. A displacement of the lens results in an additional linear TTL coupling.

the DPS signal was equal and opposite to that for the  $-50\mu\text{m}$  shift. That might have caused some additional misalignment, leading to the deviation in the pathlength change slope for positive angles.

### Lateral shift of lens three

Figure 8.8 shows the sensitivity of the four-lens imaging system to lateral displacement of lens 3 in the vertical direction. Lens 3 is the third lens in the beam path.

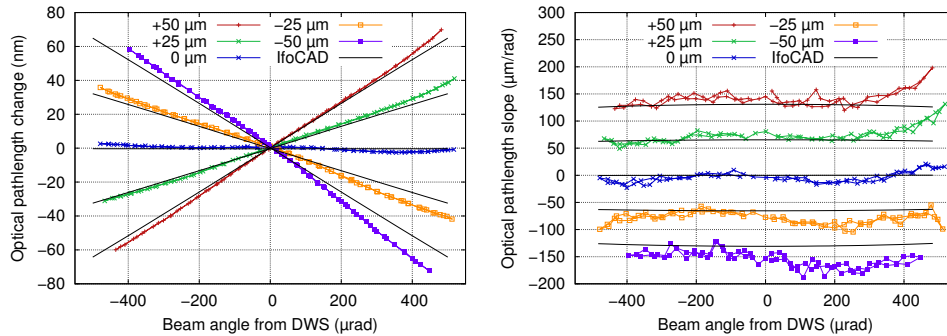
For lens 3 an additional TTL coupling of approximately  $\mp 50\mu\text{m}/\text{rad}$  for a  $\pm 25\mu\text{m}$  shift was measured. This is significantly less than for lens 1 and lens 2.

### Lateral shift of lens four

Figure 8.9 shows the sensitivity of the four-lens imaging system to lateral displacement of lens 4 in the vertical direction. Lens 4 is the last lens in the beam path, the one closest to the photodiode.

For lens 4, an additional TTL coupling of approximately  $\mp 60\mu\text{m}/\text{rad}$  for a  $\pm 25\mu\text{m}$  shift was measured. This is a little bit more than for lens 3, but still less than for the first two lenses.

A more detailed discussion of the results and a comparison between the four-lens and the two-lens system is given in section 9.



(a) Pathlength change vs. beam angle. (b) Slope of pathlength change vs. beam angle.

**Figure 8.9:** Four-lens imaging system: sensitivity to lateral displacement in vertical direction of lens 4. A TTL coupling measurement in the nominal position is plotted along with measurements for four different offsets. A displacement of the lens results in an additional linear TTL coupling.

## 8.4 Compensation by photodiode alignment

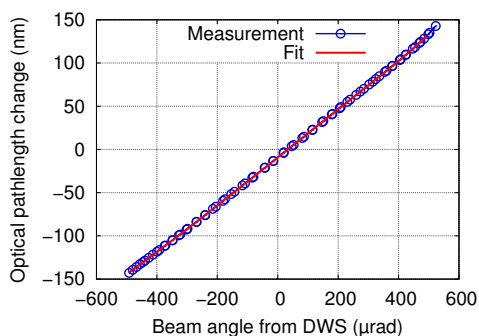
In this section it is shown that a misalignment of the imaging system can be compensated by realigning the photodiode. Here, the first lens is shifted by 25 μm downwards, which leads to a big linear coupling, if the photodiode is at the nominal position (see fig. 8.10a). In fig. 8.10c and fig. 8.10d the photodiode was aligned to the center of the LO beam, such that the DPS signal was close to zero (the same value as for nominal performance). Because the imaging system is not aligned perfectly, the point of minimal coupling is not exactly at DPS= 0. Although the lens is still in the shifted position, the TTL coupling is reduced significantly and is within the requirement.

This compensation was used to reach the nominal performance for one of the two four-lens imaging systems, because the lenses are too high and can not be lowered to match the beam height without modifying the lens mounts. In addition to this dedicated measurement, the nominal performance in fig. 8.4 already shows that this method is working.

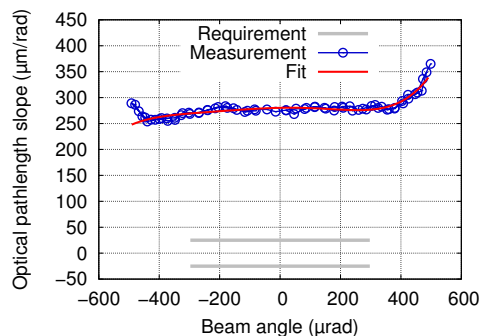
## 8.5 The effect of the field-stop

In imaging system 1, a field-stop (an aperture with 150 μm diameter) was placed in the pupil plane between the lens pairs during the alignment of the imaging system, as described in [34]. However, on the optical bench it was not possible to align the imaging system without clipping at the field stop. To test the alignment of the field-stop, the photodiode was removed and a WinCam was placed next to the optical bench in the beam path to monitor the beam. All tested positions of the imaging system showed signs of clipping

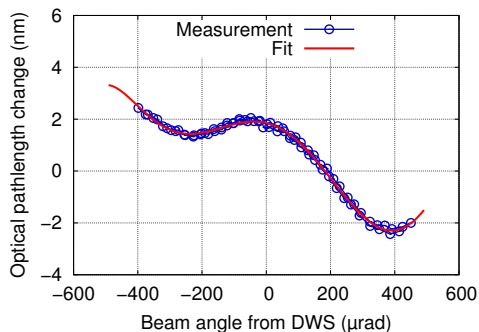




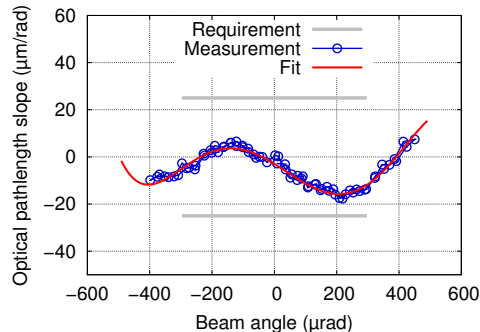
(a) Pathlength change vs. beam angle.



(b) Slope of pathlength change vs. beam angle.



(c) Pathlength change vs. beam angle.



(d) Slope of pathlength change vs. beam angle.

**Figure 8.10:** Linear TTL coupling because of a  $25\ \mu\text{m}$  lateral misalignment of lens 1 ((a) and (b)) and the result after aligning the photo diode to DPS approximately 0 ((c) and (d)).

(diffraction patterns in the beam profile) at some point in the angle range, and the field-stop was removed for all following measurements.

In fig. 8.11, a measurement with and without the field stop is shown. For the measurement with the field stop, the position was optimized with the help of the WinCam until the clipping could not be minimized further. The clipping causes a big change in the measured pathlength – due to the signal loss – and it was not possible to meet the requirement with the field stop. The second four-lens imaging system was not aligned with the field stop because of this result.

Possible reasons for the clipping by the field stop:

- The longitudinal position was not aligned well enough.
- The lateral position was not aligned well enough.
- The beam diameters are too big at the field stop.

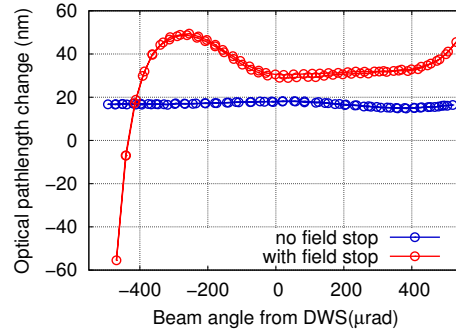


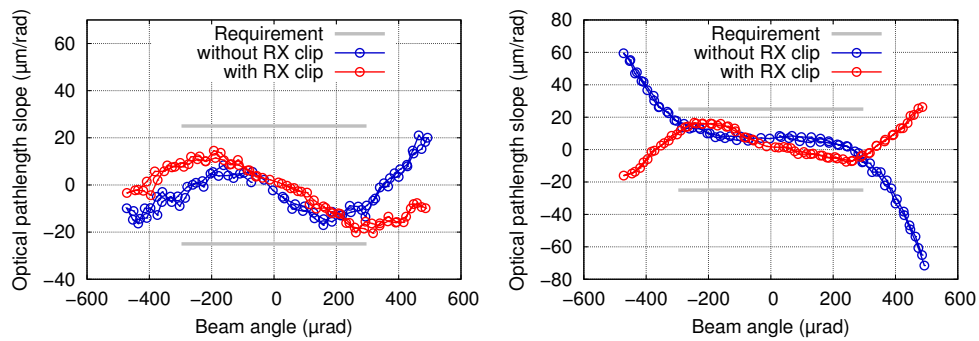
**Figure 8.11:** Pathlength change of the phase A+B versus the beam angle, showing the effect of the field-stop on the TTL coupling.

The measurements of the nominal performance of the four-lens imaging systems suggest that a field-stop is not necessary.

## 8.6 Influence of the RX aperture

The RX clip is fixed with a magnetic mount in the RX aperture and it can be removed, or replaced by different clips with different aperture designs. For the testing of the imaging systems no RX clip was used and the defining aperture is the photodiode.

With the four-lens imaging system the effect of an RX clip was investigated and the result is shown in fig. 8.12a and fig. 8.12b. It affects the A and the C phase differently because the beam diameters are different and the alignment of the telescope simulator is not perfect. In the A phase, the RX clip causes a small additional quadratic coupling that is not significant. The performance was improved by a few  $\mu\text{m}/\text{rad}$  by not using an RX clip. In the C phase the effect is bigger, changing the shape of the coupling, especially at larger angles. The RX clip is potentially poorly aligned to the LO beam, causing clipping. The C phase is not used for the performance measurements, but the RX clip was not used for the imaging system tests anyway to make sure the photodiode is the defining aperture.



(a) Slope of the pathlength change of the phase A+B versus the beam angle. (b) Slope of the pathlength change of the phase C versus the beam angle.

**Figure 8.12:** A comparison, showing the effect of the RX clip on the TTL coupling. For the measurement phase A+B the small additional coupling is not significant. The C phase shows a difference in the shape of the coupling.



## Summary and discussion

Both imaging system designs investigated here meet the LISA requirement and are possible solutions for the mission. The exact optical design needs to be adapted for the concrete mission design. The good agreement of the optical simulations with IfoCAD suggests that IfoCAD is a suitable tool to predict the performance of imaging systems. The results presented in this thesis imply that the choice of the imaging system design will be a trade-off between the complexity of the four-lens design and the sensitivity to beam parameters of the two-lens design.

The plots in fig. 9.1 summarize the misalignment sensitivity of the two different imaging systems. The resulting TTL coupling is shown as a function of the misalignment of the corresponding imaging system parameter. For each parameter the measured TTL coupling is compared with the results from simulations. All the individual lenses, as well as the photodiode, were misaligned by  $\pm 50 \mu\text{m}$ . The resulting additional linear TTL coupling is different for the different parameters. In this range for misalignment, the slope of the additional TTL coupling is linearly dependent on the offset for all lenses and photo diodes.

For the four-lens system (see Fig. 9.1a), the more critical parameters (L1 and L2) show a TTL coupling in the range of  $\pm 700 \mu\text{m}/\text{rad}$ . The less critical parameters (L3, L4 and the photo diode) show a TTL coupling of less than  $\pm 200 \mu\text{m}/\text{rad}$ . A sensitivity for the alignment of the field stop is not provided, since the requirements were not met with the field stop.

The corresponding plot for the two-lens imaging system is shown in fig. 9.1b. Here, the sensitivity to misalignments are in the range of  $-450 \mu\text{m}/\text{rad}$  for L1,  $250 \mu\text{m}/\text{rad}$  for L2 and  $150 \mu\text{m}/\text{rad}$  for the photodiode.

The four-lens system has in total only slightly more demanding requirements on the lens positions. It is, however, significantly larger and contains more components, which means more potential stray light and ghost beam

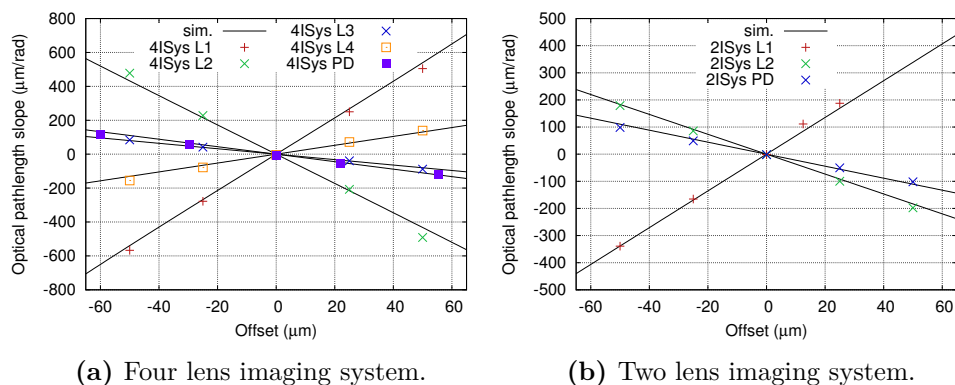


**Figure 9.1:** Sensitivity of the different misalignment parameters for both imaging systems, compared to simulated data.

sources. Since both the science and test mass interferometer will require imaging systems, the size and weight is expected to be a driver for the optical bench design.

Before considering the two-lens design for selection, a better understanding of the influence of the beam parameters is required, especially for the test mass interferometer where two Gaussian beams will be interfered. More systematic simulations and alternative lens choices are discussed in [64], but a systematic experimental study would also be desirable. Such a study would be possible in the current testbed through the addition of additional lenses or fiber couplers, although due to space constraints this would likely require custom optics and mounts.

For the science interferometer, only measurements with a flat-top beam are representative. As discussed in section 6.7, the behavior of the flat-top beam used here is not fully understood yet. The large additional TTL coupling was only present in the calibration measurements for aligning the reference pinhole and this is probably an effect that does not spoil the TTL coupling measurements, where the requirement was met without problems. If a micro structure on the phase profile is responsible for the additional coupling in the pinhole-pinhole measurement, this might average out in measurements with the whole beam. It is still desirable to either understand the behavior of the current flat-top beam or repeat the measurements with a different flat-top generator.

Another important result of this activity for the mission is the proof-of-principle of a telescope simulator. As far as the author knows, this is the first all-Zerodur<sup>®</sup> interferometer with two separate benches. A similar arrangement with independent test equipment will be necessary to test flight hardware. The telescope simulator built here is not fixed to the optical bench and does not require any additional interfaces or permanent hardware on the optical bench.

## Part III

# Preparations for performance measurements in vacuum with this setup





# Towards picometer interferometry

For investigating the TTL coupling, the picometer stability required for the LISA optical bench is not needed, because coupling factors are measured. Measuring in air saves a lot of time, because of many iterative alignment procedures and the systematic misalignment investigations. Nevertheless, the enclosed vacuum tank environment helps reducing the influence of air movement, electrostatic coupling and fast temperature changes.

Despite not strictly being necessary for the current project, the optical bench and telescope simulator assembly was built for measurements in vacuum. All the parts, including the vacuum tank, were already available from the previous EBB optical bench project. Actually operating the setup in vacuum was beyond the scope of this thesis and will be future work, but before the redirection of the project some preparatory steps were already taken to ensure the necessary environment to perform measurements with a few picometer accuracy.

In this chapter, the steps taken are reported and an outlook is given to the future work, which is necessary to reach picometer stability with the current setup. Critical for high precision measurements is the temperature stability of the experiment. The performance of the thermal shielding, already installed in the vacuum tank, was measured with high precision temperature sensors. Stringent requirements are also given for the laser frequency noise. Therefore the performance of the iodine stabilized laser was tested and a second identical laser was installed in the lab to give the possibility to monitor the performance of the laser system.

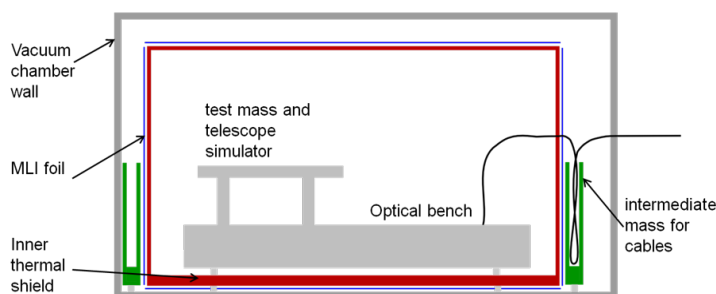


**Figure 10.1:** Schematic of the thermal insulation installed inside the vacuum chamber. The inner aluminum thermal shield is covered by multi-layer insulation foil (MLI) and the intermediate mass is providing additional thermal mass outside of the thermal shield for the cables. In addition the vacuum chamber is covered in several layers of bubble wrap foil.

## 10.1 Temperature stability

Even with an all-Zerodur setup, a very good temperature stability during measurements is essential for precision measurements. Therefore, the existing thermal shielding (an aluminum thermal shield [65]), was improved in collaboration with Christian Diekmann [16]. For measuring the temperature stability a high precision measurement system developed by Gerhard Heinzl was available. The sensor design is based on the temperature readout system developed for LISA Pathfinder ([66],[67]). As sensors, resistive elements with a temperature dependent resistance are built into a Wheatstone bridge configuration and read out differentially. Here, platinum Pt10k and NTC sensor were used. The platinum sensors provide a better absolute temperature measurements while the NTC sensors have a lower noise, but worse absolute precision. A detailed description and comparison of these sensors is given in [66].

Fig. 10.1 shows the layers of thermal insulation installed inside the vacuum chamber. The experiment is enclosed in an aluminum thermal shield with a thick baseplate to provide thermal mass. The Zerodur baseplates rest on the baseplate of the thermal shield. In the case of the temperature measurements, the interferometer baseplate was resting on another intermediate aluminum breadboard separated from the thermal shield baseplate and the Zerodur baseplate by thermally insulating Macor stand-offs. The aluminum box consists of several parts, so that the top and the sides can be removed to access the experiment. The aluminum plates were covered in multi-layer insulation (MLI) foil to reduce the heat transfer by radiation. This foil has 20 layers, alternately reflective aluminum foil and an insulating sheet. The MLI foil was fixed to the aluminum parts with insulating stand-offs to avoid short cutting the aluminum layers with a thermally conductive material. A picture of the stand-offs made of PEEK is shown in fig. 10.2. Every part of

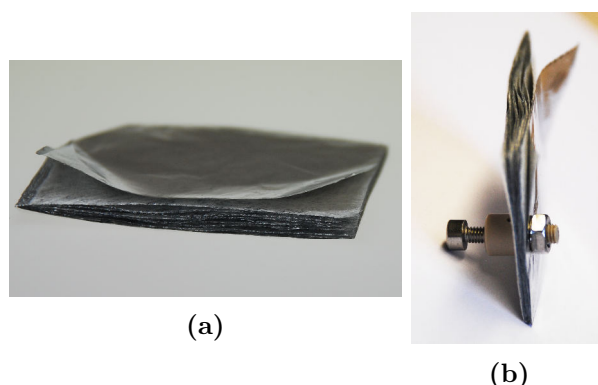


**Figure 10.2:** (a) Multi-layer insulation (MLI) foil from the side. The reflective aluminum foil layers separated by insulating layers are visible from the side. The layers are stacked loosely to avoid short cutting the aluminum layers. (b) The stand-offs designed to fix the MLI foil to the thermal shield. The PEEK parts are screwed to the aluminum plates and holes were cut into the MLI foil to fit it on the stand-offs. The foil is then fixed with nuts on the stand-offs. The nuts are only holding the foil in place, no pressure is applied to the foil to keep the individual layers stacked loosely. All sides of the thermal shield are covered individually by the foil so the thermal shield can still easily be opened.

the aluminum box was covered individually by the MLI foil to preserve the possibility to remove the sides of the thermal shield.

Another possible way of temperature coupling is via the cables going from the outside in to the vacuum tank. This can be a problem if there are a lot of cables. This effect was described in [68]. To reduce the temperature coupling through the cables, an intermediate mass was installed providing additional heat capacity not connected to the experiment. This was realized with a cable canal around the thermal shield inside the vacuum chamber. The canal has a thick aluminum base and is sitting on MACOR feet. All the cables go from the feedthrough to the intermediate mass and then through the thermal shield to the experiment.

In addition to the thermal isolation inside the vacuum tank, the tank was wrapped into three layers of bubble wrap foil. This was realized by fixing the foil to the base and the sides of the tank. For the upper side a removable cover was made so that the tank can still be opened easily.

The MLI foil did improve the temperature stability by a factor of 3 at frequencies below 3 mHz. The intermediate mass did not improve the stability, unfortunately it even increased the temperature noise slightly. These results are reported in [16].

In fig. 10.3 the achieved temperature stability inside the vacuum chamber after the installing the additional thermal insulation is shown. The readout of eight temperature sensors is plotted. The one well above the requirement was attached to the vacuum chamber wall outside the thermal shielding. The

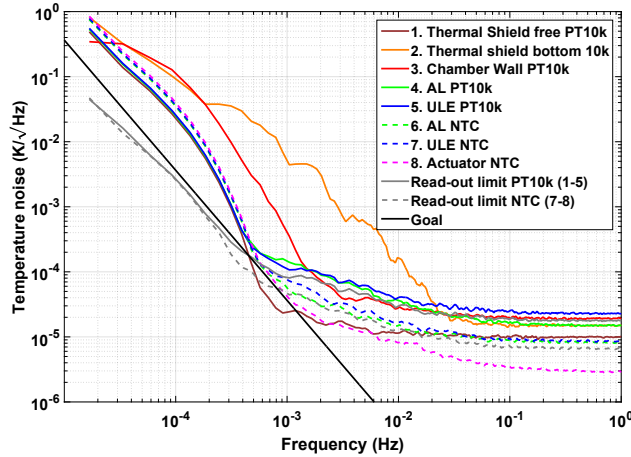


**Figure 10.3:** Spectra of the temperature readout of eight temperature sensors. 1. is in free space inside the thermal shield, 2. is attached to the baseplate of the thermal shield, 3. is attached to the wall of the vacuum chamber, 4. is attached to the aluminum breadboard between the thermal shield and the interferometer baseplate, 5. is attached to the ULE interferometer baseplate, 6. is attached to the aluminum breadboard, 7. is attached to the ULE baseplate, 8. is attached to an actuator in the interferometer. The sensor type is defined (NTC or PT10k) and the read-out limits are the difference of two sensors of the same type.

rest was distributed over various places inside the thermal shield. At lower frequencies, the goal was nearly met. At higher frequencies it is expected that the temperature stability decreases with a  $1/f$  slope, but the measurement is limited by the readout noise of the sensors at about  $10^{-5} \text{ K}/\sqrt{\text{Hz}}$ . The read-out limit in fig. 10.3 was calculated by the difference of two sensors.

## 10.2 Laser frequency stability

For precision measurements the frequency stability of the laser is crucial if the interferometer arms are not exactly matched in length. In LISA the armlength mismatch will be huge and additional techniques are necessary to cancel out the effect of the laser frequency noise (like TDI, [11]). In the combined optical bench and telescope simulator setup, the armlengths also cannot be matched because of the two separate benches. But the mismatch is much smaller and can be compensated by using a laser with very low frequency noise. For example for the EBB design, the mismatch would have been in the order of

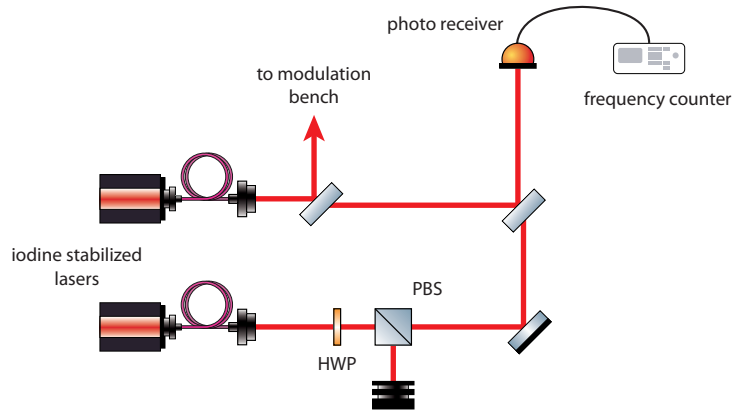


**Figure 10.4:** Setup to measure the frequency stability of the iodine stabilized laser system. As reference, a second identical laser system was used. A small pick-up from the laser used for the modulation bench is interfered with the attenuated beam from the reference system. The two laser systems were locked on two different iodine absorption lines to get a MHz beat note. The beat note is measured with a photo receiver and recorded by a frequency counter.

1.4 m. The frequency noise of the laser couples into the pathlength readout according to:

$$x_f = \Delta L \frac{\delta f}{f} \quad (10.1)$$

for a laser wavelength of  $\lambda=1064$  nm. Assuming an armlength mismatch of  $\Delta L=1.4$  m and a laser frequency noise  $\delta f=300 \text{ Hz}/\sqrt{\text{Hz}}$  this gives a pathlength noise due to frequency noise of  $x_f=1.4 \text{ pm}/\sqrt{\text{Hz}}$ . That means this frequency noise requirement allows measurements down to a few picometers.

To operate the setup in this thesis, an NPRO laser stabilized to an iodine reference was used. The laser system is commercially available from Coherent and uses their Prometheus NPRO laser [69]. Details on iodine stabilized NPROs for space-based applications and the system from Coherent can be found in [70] and [71]. Because the frequency stability is crucial to the experiment, two identical iodine stabilized laser systems were installed to have the possibility to monitor their performance. A small fraction of the laser power from the laser used for the modulation bench was interfered with the second laser and the beat note read out with a photodiode and recorded by a frequency counter (SR620 by Stanford Research Systems, Inc.). In fig. 10.4 a schematic of the measurement setup is shown. The power of the reference laser was reduced, using a  $\lambda/2$ -waveplate and a PBS. Most of the power was dumped to get comparable power levels of a few mW for both interfered beams.

The two laser systems were stabilized on two different absorption lines of the iodine reference that are separated by approximately 130 MHz. The frequency counter has a measurement range of 1.3 GHz. For one system the

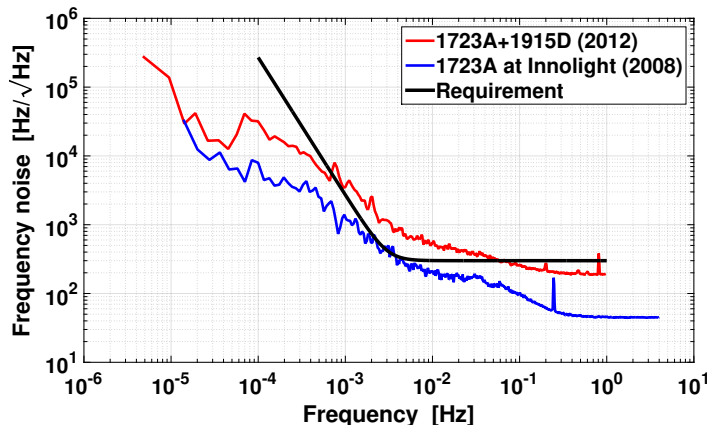


**Figure 10.5:** Measured spectrum of the two laser systems in red. 1915D and 1723A are the serial numbers of the two iodine stabilized laser systems. In comparison a similar measurement provided by the manufacturer Innolight is plotted. Here at least one of the two laser systems is not working according to the specifications. With this beat measurement it is not possible to distinguish which laser system is causing the increased frequency noise but it was assumed the older system 1723A had a reduced performance.

absorption line a1, that is recommended by the manufacturer, was chosen and for the other one the line a2. It was avoided to use a double line for the stabilization. The spectrum of the measured beat note is shown in fig. 10.5. In comparison a similar measurement performed by the manufacturer (Innolight at the time of the delivery of the first system) is plotted. In this initial measurement the frequency noise was increased over the whole frequency range compared to the frequency noise measured before delivery and the lasers did not meet the LISA requirement. With this kind of beat measurement it is not possible to distinguish which of the two laser systems is responsible for the increased frequency noise, but it was assumed the older system (serial number 1723A) lost performance. This was the reference system, the newer system (serial number 1915D) was planned to operate the EBB.

To find the cause for the reduced performance, the diagnostic port of the laser was monitored, which provides several monitoring signals like iodine stabilization error signal, the piezo actuation signal and several temperature readouts. No conspicuous feature could be found in the provided diagnostic signals. Next, the alignment of the green laser light inside the laser system used for the stabilization was optimized and the original performance could be restored. A spectrum of a measurement after the optimization is shown in fig. 10.6. The frequency noise of the two laser systems is uncorrelated and if it is assumed the performance of both systems is similar the actual performance

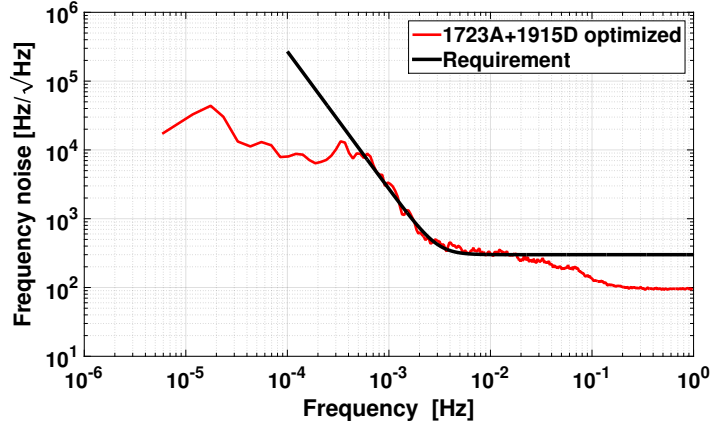


**Figure 10.6:** Measured frequency spectrum of the two laser systems after realigning the iodine stabilization of the system 1723A. The frequency noise of the two systems is uncorrelated and the measured noise level could be reduced by a factor of  $\sqrt{2}$ , if it is assumed that the actual noise is similar for both systems. The bump between 0.1 mHz and 1 mHz is probably due to temperature fluctuation because the air conditioning is fluctuating in this frequency range as well.

of one system is better by a factor of  $\sqrt{2}$ . But because it cannot be known for sure that the performance is similar for the two systems the result was not divided by  $\sqrt{2}$  and is therefore an upper limit.

### 10.3 Outlook

In this section an outlook is given on what steps will be necessary to achieve picometer stability with the current optical bench and telescope simulator setup. This list is not supposed to be complete, more challenges will probably come up during commissioning.

#### **Stability of the feet for the tip-tilt mount of the telescope simulator**

As shown in section 6.8 the all-Zerodur<sup>®</sup> feet of the telescope simulator are drifting. For the TTL coupling measurements this was not a problem because the feet could be used with the alignment screws sitting on the feet and not retracted. In this configuration the height change of the telescope simulator is mostly temperature driven and the height variations could be subtracted using the B phase signal (phase between the TX and LO beam which are not moving and therefore only seeing the height change). This will very likely not be possible on the picometer level. The drift due to temperature changes will be too large in comparison to the measured phase signal. Already small tilts

of the telescope simulator due to not evenly expanding or shrinking feet, will couple into the B phase. Therefore, it would be desirable to modify the feet so that they are working as they were designed. This means to retract the adjustment screws after the alignment of the telescope simulator and get an all-Zerodur<sup>®</sup> connection between the two baseplates. The cause of the drift is not fully understood yet but possible solutions are to increase the pressure of the screw holding the two parts of the feet together or to modify the surface quality on the parts that are pressed together to increase the friction. Another solution would be to glue the two parts together after the alignment. Of course a non-permanent solution would be preferred to maintain the flexibility of the setup.

**Thermal management** The thermal shielding described in the previous section was not fully installed for the TTL coupling measurements, because it is not necessary, but it was designed to fit the whole optical bench and telescope simulator assembly inside the thermal shield and can simply be installed again. The setup is currently operated with kHz heterodyne frequencies, so the front end electronics for the photo receivers are installed outside the vacuum chamber. It is also operated with relatively low power levels (all beams significantly below 100 mW). So there are no major heat sources in vacuum and the thermal shielding should perform as shown in the previous section. Only the phase camera on the telescope simulator produces a significant amount of heat, but can be switched off for performance measurements.

After the temperature stability measurements in vacuum, the air conditioning in the lab was modified and the temperature in the lab is significantly more stable now. It is possible that this would also improve the temperature stability inside the thermal shield.

**Amplitude stabilization** To reach the picometer performance, an amplitude stabilization of the laser beams will be necessary. The implementation is already prepared. For all three beams (TX, RX and LO) power monitor photodiodes are installed on the telescope simulator and the optical bench. A beam splitter after every FIOS provides a pick-up for these photodiodes. The power monitor mounts hold another beam splitter and two single elements photodiodes to provide an in-loop and out-of-loop amplitude measurement. The AOM driver electronics provide an amplitude modulation input to actuate the efficiency of the AOMs. The electronics were designed and built already but not yet implemented, because an amplitude stabilization is not necessary for the TTL coupling measurements.



## Summary

In the first part of this thesis the design and construction of an interferometric testbed for LISA was described. The testbed consists of two major parts: an optical bench and a telescope simulator. The optical bench has one measurement interferometer, representing the science interferometer, where the local beam is interfered with the beam received from a distant spacecraft. The telescope simulator generates a light field representative of that arriving from a distant spacecraft or a Gaussian beam representative for the test mass readout.

Only a few Zerodur interferometers with a comparable number of components as on the telescope simulator have been built at AEI ([15],[53],[54]). To the best of the author's knowledge, the testbed is the first experimental demonstration of an all-Zerodur interferometer on two separate baseplates, only constrained relative to each other by gravity. Test equipment similar to the telescope simulator built here will be necessary to test flight hardware for LISA.

A central part of the work for this thesis was the construction of the telescope simulator. The telescope simulator was built using hydroxide catalysis bonding. Template placement, assisted by a coordinate measurement machine, was used for the majority of the components.

In the second part of this thesis, the investigation of imaging systems to reduce tilt-to-length coupling was presented. First, the optical bench and telescope simulator were aligned, calibrated and commissioned. The telescope simulator was aligned on the optical bench, using the technique of microhammering, to a precision of 1-2  $\mu\text{m}$ . To ensure that the science interferometer only senses the tilt-to-length coupling of the optical bench, a reference photodiode was placed in an optically equivalent position of the interface between the two benches. To find this position, the tilt-to-length coupling difference of the reference pinhole photodiode and a temporary identical photodiode

was minimized. The difference should be zero if the two photo diodes are in equivalent positions.

The flat-top beam did show a remaining tilt-to-length coupling difference in this pinhole-pinhole measurement outside the requirement. The higher coupling was investigated within this thesis. Several possible causes could be excluded: ghost beams from the beam splitters or the reflective temporary aperture, saturation effects in the photodiodes and a misaligned polarization of the fiber injector. The cause could not be determined with certainty but a micro structure on the phase profile is a possible candidate.

Two different designs of imaging systems were investigated. A four-lens design, using classic pupil plane imaging, and a two-lens design with a divergent beam on the photodiode. It was shown that both designs meet the LISA requirement of  $\pm 25 \mu\text{m}/\text{rad}$  for angular misalignment of the received beam in the range of  $\pm 300 \mu\text{rad}$  with the flat-top beam. This requirement was also met with two Gaussian beams for the two-lens design when the beam parameters were modified. The performance of the two-lens design is dependent on beam parameter mismatch and in special cases the requirement cannot be met. The four-lens design might be less sensitive to beam parameter mismatch because the beams are collimated on the photodiode.

For both imaging system designs a systematic alignment sensitivity analysis was performed by intentionally misaligning individual components. The additional tilt-to-length coupling was mostly linear and in the range between 50 to 500  $\mu\text{m}/\text{rad}$  for a lateral offset of 50  $\mu\text{m}$ . The additional coupling scaled linearly with the offset. The results were used to verify the predictions from the optical simulation software IfoCAD. The measurements and simulations showed a good agreement.

This was the first time imaging systems for LISA were investigated experimentally in a testbed representative of the mission. The tilt-to-length coupling requirement was met using two different imaging system designs, and the testbed can be used in the future to investigate modified designs of imaging systems or different aspects of the LISA interferometry.

In the last part preparations for performing high precision measurements in vacuum with this setup were presented. The temperature stability of the optical setup was improved by passive thermal isolation using low-pass filters for heat conduction and radiation. A temperature stability below  $10^{-4} \text{K}/\sqrt{\text{Hz}}$  was achieved, close to the requirement. A laser frequency stability of 300  $\text{Hz}/\sqrt{\text{Hz}}$  or below was achieved, sufficient for  $\text{pm}/\sqrt{\text{Hz}}$  interferometric measurements.

## Read out noise floor

The noise floor in the science interferometer and the reference interferometer is calculated with the equations given in section 2.3 (from [72], [33], [23], [29]). The pathlength noise is given by:

$$\tilde{x} = \frac{\lambda}{2\pi} \times \tilde{\phi} = \frac{\lambda}{2\pi} \frac{\tilde{x}}{x_{signal,rms}} \quad (\text{A.1})$$

Where the signal is the heterodyne amplitude given by:

$$x_{signal,rms} = \eta \sqrt{2\gamma P_{TX} P_{RX}} \quad (\text{A.2})$$

The noise floor was calculated here for one segment of a quadrant photodiode or one single element photodiode, so  $P_{TX}$  and  $P_{RX}$  are the light powers of the beams on one segment or one single element photodiode (see table A.3, for the QPDs the power has to be divided by four segments).

The noise contributions taken into account here are:

$$\tilde{I}_{shot} = \sqrt{2q_e I_{ph}} \quad (\text{A.3})$$

$$\tilde{U}_{dig} = \frac{U_{LSB}}{\sqrt{6f_s}} \quad (\text{A.4})$$

$$\tilde{I}_{el} = 3.5 \text{ pA}/\sqrt{\text{Hz}} \quad (\text{A.5})$$

The input current noise  $\tilde{I}_{el}$  was estimated by a measurement in section 2.3. With A.1 the corresponding pathlength noise is then given by:

$$\tilde{x}_{shot} = \frac{\lambda}{\pi} \frac{\sqrt{q_e I_{ph}}}{\eta \sqrt{2\gamma P_{TX} P_{RX}}} \quad (\text{A.6})$$

**Table A.1:** Parameters used for the calculations

wavelength $\lambda$	1064 nm
heterodyne efficiency $\eta$	0.8
Input current noise of one segment	$3.5 \cdot 10^{-12} \text{ A}/\sqrt{\text{Hz}}$
Voltage corresponding to 1 bit $U_{LSB}$	$4.028 \cdot 10^{-4} \text{ V}$
ADC Sampling frequency $f_s$	$8.0 \cdot 10^7 \text{ Hz}$
Digitization noise $U_{dig}$	$1.839 \cdot 10^{-8} \text{ V}/\sqrt{\text{Hz}}$

$$\tilde{x}_{dig} = \frac{\lambda}{2\pi} \frac{\tilde{U}_{dig}}{R_f \eta \sqrt{2\gamma P_{TX} P_{RX}}} \quad (\text{A.7})$$

$$\tilde{x}_{el} = \frac{\lambda}{2\pi} \frac{I_{el}}{\eta \sqrt{2\gamma P_{TX} P_{RX}}} \quad (\text{A.8})$$

The parameters used for the calculation of the noise floor for all photodiodes are given in table A.1. The parameters dependent on the photodiodes are given the according section below.

For the calculations the power on the photodiodes is needed. In table A.3 the power budget assumed here is shown. The power output from the FIOSs is an estimation based on the power in the beams on the modulation bench and the actual power is dependent on the quality of the fiber coupling efficiency and the alignment on the modulation bench. The power present in the experiment is comparable to the power levels assumed here. Small losses like on the polarization beam splitters and mirrors are not taken into account for the power budget calculation.

The power budget is given for the reference QPD, the reference pinhole photodiode and a science interferometer QPD. For each beam the beam splitters passed by the beam are listed with their splitting ratio (the first number is the transmission for the beam). The photodiode (PD) is also listed in the path where clipping by the photodiode was taken into account in the power calculation. The reference QPD is a QP22-Q with a diameter of 5.3 mm (see data sheet [62]) and is only clipping the flat-top beam significantly. The reference pinhole has a diameter of 150  $\mu\text{m}$ , clipping all three beams, and the science interferometer photodiode is a GAP1000Q with a diameter of 1 mm and a beam clip with a diameter of 0.9 mm (not used in the measurements presented in this thesis but foreseen by design).

The power transmission through a round aperture placed in the center on the beam is given by [73]:

$$T = 1 - \exp\left(\frac{-2r^2}{w^2}\right) \quad (\text{A.9})$$

**Table A.2:** Transmission through a round aperture

beam	beam radius	aperture (PD)	radius	transmission T
RX flat-top	9 mm	reference QPD	2.65 mm	0.16
RX flat-top	9 mm	pinhole SEPD	75 $\mu\text{m}$	0.00014
RX flat-top	3.6 mm	science QPD	0.45 mm	0.03
TX, LO, RX Gauss	1 mm	pinhole SEPD	75 $\mu\text{m}$	0.011
TX, LO, RX Gauss	1 mm	science QPD	0.45 mm	0.92

Where  $r$  is the radius of the aperture and  $w$  the radius of the beam at the aperture. The nominal beam radius of the LO, the TX and the Gaussian RX beam is 1 mm. The beam radius of the flat-top beam is 9 mm before it is clipped at the apodized aperture (given by the specifications of the fiber coupler 60FC-T-4-M100-37 from Schäfer+Kirchhoff [74]). Since the apodized aperture is designed to minimize diffraction, the radius of the Gaussian beam was used to calculate the transmitted power.

In the science interferometer the beams are compressed by the imaging systems. The beam radii were calculated using the magnification factor of 0.4.

Table A.3: Power budget

location	LO	RX Gauss	RX flat-top	TX
fiber coupler	10 mW	2 mW	40 mW	10 mW
reference QPD				
BS13 (90/10), BS1 (50/50), BS11 (50/50), BS14 (50/50)	1.13 mW	-	-	-
BS12 (50/50), BS1 (50/50), BS11 (50/50), BS14 (50/50), PD	-	0.13 mW	0.4 mW	-
BS22 (90/10), BS2 (50/50), BS11 (50/50), BS14 (50/50)	-	-	-	1.13 mW
reference pinhole SEPD				
BS13 (90/10), BS1 (50/50), BS11 (50/50), BS14 (50/50), PD	12.6 $\mu$ W	-	-	-
BS12 (50/50), BS1 (50/50), BS11 (50/50), BS14 (50/50), PD	-	1.4 $\mu$ W	0.3 $\mu$ W	-
BS22 (90/10), BS2 (50/50), BS11 (50/50), BS14 (50/50), PD	-	-	-	12.6 mW
science QPD				
BS13 (90/10), BS1 (50/50), BS23 (60/40), BS21 (50/50), PD	1.24 mW	-	-	-
BS12 (50/50), BS1 (50/50), BS23 (60/40), BS21 (50/50), PD	-	0.14 mW	0.09 mW	-
BS22 (90/10), BS2 (50/50), BS23 (50/50), PD	-	-	-	2.07 mW

## A.1 science interferometer

The uncorrelated noise sources are added quadratically to the total pathlength noise floor (see table A.5). Here, it is calculated for one segment of one QDP in the science interferometer for the measurement signal C (TX-RX). The parameters used for this calculation specific to this photodiode are given in table A.4. The photodiode efficiency is given for a GAP1000Q InGaAs photodiode and the power in the beams are given on the photodiode (four times the power incident on one segment). The RX flat-top beam is used, because it has less power than the Gaussian RX. The total noise floor calculated here is with  $\sim 2.1 \cdot 10^{-14} \text{ m}/\sqrt{\text{Hz}}$  well below 1 pm.

**Table A.4:** parameters for one science interferometer QPD

Photodiode efficiency $\gamma$	0.7 A/W
power TX beam $P_{TX}$	2.07 mW
power RX flat-top beam $P_{RX}$	0.09 mW
<i>signal</i> (heterodyne amplitude) of one segment	0.1 mA
shot noise $n_{shot}$	$1.1 \cdot 10^{-11} \text{ A}/\sqrt{\text{Hz}}$

**Table A.5:** pathlength noise for the signal TX+RX on one segments of one science interferometer QPD

noise source	pathlength noise [ $\text{m}/\sqrt{\text{Hz}}$ ]
pathlength noise due to shot noise	$2.42 \cdot 10^{-14}$
pathlength noise due to electronic noise	$6.13 \cdot 10^{-15}$
pathlength noise due to digitizing noise	$6.44 \cdot 10^{-15}$
pathlength noise floor	$2.12 \cdot 10^{-14}$

## A.2 reference interferometer

The total pathlength noise floor in the reference interferometer is given for a QPD in table A.7 and the pinhole photodiode in table A.9. Here, it is calculated for the measurement signal C (TX-RX). The parameters used for this calculation specific to the photodiode are given in table A.4 and table A.8. The photodiode efficiency is given for a QP22-Q from First Sensor and a S5821 photodiode from Hamamatsu. The power in the beams are given on the photodiode, for the RX beam the flat-top beam was chosen for the calculation because it has less power than the Gaussian RX. The total noise floor calculated for a science interferometer QPD is with  $\sim 2.2 \cdot 10^{-14} \text{ m}/\sqrt{\text{Hz}}$  well below 1 pm. The noise floor for the reference pinhole is  $\sim 1 \text{ pm}/\sqrt{\text{Hz}}$ .

**Table A.6:** parameters for one reference interferometer QPD

Photodiode efficiency $\gamma$	0.55 A/W
power TX beam $P_{TX}$	1.13 mW
power RX beam $P_{RX}$	0.4 mW
<i>signal</i> (heterodyne amplitude) of one segment	66.7 $\mu\text{A}$
shot noise $n_{shot}$	$7.45 \cdot 10^{-12} \text{ A}/\sqrt{\text{Hz}}$

**Table A.7:** pathlength noise for the signal TX+RX on one segment of the reference interferometer QPD

noise source	pathlength noise [ $\text{m}/\sqrt{\text{Hz}}$ ]
pathlength noise due to shot noise	$2.61 \cdot 10^{-14}$
pathlength noise due to electronic noise	$8.89 \cdot 10^{-15}$
pathlength noise due to digitizing noise	$2.95 \cdot 10^{-15}$
pathlength noise floor	$2.11 \cdot 10^{-14}$



**Table A.8:** parameters for the reference pinhole photodiode

Photodiode efficiency $\gamma$	0.25 A/W
power TX beam $P_{TX}$	12.6 $\mu$ W
power RX beam $P_{RX}$	0.3 $\mu$ W
<i>signal</i> (heterodyne amplitude) of one segment	0.66 $\mu$ A
shot noise $n_{shot}$	$1.02 \cdot 10^{-12}$ A/ $\sqrt{\text{Hz}}$

**Table A.9:** pathlength noise for the signal TX+RX on the reference pinhole photodiode

noise source	pathlength noise [m/ $\sqrt{\text{Hz}}$ ]
pathlength noise due to shot noise	$3.66 \cdot 10^{-13}$
pathlength noise due to electronic noise	$8.97 \cdot 10^{-13}$
pathlength noise due to digitizing noise	$2.98 \cdot 10^{-13}$
pathlength noise floor	$1.02 \cdot 10^{-12}$



## As-built component list

In table B.1 a list of the components bonded within the work for this thesis is given. For each component the position by design is given and the measured deviation from this position. These components were all bonded using two different templates. The position was measured using the CMM. At the bottom of the table the standard deviation is given for the measured deviations from the design position. For the angle, the standard deviation is given including M8 and without M8, because this mirror has an unusually large angular misplacement, probably because it was not touching all ball bearings during the bonding process.

In fig. B.2 and fig. B.2 the layouts of the telescope simulator and the optical bench are shown with all the components labeled according to the component names used in the following tables.

In table B.2 and table B.3 the component specifications are given for all optical components on the telescope simulator and the optical bench. The substrate types are A (small beam splitter), B (small recombination beam splitter) and C (small mirror). In the specifications the coating for both sides is given, HR for high reflectivity, ARs for anti-reflective for s-polarization, ARp for anti-reflective for p-polarization or PBS for a polarization beam splitter. For the non-polarizing beam splitters the splitting ratio is given. Details of the dimensions of the different substrate types and coating specifications can be found in [19]. The specifications for the out-of-plane optics and the FIOSs are given there, too.

**Table B.1:** Component list with nominal and measured positions.

component	nominal			deviation		
	angle[deg]	x[mm]	y[mm]	angle[ $\mu$ rad]	x[ $\mu$ m]	y[ $\mu$ m]
template1						
M6	-45	120.478	24.705	17	7	-11
M5	-45	96.482	92.162	52	6	-4
BS15	45	116.402	90.582	17	13	-13
M2	45	225.000	111.522	297	11	-24
M7	135	172.678	167.340	-279	2	-17
BS14	-135	146.259	168.921	820	71	-79
BS12	135	52.000	179.500	297	-56	-96
M9	22,5	179.192	227.148	70	31	-28
M8	-157.5	142.182	264.158	2601	15	-24
template2						
M1	-135	30.000	142.500	663	-23	10
PCO3	45	53.580	144.080	122	-100	87
PCO2	135	72.920	183.576	-87	-90	-54
M4	-135	117.982	111.522	-140	-19	9
M3	-45	142.182	73.504	-140	-7	-1
M10	45	193.504	47.182	0	-13	22
PBS1	-45	196.000	76.000	-454	-31	26
BS1	45	193.504	114.018	87	-95	90
BS13	-45	197.580	143.256	-716	-29	15
standard deviation						
				700.663	44.999	47.0518
without M8:						
				365.629		

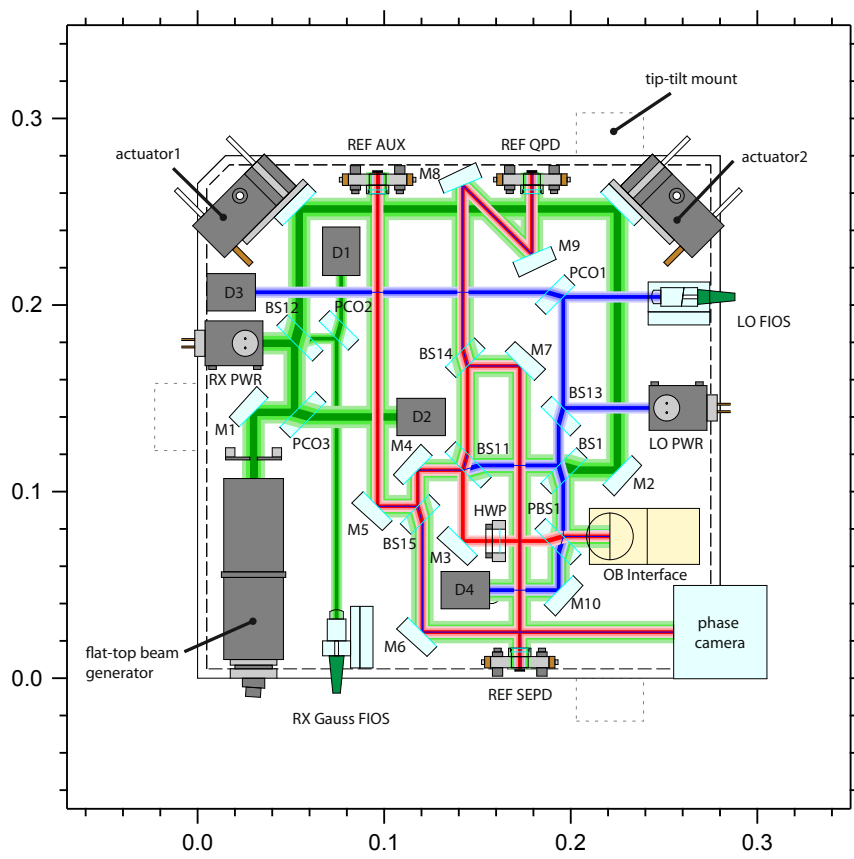


**Figure B.1:** Layout of the telescope simulator with all components labeled.

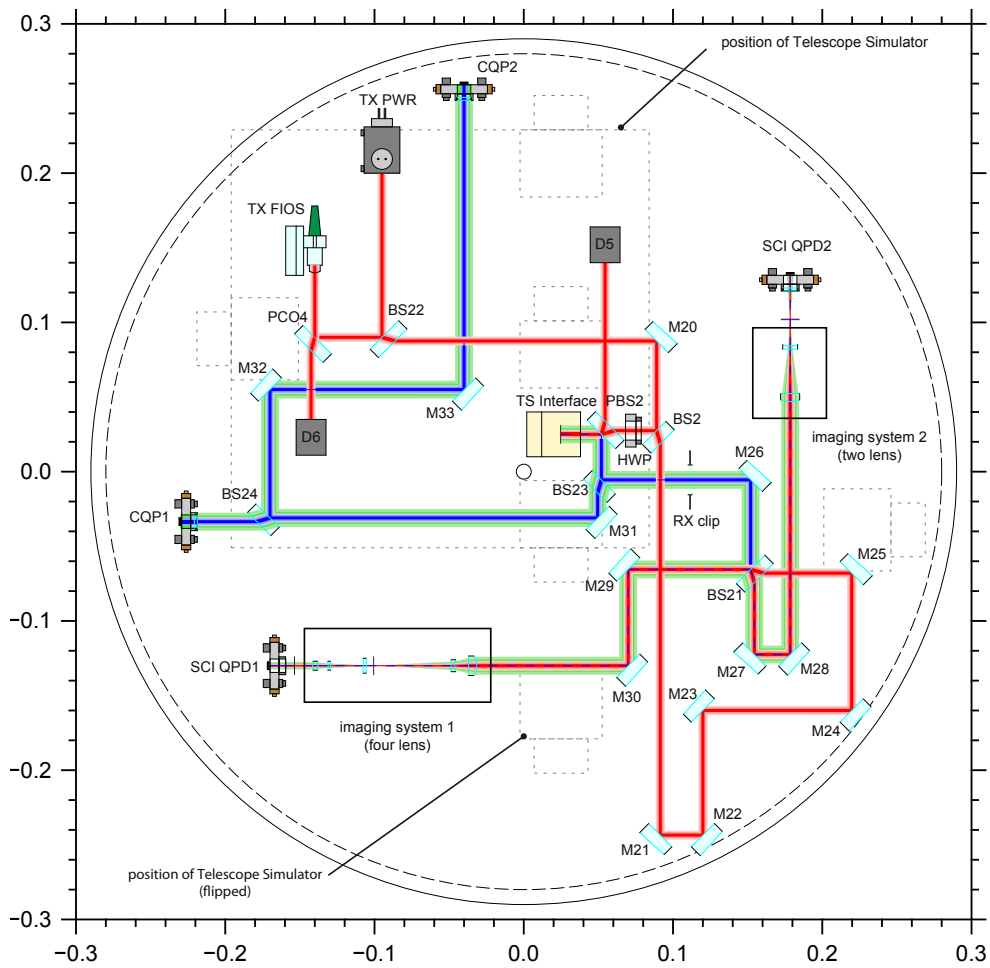


**Figure B.2:** Layout of the optical bench with all components labeled.

**Table B.2:** List of component names and specifications for the telescope simulator.

component name	substrate	coating	specification
BS13	A	4/11	10/90, ARs
BS14	A	1/11	50/50, ARs
BS15	A	1/11	50/50, ARs
PCO1	A	9/12	PBS, ARp
PCO2	A	9/12	PBS, ARp
BS12	B	1/11	50/50, ARs
BS1	B	1/11	50/50, ARs
BS11	B	1/11	50/50, ARs
PBS1	B	9/12	PBS, ARp
PCO3	B	9/12	PBS, ARp
M1	C	10/11	HR, ARs
M2	C	10/11	HR, ARs
M3	C	10/11	HR, ARs
M4	C	10/11	HR, ARs
M5	C	10/11	HR, ARs
M6	C	10/11	HR, ARs
M7	C	10/11	HR, ARs
M8	C	10/11	HR, ARs
M9	C	10/11	HR, ARs
M10	C	10/11	HR, ARs

**Table B.3:** List of component names and specifications for the optical bench.

component name	substrate	coating	specification
BS2	A	1/11	50/50, ARs
BS23	A	3/11	60/40, ARs
BS24	A	1/11	50/50, ARs
BS22	B	4/11	10/90, ARs
BS21	B	1/11	50/50, ARs
PBS2	B	9/12	PBS, ARp
PCO4	B	9/12	PBS, ARp
M20	C	10/11	HR, ARs
M21	C	10/11	HR, ARs
M22	C	10/11	HR, ARs
M23	C	10/11	HR, ARs
M24	C	10/11	HR, ARs
M25	C	10/11	HR, ARs
M26	C	10/11	HR, ARs
M27	C	10/11	HR, ARs
M28	C	10/11	HR, ARs
M29	C	10/11	HR, ARs
M30	C	10/11	HR, ARs
M31	C	10/11	HR, ARs
M32	C	10/11	HR, ARs
M33	C	10/11	HR, ARs



# Bibliography

- [1] B. P. Abbott et al., *Observation of Gravitational Waves from a Binary Black Hole Merger*, Physical Review Letters **116** (2016).
- [2] A Einstein, *Die Grundlagen der allgemeinen Relativitätstheorie*, Annalen der Physik **49**, 769 (1916).
- [3] K Danzmann et al., *The Gravitational Universe*, 2014.
- [4] The ESA L3 Gravitational Wave Mission - Gravitational Observatory Advisory Team - Final Report, <http://sci.esa.int/jump.cfm?oid=57910>, 2016.
- [5] M. Armano et al., *Sub-Femto-g Free Fall for Space-Based Gravitational Wave Observatories: LISA Pathfinder Results*, Physical Review Letters **116**, 231101 (2016).
- [6] Pau Amaro-Seoane, Sofiane Aoudia, Stanislav Babak, Pierre Binetruy, Emanuele Berti, Alejandro Bohe, Chiara Caprini, Monica Colpi, Neil J. Cornish, Karsten Danzmann, Jean-Francois Dufaux, Jonathan Gair, Oliver Jennrich, Philippe Jetzer, Antoine Klein, Ryan N. Lang, Alberto Lobo, Tyson Littenberg, Sean T. McWilliams, Gijs Nelemans, Antoine Petiteau, Edward K. Porter, Bernard F. Schutz, Alberto Sesana, Robin Stebbins, Tim Sumner, Michele Vallisneri, Stefano Vitale, Marta Volonteri, and Henry Ward, *Low-frequency gravitational-wave science with eLISA/NGO*, Classical and Quantum Gravity **29** (2012).
- [7] Alberto Sesana, *Prospects for Multiband Gravitational-Wave Astronomy after GW150914*, Physical Review Letters **116** (2016).
- [8] LISA assessment study report (Yellow Book), <http://sci.esa.int/jump.cfm?oid=48364>, 2011.
- [9] NGO assessment study report (Yellow Book), <http://sci.esa.int/jump.cfm?oid=49839>, 2012.
- [10] Massimo Tinto and Sanjeev V. Dhurandhar, *Time-Delay Interferometry*, Living Reviews In Relativity **8**, 4 (2005).

- [11] Massimo Tinto and Sanjeev V. Dhurandhar, *Time-Delay Interferometry*, Living Reviews In Relativity **17** (2014).
- [12] Glenn de Vine, Brent Ware, Kirk McKenzie, Robert E. Spero, William M. Klipstein, and Daniel A. Shaddock, *Experimental Demonstration of Time-Delay Interferometry for the Laser Interferometer Space Antenna*, Physical Review Letters **104** (2010).
- [13] Markus Otto, Gerhard Heinzel, and Karsten Danzmann, *TDI and clock noise removal for the split interferometry configuration of LISA*, Classical and Quantum Gravity **29** (2012).
- [14] F. Steier, R. Fleddermann, J. Bogenstahl, C. Diekmann, G. Heinzel, and K. Danzmann, *Construction of the LISA back-side fibre link interferometer prototype*, Classical and Quantum Gravity **26** (2009).
- [15] Roland Fleddermann, *Interferometry for a space-based gravitational wave observatory*, PhD thesis, Leibniz Universität Hannover, Hannover, 2012.
- [16] Christian Diekmann, *Development of core elements for the LISA optical bench - Electro-optical measurement systems and test devices*, PhD thesis, Leibniz Universität Hannover, Hannover, 2012.
- [17] Maike Lieser, E Fitzsimons, K-S Isleif, C Killow, M Perreur-Lloyd, D Robertson, S Schuster, M Tröbs, S Veith, H Ward, G Heinzel, and K Danzmann, *Construction of an optical test-bed for eLISA*, Journal of Physics: Conference Series **716**, 012029 (2016).
- [18] C Brugger, B Broll, E Fitzsimons, U. Johann, W Jonke, S. Lucarelli, S. Nikolov, M Voert, D. Weise, and G Witvoet, An experiment to test in-field pointing for eLISA, in *Proceedings of the 10th International Conference on Space Optics*, 2014.
- [19] Michael Perreur-Lloyd, Christian Killow, Ewan Fitzsimons, David Robertson, Harry Ward, and Alasdair Taylor, LOB-TN-8.2-11-UGL 'Optical Bench EBB Design Definition File', Technical report, 2011.
- [20] O. Jennrich, *LISA technology and instrumentation*, Classical and Quantum Gravity **26** (2009).
- [21] J. Pijnenburg, N Rijnveld, and H. Hogenhuis, Extremely stable piezo mechanisms for the New Gravitational wave Observatory, in *Proceedings of the 9th International Conference on Space Optics*, 2012.
- [22] L. d'Arcio, J. Bogenstahl, C. Diekmann, E. D. Fitzsimons, G Heinzel, H. Hogenhuis, C. J. Killow, M. Lieser, S. Nikolov, M. Perreur-Lloyd, J. Pijnenburg, D Robertson, A. Taylor, M. Tröbs, H. Ward, and D. Weise, An

- Elegant Breadboard of the Optical Bench for eLISA/NGO, in *Proceedings of the 9th International Conference on Space Optics*, 2012.
- [23] S Barke, Y Wang, J J Esteban Delgado, M Tröbs, G Heinzel, and K Danzmann, *Towards a gravitational wave observatory designer: sensitivity limits of spaceborne detectors*, *Classical and Quantum Gravity* **32**, 095004 (2015).
- [24] Gudrun Wanner, *Complex optical systems in space : numerical modelling of the heterodyne interferometry of LISA Pathfinder and LISA*, PhD thesis, Leibniz Universität Hannover, 2010.
- [25] Gudrun Wanner, Gerhard Heinzel, Evgenia Kochkina, Christoph Mahrtdt, Benjamin S. Sheard, Soenke Schuster, and Karsten Danzmann, *Methods for simulating the readout of lengths and angles in laser interferometers with Gaussian beams*, *Optics Communications* **285**, 4831 (2012).
- [26] Gudrun Wanner, Soenke Schuster, Michael Troebs, and Gerhard Heinzel, A brief comparison of optical pathlength difference and various definitions for the interferometric phase, in *10th International LISA Symposium*, volume 610 of *Journal of Physics Conference Series*, Univ Florida, Gainesville, FL, 2015, 10th International LISA Symposium, Univ Florida, Gainesville, FL, MAY 18-23, 2014.
- [27] G. Heinzel, V. Wand, A. Garcia, O. Jennrich, C. Braxmaier, D. Robertson, K. Middleton, D. Hoyland, A. Rüdiger, R. Schilling, U. Johann, and K. Danzmann, *The LTP interferometer and phasemeter*, *Classical and Quantum Gravity* **21**, S581 (2004).
- [28] Oliver Gerberding, Christian Diekmann, Joachim Kullmann, Michael Troebs, Ioury Bykov, Simon Barke, Nils Christopher Brause, Juan Jose Esteban Delgado, Thomas S. Schwarze, Jens Reiche, Karsten Danzmann, Torben Rasmussen, Torben Vendt Hansen, Anders Enggaard, Soren Moller Pedersen, Oliver Jennrich, Martin Suess, Zoran Sodnik, and Gerhard Heinzel, *Readout for intersatellite laser interferometry: Measuring low frequency phase fluctuations of high-frequency signals with micro-radian precision*, *Review of Scientific Instruments* **86** (2015).
- [29] Simon Barke, *Inter-Spacecraft Frequency Distribution for Future Gravitational Wave Observatories*, PhD thesis, Leibniz Universität Hannover, Hannover, 2015.
- [30] Gerhard Heinzel, *Advanced optical techniques for laser-interferometric gravitational-wave detectors*, PhD thesis, Universität Hannover, 1999.
- [31] F. Guzman Cervantes, J. Livas, R. Silverberg, E. Buchanan, and R. Stebbins, *Characterization of photoreceivers for LISA*, *Classical and Quantum Gravity* **28**, 094010 (2011).

- [32] Christian Diekmann, Phasenstabilisierung und -auslesung für LISA, Diploma Thesis, 2008, Leibniz Universität Hannover.
- [33] G. Heinzel, A. Rüdiger, and R. Schilling, Spectrum and spectral density estimation by the Discrete Fourier transform (DFT), including a comprehensive list of window functions and some new at-top windows., 2002.
- [34] Ewan Fitzsimons, Michael Perreur-Lloyd, Michael Tröbs, Sönke Schuster, and Germán Fernández Barranco, LOB-TN-14-10-ASD – Detailed Design of Tilt-to-Piston Investigation, Technical report, Airbus Defence and Space, University of Glasgow, AEI Hannover, 2015.
- [35] O. Gerberding, *Phase readout for satellite interferometry*, PhD thesis, Leibniz Universität Hannover, 2014.
- [36] Gerhard Heinzel, personal communication.
- [37] Soenke Schuster, Gudrun Wanner, Michael Troebs, and Gerhard Heinzel, *Vanishing tilt-to-length coupling for a singular case in two-beam laser interferometers with Gaussian beams*, Applied optics **54**, 1010 (2015).
- [38] D. Weise, LOB-ASD-TN-006-02 'OB Requirements Specification and Justification', Technical report, 2010.
- [39] Soenke Schuster, Michael Troebs, Gudrun Wanner, and Gerhard Heinzel, *Experimental demonstration of reduced tilt-to-length coupling by a two-lens imaging system*, Optics Express **24** (2016).
- [40] Evgenia Kochkina, G. Heinzel, G. Wanner, V. Mueller, C. Mahrtdt, B. Sheard, S. Schuster, and K. Danzmann, Simulating and Optimizing Laser Interferometers, in *9th LISA Symposium*, volume 467 of *Astronomical Society of the Pacific Conference Series*, pages 291–292, 2013, Paris, France, May, 2012.
- [41] Marina Dehne, Michael Troebs, Gerhard Heinzel, and Karsten Danzmann, *Verification of polarising optics for the LISA optical bench*, Optics Express **20**, 27273 (2012).
- [42] A. Taylor, L. d’Arcio, J. Bogenstahl, K. Danzmann, C. Diekmann, E. D. Fitzsimons, O. Gerberding, G. Heinzel, J. S. Hennig, H. Hogenhuis, C. J. Killow, M. Lieser, S. Lucarelli, S. Nikolov, M. Perreur-Lloyd, J. Pijenburg, D. I. Robertson, A. Sohmer, M. Troebs, H. Ward, and D. Weise, Optical Bench Interferometer - From LISA Pathfinder to NGO/eLISA, in *9th LISA Symposium*, volume 467 of *Astronomical Society of the Pacific Conference Series*, pages 311–315, 2013, Paris, France, May, 2012.

- [43] Christian J. Killow, Ewan D. Fitzsimons, Michael Perreur-Lloyd, David I. Robertson, Henry Ward, and Johanna Bogenstahl, *Optical fiber couplers for precision spaceborne metrology*, Applied optics **55**, 2724 (2016).
- [44] Michael Perreur-Lloyd, Karsten Danzmann, Ewan D. Fitzsimons, Gerhard Heinzel, Jan-Simon Hennig, Christian J. Killow, Maike Lieser, David I. Robertson, Sönke Schuster, Alasdair Taylor, Michael Tröbs, Harry Ward, and Dennis Weise, *Sub-system mechanical design for an eLISA optical bench*, Journal of Physics: Conference Series **610**, 012032 (2015).
- [45] Maike Lieser, Sönke Schuster, and Michael Tröbs, LOB-AEI-TN-16 – Testing Interferometric Imaging for eLISA - Test Report and Final Report, Technical report, AEI Hannover, 2016.
- [46] Frederic Tausch, Experimentelle Bestimmung der Genauigkeit und des Messbereiches einer Quadrantenphotodiode, Facharbeit, 2014.
- [47] Max Zwetz, Non-Gaussian laser beams for the test of the LISA optical bench, Master’s thesis, Leibniz Universität Hannover, 2016.
- [48] Brigitte Kaune, Kontrolle und Charakterisierung von piezobetriebenen Kipp- und Linearaktuatoren für die optische Bank von LISA, Bachelor’s thesis, Leibniz Universität Hannover, Hannover, 2011.
- [49] Anna-Maria A. van Veggel and Christian J. Killow, *Hydroxide catalysis bonding for astronomical instruments*, Adv. Opt. Techn. **3** (2014).
- [50] D.H. Gwo, *Ultra precision and reliable bonding method*, (2001), US Patent 6,284,085.
- [51] D. I. Robertson, E. D. Fitzsimons, C. J. Killow, M. Perreur-Lloyd, H. Ward, J. Bryant, A. M. Cruise, G. Dixon, D. Hoyland, D. Smith, and J. Bogenstahl, *Construction and testing of the optical bench for LISA Pathfinder*, Classical and Quantum Gravity **30** (2013).
- [52] Christian J Killow, Ewan D Fitzsimons, James Hough, Michael Perreur-Lloyd, David I Robertson, Sheila Rowan, and Henry Ward, *Construction of rugged, ultrastable optical assemblies with optical component alignment at the few microradian level*, Applied optics **52**, 177 (2013).
- [53] Marina Dehne, *Construction and noise behaviour for ultra-stable optical systems for space interferometers*, PhD thesis, Leibniz Universität Hannover, Hannover, 2012.
- [54] K Dahl, G Heinzel, B Willke, K A Strain, S Goßler, and K Danzmann, *Suspension platform interferometer for the AEI 10 m prototype: concept*,

- design and optical layout*, Classical and Quantum Gravity **29**, 095024 (2012).
- [55] Ewan D. Fitzsimons, Johanna Bogenstahl, James Hough, Christian J. Killow, Michael Perreur-Lloyd, David I. Robertson, and Henry Ward, *Precision absolute positional measurement of laser beams*, Applied Optics **52**, 2527 (2013).
- [56] Daniel Schuetze, Vitali Mueller, and Gerhard Heinzel, *Precision absolute measurement and alignment of laser beam direction and position*, Applied optics **53**, 6503 (2014).
- [57] M Chwalla, K Danzmann, G Fernández Barranco, E Fitzsimons, O Gerberding, G Heinzel, C J Killow, M Lieser, M Perreur-Lloyd, D I Robertson, S Schuster, T S Schwarze, M Tröbs, H Ward, and M Zwetz, *Design and construction of an optical test bed for LISA imaging systems and tilt-to-length coupling*, Classical and Quantum Gravity **33**, 245015 (2016).
- [58] D Robertson, LOB-UGL-TN-010.1 'Final Alignment Measurements', Technical report, 2015.
- [59] V Wand, J Bogenstahl, C Braxmaier, K Danzmann, A Garcia, F Guzmán, G Heinzel, J Hough, O Jennrich, C Killow, D Robertson, Z Sodnik, F Steier, and H Ward, *Noise sources in the LTP heterodyne interferometer*, Classical and Quantum Gravity **23**, S159 (2006).
- [60] Max Zwetz, Setup and characterization of a measurement system for the LISA OB, Bachelor's Thesis, 2014.
- [61] Maike Lieser, Sönke Schuster, and Michael Tröbs, LOB-AEI-TN-15 – Test of interferometry concept, Technical report, AEI Hannover, 2015.
- [62] First Sensor AG, <http://www.first-sensor.com>.
- [63] M Tröbs, J Bogenstahl, M Dehne, C Diekmann, E Granova, A Shoda, G Wanner, and G Heinzel, LOB-AEI-TN-005.1-13 - Test of interferometry concept, Technical report, AEI Hannover, 2011.
- [64] Sönke Schuster, *TBD*, PhD thesis, Leibniz Universität Hannover, 2016.
- [65] Igor Libmann, Design and characterisation of a thermal shield for LISA optical bench testing, Bachelor's thesis, 2011.
- [66] Josep Sanjuán Muñoz, *Development and validation of the thermal diagnostics instrumentation in LISA Pathfinder*, PhD thesis, Universitat Politècnica de Catalunya, 2009.

- [67] A. Lobo, M. Nofrarias, J. Ramos-Castro, and J. Sanjuan, *On-ground tests of the LISA PathFinder thermal diagnostics system*, *Classical and Quantum Gravity* **23**, 5177 (2006).
- [68] Miquel Nofrarias, *Thermal Diagnostics in the LISA Technology Package Experiment*, PhD thesis, Universitat de Barcelona, 2007.
- [69] Coherent, Inc., *Prometheus - Ultra-Narrow Linewidth CW DPSS Green Laser*, 2013, [www.coherent.com](http://www.coherent.com).
- [70] Volker Leonhardt and Jordan B. Camp, *Space interferometry application of laser frequency stabilization with molecular iodine*, *Applied optics* **45**, 4142 (2006).
- [71] Thilo Schuldt, *Frequenzstabilisierter Nd:YAG-Laser für Weltraumanwendungen*, Diplomarbeit, 2003, Universität Hamburg.
- [72] M. Tröbs, L. d’Arcio, S. Barke, J. Bogenstahl, I. Bykov, M. Dehne, C. Diekmann, E. D. Fitzsimons, R. Fleddermann, O. Gerberding, J.-S. Hennig, F. G. Hey, H. Hogenhuis, C. J. Killow, E. Kochkina, J. Kullmann, M. Lieser, S. Lucarelli, M. Perreur-Lloyd, J. Pijnenburg, D. I. Robertson, A. Shoda, A. Sohmer, A. Taylor, G. Wanner, H. Ward, D. Weise, G. Heinzl, and K. Danzmann, *Testing the LISA optical bench*, in *Proc. of the International Conference on Space Optics*, 2012.
- [73] B. E. A. Saleh and M. C. Teich, *Fundamentals of Photonics*, John Wiley & Sons, Inc., second edition edition, 2007.
- [74] *Fiber Collimators 60FC-... for a range of laser beam diameters using a variety of attached or integrated optics capabilities*, [www.sukhamburg.com](http://www.sukhamburg.com).





# Acknowledgments

First of all I would like to thank Professor Karsten Danzmann for giving me the opportunity to work at the AEI. This is a very special institute with a very nice work environment and great people. I am very grateful that I was given the opportunity to work on such an interesting and exciting project!

I would like to thank Gerhard Heinzl for being my supervisor, sharing his extensive knowledge and giving me the opportunity to work in his group.

I would like to thank Michael Tröbs for being my day-to-day supervisor as the PostDoc in the group and his advise and support.

A very big Thank you is going to the LISA optical bench team! To my group in Hannover, Michael Tröbs, Sönke Schuster und Max Zwetz for great team work and many fruitful discussions, I enjoyed working with you! To the group in Glasgow, Christian Killow, Mike Perreur-Lloyd, Dave Robertson and Harry Ward for building the optical bench and other hardware, and for sharing their knowledge and bonding experience with me! To the team from Airbus, especially Ewan Fitzsimons for his knowledge, support and design work. I also want to thank the people who worked on the project before me (with some overlap), Christian Diekmann, Johanna Bogenstahl, Dennis Weise and all the other people from AEI, Glasgow, Airbus and TNO. Thank you all for giving me the opportunity to work in such a great team!

I want to acknowledge ESA for funding the LISA optical bench project and the DLR for funding various activities.

I am also grateful for the support from all the other people in the Space Interferometry group. Especially Oliver Gerberding, Thomas Schwarze, Germán Fernandez Barranco and Vitali Müller for providing hardware and knowledge to the project and Gunnar Stede for his help in the clean room. But also all the rest of the group for advise, discussions, Mensa company, fun coffee breaks and great conference trips!

I also would like to thank my great office mates, Simon Barke and Henry Wegener.

I am very grateful to the staff of the AEI for all their support and help. This work would not have been possible without the mechanical workshop, the electronic workshop, the IT, the maintenance staff and the secretaries.

I would like to thank all the people from the institute to have made it such a fun time at the AEI!

For their precious time to proof-read this thesis I want to thank Michael Tröbs, Gerhard Heinzl and Conor Mow-Lowry. All remaining mistakes are of course my responsibility!

Last but not least, I want to thank my family for always supporting me and my fiancé Conor, for his support during this stressful time and all other times, and for always believing in me.

# Publications

M Chwalla, K Danzmann, G Fernández Barranco, E Fitzsimons, O Gerberding, G Heinzl, C J Killow, M Lieser, M Perreur-Lloyd, D I Robertson, S Schuster, T S Schwarze, M Tröbs, H Ward, and M Zwestz, *Design and construction of an optical test bed for LISA imaging systems and tilt-to-length coupling*, Classical and Quantum Gravity 33, 245015 (2016).

Maike Lieser, E Fitzsimons, K-S Isleif, C Killow, M Perreur-Lloyd, D Robertson, S Schuster, M Tröbs, S Veith, H Ward, G Heinzl, and K Danzmann, *Construction of an optical test-bed for eLISA*, Journal of Physics: Conference Series 716, 012029 (2016).

Michael Perreur-Lloyd, Karsten Danzmann, Ewan D. Fitzsimons, Gerhard Heinzl, Jan-Simon Hennig, Christian J. Killow, Maike Lieser, David I. Robertson, Sönke Schuster, Alasdair Taylor, Michael Tröbs, Harry Ward, and Dennis Weise, *Sub-system mechanical design for an eLISA optical bench*, 10th LISA Symposium, Journal of Physics: Conference Series 610, 012032 (2015).

K Danzmann et al., The Gravitational Universe, 2014.

M. Hendry, C. Bradaschia, H. Audley, S. Barke, D. G. Blair, N. Christensen, K. Danzmann, A. Freise, O. Gerberding, B. Knispel, M. Lieser, I. Mandel, T. Moore, A. Stuver, B. Whitting *Education and public outreach on gravitational-wave astronomy*, General Relativity and Gravitation, 46 (8), 1764 (2014)

M. Lieser, L. d’Arcio, S. Barke, J. Bogenstahl, C. Diekmann, I. Diepholz, E. D. Fitzsimons, O. Gerberding, J.-S. Hennig, M. Hewitson, F. G. Hey, H. Hogenhuis, C. J. Killow, S. Lucarelli, S. Nikolov, M. Perreur-Lloyd, J. Pijenburg, D. I. Robertson, A. Sohmer, A. Taylor, M. Tröbs, H. Ward, D. Weise, G. Heinzl and K. Danzmann *LISA Optical Bench Testbed*, 9th LISA Symposium, Astronomical Society of the Pacific Conference Series, 467, 301-302 (2013)

M. Tröbs, L. d’Arcio, S. Barke, J. Bogenstahl, C. Diekmann,, E. D. Fitzsimons, O. Gerberding, J.-S. Hennig, F. G. Hey, H. Hogenhuis, C. J. Killow, M. Lieser, S. Lucarelli, S. Nikolov, M. Perreur-Lloyd, J. Pijenburg, D. I. Robert-

son, A. Sohmer, A. Taylor, H. Ward, D. Weise, G. Heinzel and K. Danzmann *LISA Optical Bench Testing*, 9th LISA Symposium, Astronomical Society of the Pacific Conference Series, 467, 233-234 (2013)

L. d’Arcio, J. Bogenstahl, C. Diekmann, E. D. Fitzsimons, G. Heinzel, H. Hogenhuis, C. J. Killow, M. Lieser, S. Nikolov, M. Perreur-Lloyd, J. Pijenburg, D. Robertson, A. Taylor, M. Tröbs, H. Ward, and D. Weise, *An Elegant Breadboard of the Optical Bench for eLISA/NGO*, in Proceedings of the 9th International Conference on Space Optics, 2012.

A. Taylor, L. d’Arcio, J. Bogenstahl, K. Danzmann, C. Diekmann, E. D. Fitzsimons, O. Gerberding, G. Heinzel, J. S. Hennig, H. Hogenhuis, C. J. Killow, M. Lieser, S. Lucarelli, S. Nikolov, M. Perreur-Lloyd, J. Pijenburg, D. I. Robertson, A. Sohmer, M. Tröbs, H. Ward, and D. Weise, *Optical Bench Interferometer - From LISA Pathfinder to NGO/eLISA*, in 9th LISA Symposium, volume 467 of Astronomical Society of the Pacific Conference Series, pages 311–315, 2013, Paris, France, May, 2012.

M. Tröbs, L. d’Arcio, S. Barke, J. Bogenstahl, I. Bykov, M. Dehne, C. Diekmann, E. D. Fitzsimons, R. Fleddermann, O. Gerberding, J.-S. Hennig, F. G. Hey, H. Hogenhuis, C. J. Killow, E. Kochkina, J. Kullmann, M. Lieser, S. Lucarelli, M. Perreur-Lloyd, J. Pijenburg, D. I. Robertson, A. Shoda, A. Sohmer, A. Taylor, G. Wanner, H. Ward, D. Weise, G. Heinzel, and K. Danzmann, *Testing the LISA optical bench*, in Proc. of the International Conference on Space Optics, 2012.

# Curriculum vitae

---

Maike Danielle Lieser

An der Strangriede 2  
30167 Hannover  
email: maike.lieser@gmx.de

born 28th of August 1985 in Seeheim-Jugenheim, Germany

---

- |            |  |
|------------|--|
| 1992-1998  | Primary schools (Grundschule und Orientierungsstufe)   |
| 1998-2005  | Secondary School, Humboldt Gymnasium Eichwalde, Graduation with Abitur   |
| 2005-2011  | Studies of Technical Physics at the Leibniz Universität Hannover   |
| 2011       | Diploma in Physics, Leibniz Universität Hannover<br>Title of the diploma thesis: Kohärente Anti-Stokes Raman-Streuung mit Pulsführung in Wellenleiterstrukturen  |
| since 2011 | PhD student and research associate at the Max Planck Institute for Gravitational Physics (Albert Einstein Institute) in Hannover, stipend holder of the International Max Planck Research School on Gravitational Wave Astronomy for two years |